Abbe School of Photonics | JENA
Friedrich-Schiller-Universität

Deutsches Zentrum
für Luft- und Raumfahrt
German Aerospace Center

Integrated Optical Filter Design in InP for Coherent Optical Communications in Space

Master's Thesis

Muhammed Fatih Akal

February 24, 2023

Academic Supervisors: Prof. Dr. Thomas Pertsch, Dr. Marcin Wojciech Ziarko

Declaration of Independence

I, Muhammed Fatih AKAL, declare that this thesis and the work presented in it are my own. I certify that:

- This work was done wholly or mainly while in candidature for a research degree at this University;
- None of this work has been published before submission;
- I have acknowledged all main sources of help;
- Where I have consulted the published work of others, this is always clearly attributed;
- Where the thesis is based on work done by myself jointly with others, I have made clear exactly what was done by others and what I have contributed myself;
- Where I have quoted from the work of others, the source is always given. With the exception of such quotations, this thesis is entirely my own work;

Date: _____

Signature: _____

Abstract

Extraterrestrial photonic integrated circuits (EPIC) offer potential solutions to relieve the global communication bottleneck in the near future. This study focuses on the design of an important component for an EPIC project at German Aerospace Center (DLR), namely integrated optical filter design. The motivation behind this work is the promise of photonic integration that low loss, lightweight and flexibly tunable filters can be realized for extraterrestrial communication. Furthermore, integrated optical filters can significantly enhance the signal-to-noise ratio (SNR) of communication systems without the need for electro-optical conversions.

Among different material platform options, the focus is mainly directed towards Indium Phosphide (InP). Regarding the investigated optical filter types, mainly ring resonator and Mach-Zehnder Interferometer (MZI) geometries are studied in this thesis. After a detailed examination, the design is finalized using a 2^{nd} order MZI filter with 1.76 mm^2 footprint and 31.25 GHz (0.25 nm) full-width at half-maximum (FWHM). Moreover, 137.5 GHz (1.10 nm) free spectral range (FSR), 25 dB on-off extinction ratio (ER), <1 dB insertion loss (IL) and 18-25 dB power suppression at the centers of the side channels are calculated with Beam Propagation Method (BPM) simulations, which are predicted with the preliminary scattering matrix (S-matrix) analyses. This thesis elaborates on the theoretical fundamentals of ring resonator and MZI filters, followed by the adopted methodology during the entire filter design process. In this regard, it provides a comparative investigation between the two filter types in the context of InP material platform. The performance of the finalized design with MZI is also discussed at the end, including the tuning considerations of the filter.

Acknowledgements

I would like to express my sincere gratitude to Prof. Dr. Thomas Pertsch and Dr. Marcin Wojciech Ziarko for their guidance throughout the entire journey of realizing this thesis. I am also deeply grateful to Giulio Terrasanta and Dr. Nicola Bergamasco for their incredible assistance during the course of the last 6 months. The generous feedbacks I received from them have been quite an important chance for me to learn from my mistakes and refine this work. For the same reason, I also need to definitely include Dr. Ziarko's name here again. In addition, I want to thank him once more for giving me this opportunity to work on this very interesting project at German Aerospace Center (DLR).

I am greatly indebted to Abbe School of Photonics (ASP), Friedrich-Schiller University of Jena (FSU Jena) and German Aerospace Center (DLR) for their financial support with scholarship and salaries, which I appreciate tremendously. And of course, I'd like to acknowledge the scientific and academic knowledge I received from Dr. Sina Saravi during my previous projects at ASP, whose supervision has built the foundations of this thesis.

Finally, the most special thanks from me goes to my mother, brother and sisters, who have always been there for me during the turbulent times I endured in the last few years. I have been, am and will always be grateful for their support.

Table of Contents

List of Figures

List of Tables

List of Abbreviations

IC	Integrated Circuit
PIC	Photonic Integrated Circuit
SNR	Signal-to-Noise Ratio
SDM	Space Division Multiplexing
TDM	Time Division Multiplexing
WDM	Wavelength Division Multiplexing
DWDM	Dense Wavelength Division Multiplexing
KPI	Key Performance Indicator
FSR	Free Spectral Range
FWHM	Full-Width at Half-Maximum
ER	Extinction Ratio
IL	Insertion Loss
TPA	Two-Photon-Absorption
ITU	International Telecommunication Union
SoI	Silicon on Insulator
SiN	Silicon Nitride
InP	Indium Phosphide
InGaAsP	Indium Gallium Arsenide Phosphide
MZI	Mach Zehnder Interferometer
MMI	Multimode Interferometer
S-matrix	Scattering matrix
FDTD	Finite-Difference Time-Domain
BPM	Beam Propagation Method
EME	Eigen-Mode Expansion
ppw	points per wavelength

List of Symbols

α_s	Single-pass-transmission (loss) coefficient
α	Power attenuation coefficient [1/cm]
α_{dB}	Logarithmic power attenuation coefficient [dB/cm]
a, b	Port field amplitudes
κ	Coupling coefficient
t	Transmission coefficient
n_{eff}	Effective index
n_g	Group index
R	Ring (bending) radius
L	Propagation length (ring circumference/MZI arm length)
ΔL	MZI arm length difference
Θ	Phase accumulation
$\Delta\Theta$	Phase accumulation difference
φ	Phase of the complex transmission coefficient multiplication
$d_{coupling}$	Coupling gap width
λ	Wavelength
ν	Frequency
c_0	Speed of light in vacuum
Λ_B	Bragg grating period
m	Mode/solution number
T	Transfer function
P	Port power
FSR	Free spectral range
FWHM	Full-width at half-maximum
IL	Insertion loss
ER	Extinction ratio

To my mother…

Chapter 1

Photonic Integration and Optical Communications

1.1 Introduction to Photonic Integrated Circuits

Photonic integrated circuits (PIC) are the optical counterparts of the electronic integrated circuits (IC), both of which operate to carry out certain logical operations through generation, manipulation and detection of electromagnetic fields. In the case of electronic ICs, the main mean of signal transport is the free electrons inside the metallic wires, whereas the light particles, so-called photons are employed for the same purpose in the dielectric waveguides of PICs. The electronic IC's are much more prevalent due to their smaller sizes, lower costs and broader commercial availabilities. On the other hand, the photonic integration offers the possibility to achieve larger bandwidths, reduced losses and energy consumption and lower latency among its other advantages [2], [3]. Furthermore, when compared to bulk optics, integrated photonics allows to remove the complexity of the optical setups and the related stability problems [4]. This is also supported by the immense reduction of component and circuit sizes, as well as weight and power consumptions [5], [6].

The current state of the photonic integration makes it possible to place thousands of optical components on a single chip [5]. With the similarities to the development of electronic IC's, it is estimated that the exponential growth in the photonic integration would be continued in the coming several decades [5]. Together with the aforementioned benefits, this promise plays as an important drive behind the ongoing research in the field of PIC's and the commercial applications in the fields of optical sensing, telecommunications, metrology and microwave photonics [5], [7]. Since the main design objective of this thesis is centered around the area of optical communications, the discussion will be concentrated on the optical communication systems with their focus on PICs.

1.2 Optical Communications and PICs

The transmission capacity of optical communication systems saw a significant enhancement over the last 30 years [8]. Nevertheless, the upper limit for this capacity might be reached within the next decade, which requires new solutions to be developed [8]. To this end, extraterrestrial optical systems are being considered to improve the global connectivity, where optical fiber communications are restricted in terms of infrastructure [9]. Toward this goal, various aspects of high throughput satellite communication system development at the Institute of Communications and Navigation at German Aerospace Center (DLR) is discussed in the conference paper by Calvo et. al. [9]. In the context of extraterrestrial communications, photonic integration is a promising step to relieve the bottleneck of data transfer with the increased bandwidth promise, compared to the currently utilized radio-frequency (RF) systems [6]. In addition, with the reduced cost, size, weight and power (C-SWaP) consumption, PIC's are superior to the bulk optical setups for their use in satellite systems [6].

There are various methods that have been put forward to enhance the performance of the optical communication systems. Some of these include the Space Division Multiplexing (SDM) and the Time Division Multiplexing (TDM), where the goal is to increase the spatial or temporal effectiveness of the available channels. Another such attempt is to increase the spectral efficiency of the communication channels through the Wavelength Division Multiplexing (WDM) method and/or coherent optical communications. Being relatively more cost- and energy- efficient methods [10], they are used in the system that will be mentioned shortly in this work. An interesting study published by Jørgensen et. al. demonstrates the combination of WDM and SDM in order to achieve quite remarkable transmission rates by using photonic integration [11], which is a promising attempt in combining different signal multiplexing methods with PIC's.

In this study, the transceiver system under focus utilizes coherent communications, in which information can be extracted from both the amplitude and the phase of the modulated signal. This adds a certain hardware complexity to the system, which is another motivation behind the research in PIC's for this purpose [10]. Alongside their main advantages mentioned before, such as reduced power consumption and footprint, PIC's also make it possible to perform many signal processing operations in the optical domain without the need for optical-electronic conversions to implement such coherent optical systems [10]. One example application of such an optical processing is frequency/wavelength filtering, which is useful in increasing the signal-to-noise ratio (SNR) of a communication system by suppressing the additional noise mixed into the original signal during its transfer. To this end, integrated photonics enables the fabrication of filters that have low losses, are light weight and flexibly tunable, which is not straightforward to realize with an electronic microwave filter [12]. This brings

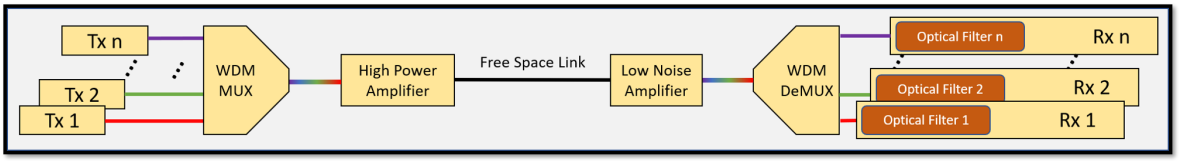

Figure 1.1: General model of the optical transceiver design for which filtering would be implemented

up the topic of the thesis, namely the integrated optical filter design, which is aimed for in order to carry out wavelength filtering in a purely optical domain in real-time.

The procedure of the design will be investigated in the context of an optical transceiver system, the model of which can be seen in Figure 1.1. Using a WDM scheme with multiple separated wavelength channels, the signals generated in the transmitter circuit are sent through the free space optical link and collected at the receiver end after the demultiplexing into the individual channels. Mainly due to the amplifiers in the system, which introduces additional noise to the optical signals, the received signal quality could be lower than the requirements of the general transceiver system. To prevent or diminish such unwanted additions to the signals in the WDM channels, an integrated optical filter is intended to be designed for the receiver circuit. Moreover, it is desired that the designed filter can be tunable and the central wavelength of it can be adjusted for the different channels.

Therefore, the main objective of this thesis is to study the possibilities for an integrated optical filter design in terms of the choice of material platform and available filter types (Chapter 2), which is followed by laying out the theoretical basis of the most promising filtering options (Chapter 3) and the respective simulation methodologies that are utilized along the process (Chapter 4). The results of the design procedure and the detailed analysis of the final design are then discussed (Chapter 5), together with further recommendations and conclusions that would be helpful in similar research projects and/or theses (Chapter 6).

Chapter 2

Initial Design Considerations

2.1 Key Performance Indicators of the Filter Design

The band-pass filter designed in this work needs to be compliant with certain criteria that are determined in advance, such that the choices during the design process can be made according to fixed guidelines. To this end, several key performance indicators (KPI) are determined to be met at the end of the project, which concerns the free spectral range (FSR), full-width at half maximum (FWHM) bandwidth, insertion loss (IL) and extinction ratio (ER) of the band-pass filter (see Figure 2.1). Regarding the FSR, it would be preferable to have as large value as possible, such that the consecutive resonances of the filter would be separated by a spectral range greater than the span between the first and the last communication channel frequencies. In case this is not possible and FSR cannot be made arbitrarily large, it is at least desired that the neighboring channels are aligned with an off-resonance of the filter by setting an appropriate FSR value. As a result, the remaining noise from the adjacent channels would also be suppressed, which would improve the performance of the filter.

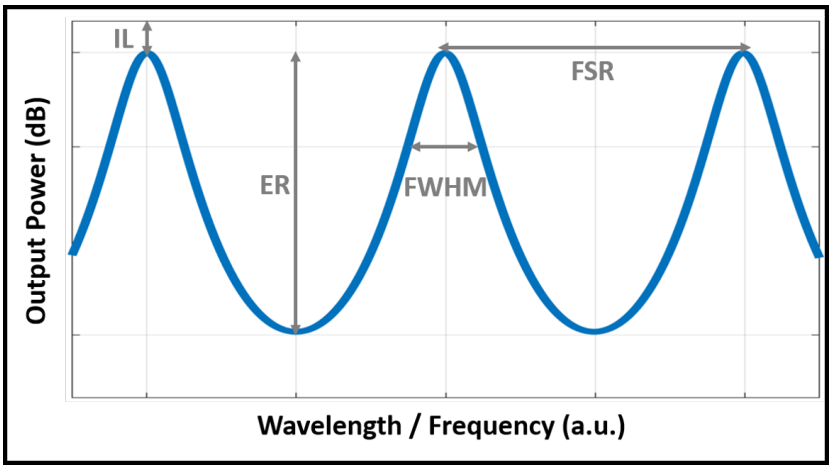

Figure 2.1: Example filter spectrum with determined KPIs of this work

Table 2.1: Key Performance Indicators of the band-pass filter design

	FWHM Bandwidth (GHz)	**Insertion Loss (dB)**	**Extinction Ratio (dB)**
Ideal	37.5	<1	>20
Good	30<FWHM<50	<3	>15
Acceptable	25<FWHM<100	<5	>10

Although at this point, the FSR criterion is left more of a qualitative indicator rather than being defined quantitatively, a numerical example can be given to make it clearer. According to one of the standard WDM channel frequency definitions of the International Telecommunication Union (ITU), 100 GHz separation (0.80 nm at λ=1550 nm) between consecutive channels is considered [1]. If, due to the limitations by the filter type or material choice, it would not be possible to reach an FSR value that is higher than 100 GHz, then one of the feasible approaches would be to set the FSR of the filter to 75 GHz in order to minimize the signal value at the neighboring channels. In this way, the amplitude maxima of the filter would be aligned to the frequencies, whose separation from the design frequency becomes 0, 75, 150, 225,... GHz. This would ensure that at least 6 adjacent higher and lower frequency channels do not align with the resonances of the filter and the noise contributions from those channels can be suppressed to an extent. Another way of circumventing the limited FSR values could be to utilize the so-called Vernier Effect by going to higher-order filtering, which is a nice solution that will be discussed later.

For the other three indicators, namely FWHM, IL and ER, quantitative limits can be determined. In this sense, the range of values that are acceptable, good or ideal for the project goals are listed in Table 2.1. As will be discussed in the next chapters, meeting each criterion with an ideal scenario might prove difficult and certain trade-offs should be made to reach the best possible design.

2.2 Material Platforms for PICs

For the photonic integration, there are numerous alternative material platforms available, such as Silicon on Insulator (SoI), Silicon Nitride (Si_3N_4 or shortly SiN), Indium Phosphide (InP) and Lithium Niobate ($LiNbO_3$). In this work, the most commonly preferred three among these platforms, namely SoI, SiN and InP will be investigated, regarding their advantages and disadvantages both in general and also in the context of filter design. For the details of the current state of the photonic integration on these platforms, the reader is referred to the publications of Thomson et. al. (SoI) [13], Blumenthal et. al. (SiN) [14] and Smit et. al (InP) [5]. A general comparison of the available platforms is given in Table 2.2. Comparison of the available material platforms, which provides an initial insight on the investigation made in the next subsections.

Table 2.2: Comparison of the available material platforms

	SoI	**SiN**	**InP**
Index Contrast	High	Medium	Low
Device Footprint	Small	Medium	Large
CMOS Compatibility	Yes	Yes	No
Waveguide Loss	Medium	Low	High
Monolithic Photonic Integration	No	No	Yes
Thermo-Optic Coefficient (dn/dT)	$10^{-4}\ K^{-1}$	$10^{-5}\ K^{-1}$	$10^{-4}\ K^{-1}$

2.2.1 Silicon on Insulator

At the design wavelength of 1550 nm, the refractive indices of the Silicon (Si) and Silica (SiO_2) are approximately around 3.47 [15] and 1.44 [16], respectively. This high index contrast between the core and the cladding regions allows the SoI platform to ensure strong mode confinement in the waveguides. Compared to its alternatives, this results in SoI to accommodate the smallest waveguide dimensions, as well as having the smallest bending losses. Due to this feature, the component sizes can be made very small in SoI, meaning small footprint devices and complex chips are best realizable with Silicon [2], [17]. The other significant advantage SoI offers is the availability of CMOS integration process, which is also based on the Silicon platform [18], [19]. Hence, the already available electronic fabrication facilities, the knowhow of which is already maturely developed during the past few decades, can be utilized for fabricating the photonic circuits [2], [17], [18]. Despite these advantages, there are certain drawbacks of choosing SoI as the material platform. The first of these reasons is the sensitivity to fabrication processes with the high-index-contrast nature the platform possesses, which might not tolerate even several nm-sized fabrication errors on the waveguide sidewalls by resulting in an increased loss in the order of 1 dB/cm [17]. More importantly, it is a challenge to realize active devices using Silicon, since it has an indirect bandgap with the transition energy of 1.12 eV and has negligible second order nonlinearity [17], [18]. Especially at the telecom wavelengths, this renders the on-chip fabrication of lasers, amplifiers, modulators and detectors, although not impossible, difficult to realize on this platform, [20], [21].

2.2.2 Silicon Nitride

Certain similar characteristics to SoI can be observed with SiN, which is also a CMOS-compatible platform, though it has certain advantages, making it worthy of consideration as an alternative to SoI [12]. First and foremost, SiN offers much lower propagation losses, enabling it to be attractive in terms of waveguiding and passive component designs in photonic circuits [17], [19]. This can be partially attributed to the lower index contrast in the order of 0.55 between the core (SiN) and the cladding (SiO_2), where the refractive index of SiN is approximately 2 [16], [19]. Compared to SoI platform,

this offers fabrication tolerance and flexibility to the SiN circuits [19], [22], although the cost in this case comes with increased device dimensions in SiN. Moreover, increased losses are encountered in SoI at high powers due to the presence of the Two-Photon-Absorption (TPA) effect in Silicon [17], [18]. Owing to the large bandgap of SiN, on the other hand, TPA does not pose any issues in SiN across the wavelengths of telecommunication bands, as well as within the visible range [17], [18], [19], [23]. Despite these interesting aspects of SiN, the alternative platforms offer better performance in the case of tunability in optical filtering using the thermo-optic effect. This is mainly because the thermo-optic coefficient of SiN ($\frac{dn}{dT} \sim 10^{-5}\ K^{-1}$) is ten times lower than Silicon ($\frac{dn}{dT} \sim 10^{-4}\ K^{-1}$) and Indium Phosphide ($\frac{dn}{dT} \sim 10^{-4}\ K^{-1}$), which requires longer or larger devices to achieve the same level of tunability [24], [25], [26], [27].

2.2.3 Indium Phosphide

The third material platform that will be discussed, namely InP, is another important alternative to previously mentioned Si-based platforms and is chosen for the filter design that will be investigated in this thesis. InP is a popular commercial PIC platform that offers pure monolithic integration of all optoelectronic circuit functionalities, where passive and active devices can be combined on a single chip [6], [28]. Being a III-V semiconductor with direct bandgap and lack of inversion symmetry, InP allows achieving optical gain and electro-optic modulation and thus inherent and simultaneous realization of lasers, amplifiers and modulators, together with photodetectors and passive devices as opposed to SoI and SiN [7], [18], [28].

The refractive index of InP cladding at 1550 nm is 3.16, whereas the InGaAsP core index depends on the Arsenic ratio in the material that results in a relatively large range of values between 3.2 and 3.5 [29], [30]. Nevertheless, the highest Arsenic density yields around 0.3 index difference between the core and the cladding, which is lower than SoI and SiN systems. A direct implication of this is increased device dimensions in InP, proving to be a disadvantage when seeking for a small footprint circuit design. Compared to the previous alternatives, there is also another downside of InP, which is the increased linear losses in waveguides due to its higher absorption [18], [21]. Despite the CMOS incompatibility, larger component sizes and higher losses, InP is a promising platform that is preferred in the optical transceiver system of this study, for which the integrated filter design will be studied.

2.3 Integrated Optical Filter Types

There are several common filter types to choose from when integrated optical filter design is considered. These can be listed as Bragg grating, ring resonator and Mach Zehnder interferometer (MZI) filters. Each has its advantages and disadvantages; hence the determination of the filter type requires a careful analysis of the possible trade-offs of each of them. In this sense, an initial examination and a comparative study of the Bragg grating, ring resonator and MZI filters will be done, after which the available options are narrowed down for more focused investigations.

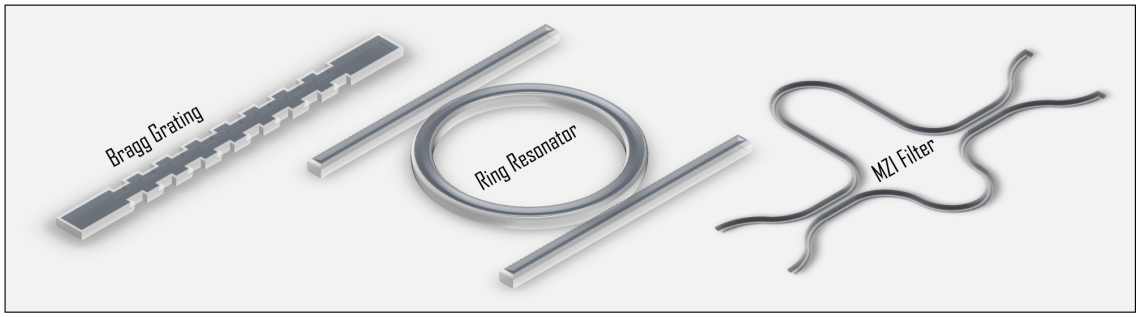

Figure 2.2: Bragg grating, ring resonator and Mach Zehnder interferometer filter structures

2.3.1 Bragg Grating Filter

The common property of all three filter types is that each work on interference and coupling mechanisms to separate certain wavelengths from others, in order to achieve filtering. Differing from the other two, coupling in Bragg grating filter takes place as contra-directional, rather than co-directional. In this sense, Bragg grating acts as a band-stop filter, where the filtered spectral content is reflected and travels in the opposite direction to the pass-band signal. This brings up the first disadvantage of Bragg grating filters, which is the necessity of having additional optical elements at the input such as a circulator or a multimode interferometer (MMI) coupler for separating the input and the filtered signals [31], [32].

The physical mechanism of the filtering with a Bragg grating can be attributed to the grating condition, which, when satisfied, enables a constructive interference of the reflected light from periodically arranged varying effective index sections [33]. Reflection of light at the boundaries of different effective index regions follow the Fresnel equations. The effective index changes can be realized by actual refractive index variation or also by corrugation of waveguide widths that alters the effective index of the propagating light inside the waveguide [34]. Any wavelength of light experiences a non-zero value of reflection at each interface, however only the wavelengths, Λ_B, satisfying a certain condition can be phase-matched and build up their intensities in the opposite propagation direction. This requirement is imposed by the so-called grating condition:

$$m\lambda_B = 2n_{eff,av} * \Lambda_B \tag{2.1}$$

where the grating period is denoted by Λ_B, the average effective index by $n_{eff,av}$ and the diffraction order by an integer m. Here, the value of the average effective index is between the effective indices of the different sections and depends on the ratio of the respective section lengths.

While designing a Bragg grating filter, it is possible to modify the reflectivity spectrum and the corresponding bandwidth of the filtered signal by changing the coupling coefficient. For example, by decreasing the corrugation width or index difference, narrower bandwidths can be achieved with the cost of lower maximum reflectivity value [33], [35]. As a counter measure to this, the usage of longer gratings could be a solution, which indicates an increase in the device dimensions and might not be always preferable depending on the design considerations [31], [33], [35].

The main advantage of using a Bragg grating for filtering purposes, on the other hand, is the quasi FSR-free operation it offers in a broad wavelength range [31]. This can be understood by inspecting Eq. 2.1, the right-hand side of which is fixed with the physical parameters, effective index and grating period. As an example, assuming a wavelength for the first order solution to the Eq. 2.1, (e.g. m=1, $\Lambda_{B,1}$=1550 nm), the second diffraction order solution (m=2) can be found at the half wavelength ($\Lambda_{B,2}$=775 nm) and the increasing order of solutions divide the fundamental wavelength by the order number. Hence, the nearest wavelength band that is also reflected with the Bragg grating would be separated from the first reflection band by 775 nm in this example. Considering the WDM spectral grid standards of the ITU, in which the channels are defined by sub-nanometer separations, Bragg grating can therefore be considered to offer FSR-free-operation in effect [1]. Despite this very important merit of Bragg grating filters, it is nevertheless very difficult to obtain sub-nanometer FWHM values with this filter geometry, since it would require very small coupling strengths and hence nm-sized physical corrugations, the fabrication of which is not a simple process [31], [36]. An example study on SoI reported 0.80 nm filter bandwidth with a strip waveguide and sidewall corrugation widths of only 10 nm, the reproducibility of which was questioned by the authors themselves [37]. In general, many reported waveguide Bragg gratings are in fact fabricated using electron beam lithography, which is nevertheless not suitable for commercial applications [38]. Mainly due to possible fabrication difficulties which are connected to these reasons, Bragg grating filter is not considered for the design that will be followed in this thesis.

2.3.2 Ring Resonator Filter

Ring resonators are the most commonly used components in bandpass filters due to their compactness, as well as their ease of fabrication [39]. Here as well, it is possible with ring resonator filters to have the flexibility of bandwidth adjustment by changing the coupling strength, as it is the case in Bragg grating filters [40]. The theoretical analysis of the ring resonator geometry will be done in the next chapter. Nevertheless, for an introductory understanding and comparison purposes, the physical filtering operation will be superficially provided at this point.

The structure in focus for this study is a so-called add-drop ring resonator filter, where a ring waveguide is placed between two straight waveguides, which are called the input-pass and add-drop bus waveguides. The input signal couples to the ring waveguide, when the coupling gap distance is sufficiently small, the value of which depends on many factors, such as material properties and waveguide geometries. After completing a half round trip inside the ring, the field couples to the drop (output) port and the remaining field amplitude in the ring completes its full circle. Reaching the input-ring coupling region, the field interferes with a time-shifted version of itself and depending on the wavelength, the magnitude inside the ring can be enhanced or suppressed. After many periodic interference events, the field inside the ring, as well as the output port field reaches a steady state, where the wavelength determines how much power is coupled to the output port. The resonant wavelengths would hence be filtered or separated from the rest of the signal and forwarded to a different waveguide from the input-pass waveguide, in which the unfiltered signal content remains.

Coupling coefficient strength at coupling regions, as well as ring radius, effective index and losses

in the resonator determine the properties of the filter response, which requires a certain design process depending on the desired KPIs of the filter.

2.3.3 Mach Zehnder Interferometer Filter

As the name suggests, the simplest, first-order configuration of the MZI filter is constructed by a Mach Zehnder interferometer which is placed between two coupling sections. The first coupling region is responsible for splitting the input field into the two arms of the Mach Zehnder interferometer. The wavelength and the effective index of the mode in the MZI arms determines the characteristics of the interference event taking place at the second coupling region. Hence, the field gets separated into two channels, where certain wavelengths are forwarded to the first port and the rest to the second port. Thanks to the simple configuration of MZI and coupling sections, which are inherently low-loss devices, it is easily possible to fabricate a low-loss filter with this structure [41]. From the design perspective, it is also straightforward to adjust the FSR with a first-order MZI filter by only varying the arm length differences, yet only with the cost of a non-adjustable FWHM, as mentioned previously.

The main difference of the MZI filter geometry from the ring resonator filter is that the field is fed-forward in the system, as opposed to the feedback loop observed in the latter filter type [42]. This has a direct implication on the pass-band characteristics of the filters, where a Lorentzian shape can be seen in the first-order ring resonator filter spectrum and sinusoidal response is observed in the first-order MZI filter outputs [43]. From the transfer function analysis perspective, this can be explained by the pole creation in a feedback looped coupled system (ring resonator) and zero creation in a cascaded feed-forward geometry (MZI) [42].

Leaving the further theoretical details to the next chapter, it can be shortly summarized that MZI filter has an inverse characteristic spectrum compared to the ring resonator filter, which can be either be preferable or not depending on the design criteria. In this thesis, since a flexibility in finesse of the resonance is sought, ring resonator becomes advantageous in terms of the design goal and it is the first geometry that is chosen to be investigated in the next chapter.

2.4 A General Discussion on the Filter Types in the Context of Indium Phosphide

Having laid the fundamentals of the different options in terms of material platforms and integrated filter types for the design in focus, the scope can be narrowed down and the inapplicable choices can be eliminated. To this end, the decision on the material platform, as also indicated earlier, is made on the InP, since the main priority is determined to be the monolithic integration of the filter with the rest of the existing transceiver circuit design that is realized in InP.

In terms of the filter type, Bragg grating filter was disregarded as not being easily fabricable to achieve the 37.5 GHz (0.30 nm) FWHM goal. Due to the compactness of the geometry and flexible bandwidth/finesse features it offers, an initial consideration is made on the ring resonator filter. However, the relatively low field confinement in InP poses a limitation in the minimum achievable bending radius. Compared to the SoI and SiN, this indicates having larger ring resonators with reduced band-

width and resonance spacings in InP. An example value from a commercial InP foundry, Fraunhofer HHI, shows that bending radius value below 150 μm is not accessible, due to the exponentially increasing bending losses after this limit [44]. At this point, the reader is referred to another study on InP ring resonator filter design, in which a depiction of the relations between the ring radius and FSR/bending losses are given quite intuitively [45]. On the other hand, although being structure-wise not as compact as the ring resonator, MZI filter is also visited as the other promising alternative. In contrast to the ring resonator, where the down-limited ring radius affects the characteristics of the resonances, the main decisive parameter in the MZI filter geometry becomes the interferometer arm length differences, which can be made arbitrarily small or large. Thus, the spectral response of the MZI filter is not strictly restricted by the material platform. With these considerations, the theoretical studies on both ring resonator and MZI filters are made in the beginning of the design process, which can be found in the next chapter.

Chapter 3

Theoretical Backgrounds of Ring Resonator and MZI Filters with S-Matrix Analysis

The scattering matrix (S-matrix) model is a relatively simple but useful mean of representing the steady-state response of resonator geometries [46]. It allows to extract the field relations between the input and the output ports of a system by its internal parameters and it is a simple, yet relatively accurate model in the case of ring resonators, which otherwise would require more sophisticated and computationally heavy methods, such as Finite-Difference Time-Domain (FDTD) method. In this sense, a framework for the ring resonator filter will be developed, which afterwards will be utilized for the MZI filter as well. Furthermore, initial results of the theoretical derivations and the implications of the chosen geometries on the filter design will be investigated by the analyses of the generated MATLAB scripts and plots. This would enable the representation of the relations between the KPI parameters, such as FSR, FWHM, IL and ER, on the internal parameters of the system, namely coupling coefficients (κ), loss coefficients (α), effective index (n_{eff}), ring radius (R) and interferometer arm lengths (L).

3.1 Add-Drop Ring Resonator Filter Theory

In this section, the main focus is on the derivation of the spectral characteristics of a 1st order double-bus add-drop ring resonator filter. For the theoretical derivations on all-pass ring resonators with only one bus waveguide, one can refer to the references [47], [48]. Nevertheless, most of the conceptual derivations made for the add-drop filter are the same as in the all-pass filter, with slight changes considering the device structure. The mathematics of the derivation can even further be adapted for higher order geometries with multiple serially cascaded ring resonators. However, since the main idea of this analysis is to understand the relations between the fundamental parameters of the system and the spectral characteristics, an initial consideration is given to the 1st order geometry that is sufficient for this purpose.

The schematic of the 1st order double-bus add-drop ring resonator filter is given in Figure 3.1a,

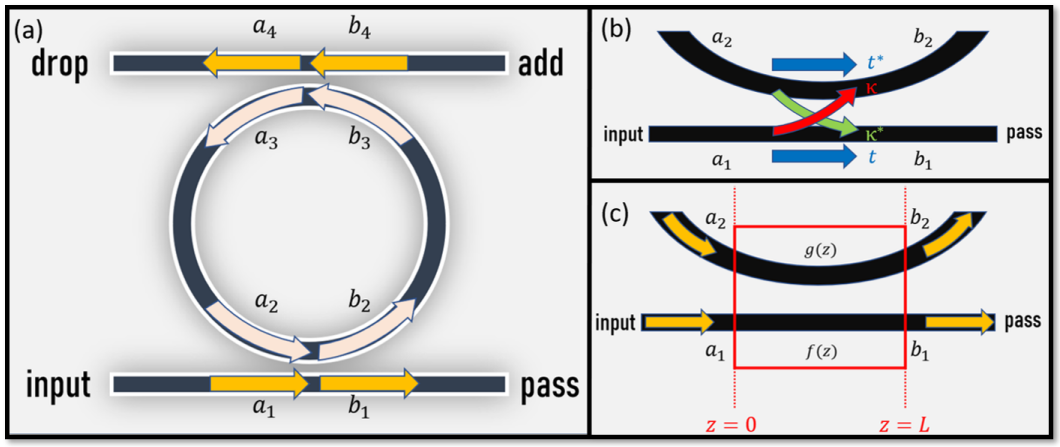

Figure 3.1: (a) 1^{st} order double bus add-drop ring resonator filter model with (b) coupling and transmission coefficient definitions, as well as (c) the related model for coupling mode theory analysis given in Appendix A

including the field amplitude terms at the individual ports of the system. The input, pass, drop (output) and add ports are denoted by a_1, a_2, b_1, b_2, respectively. Starting with the first coupling region, the relation between the outgoing fields (b_1&b_2) and the incoming fields (a_1&a_2) can be written using S-matrix formalism [46]:

$$\begin{pmatrix} b_1 \\ b_2 \end{pmatrix} = \begin{pmatrix} s_{11} & s_{12} \\ s_{21} & s_{22} \end{pmatrix} \begin{pmatrix} a_1 \\ a_2 \end{pmatrix} \tag{3.1}$$

In order to find the relations between the individual matrix elements, certain assumptions need to be made, the first of which is taking the losses during the coupling process to be zero. Also, it is convenient to assume that a single unidirectional mode of the resonator is excited [49] and no reflection takes place in the system. Initially, the relation between the off-diagonal elements of the matrix can be found by referring to the coupled mode theory, which is provided in Appendix A. Using the result obtained there, the complete matrix is then expressed as (see also Figure 3.1b) [49]:

$$S = \begin{pmatrix} t & -\kappa^* \\ \kappa & t^* \end{pmatrix} \tag{3.2}$$

Hence, the relation between the outgoing fields (b_1&b_2) and the incoming fields (a_1&a_2) at the first coupling region can be written using the S-matrix as:

$$\begin{pmatrix} b_1 \\ b_2 \end{pmatrix} = \begin{pmatrix} t_1 & -\kappa_1^* \\ \kappa_1 & t_1^* \end{pmatrix} \begin{pmatrix} a_1 \\ a_2 \end{pmatrix} \tag{3.3}$$

where the subscript 1 is used in the coupling and transmission coefficients, indicating the interactions at the first coupling region. After a half round trip in the resonator, the complex field transforms to:

$$b_3 = \sqrt{\alpha_s e^{i\theta} b_2} \tag{3.4}$$

with α_s being the single-pass amplitude transmission (also referred to as a loss coefficient in this thesis), which scales down the field amplitude as a function of losses during a single round-trip in the resonator and has a real value between 0 and 1. Since the definitions of α_s and θ are made considering the whole round-trip circulation, they taken inside a square root in the case of a half-round trip. Here, α_s is unitless and is related to the power attenuation coefficient, α [1/cm], and the power attenuation coefficient in dB scale, α_{dB} [dB/cm], as [47]:

$$\alpha_s^2 = e^{-\alpha L} = 10^{-\left(\frac{\alpha_{dB} L}{10}\right)} \tag{3.5}$$

In telecommunications, it is a common usage to express the power attenuation in dB scale with regards to the propagation distance, hence the last expression proves to be important. The conversion between the power attenuation coefficient and its dB-scale counterpart can be done with the formula:

$$\alpha_{dB} = \frac{10}{ln(10)}\alpha \tag{3.6}$$

Getting back to the other term in Eq. 3.4; the phase accumulation after a full round trip, θ, is given by the multiplication of the propagation constant, β, and the circumference of the ring, L:

$$\theta = \beta L = \frac{2\pi n_{eff}}{\lambda_0} * 2\pi R_{ring} = \frac{4\pi^2 n_{eff} R_{ring}}{\lambda_0} = \frac{4\pi^2 n_{eff} R_{ring}}{c_0}\nu \tag{3.7}$$

Here, R_{ring} is the ring radius, λ_0 is the wavelength of the field in vacuum and n_{eff} is the effective index of the waveguide. The matrix at the second coupling region on the add-drop waveguide has the same form as the initial one and relates the outputs a_3 and a_4 to the inputs b_3 and b_4:

$$\begin{pmatrix} a_3 \\ a_4 \end{pmatrix} = \begin{pmatrix} t_2 & -\kappa_2^* \\ \kappa_2 & t_2^* \end{pmatrix} \begin{pmatrix} b_3 \\ b_4 \end{pmatrix} \tag{3.8}$$

Again, after another half round trip in the resonator, which is identical to the previous one, the field inside the ring returns to the first coupling region, which allows to write:

$$a_2 = \sqrt{\alpha_s e^{i\theta} a_3} \tag{3.9}$$

When the input at the add port ($b_4 = 0$) is assumed to be zero, the port field amplitudes are found with respect to the input port amplitude, a_1, by solving the system of equations presented above. The corresponding expressions for each port can be found in Appendix B.1. Narrowing the focus to the two interesting ports of the system, namely the pass (b_1) and the drop (a_4) ports, the respective powers can be found by taking the absolute square of the field amplitudes from Appendix B.1:

$$|b_1|^2 = |a_1|^2 \left(\frac{|t_1|^2 + |t_2|^2\alpha_s^2 - 2Re\{t_1 t_2^* \alpha_s e^{-i\theta}\}}{1 + |t_1 t_2|^2\alpha_s^2 - 2Re\{t_1 t_2^* \alpha_s e^{-i\theta}\}} \right) \tag{3.10}$$

$$|a_4|^2 = |a_1|^2 \left(\frac{|\kappa_1 \kappa_2|^2 \alpha_s}{1 + |t_1 t_2|^2\alpha_s^2 - 2Re\{t_1 t_2^* \alpha_s e^{-i\theta}\}} \right) \tag{3.11}$$

with $\theta = \frac{4\pi^2 n_{eff} R_{ring}}{\lambda_0}$ and $|t_i|^2 + |\kappa_i|^2 = 1$, where $i \in \{1, 2\}$.

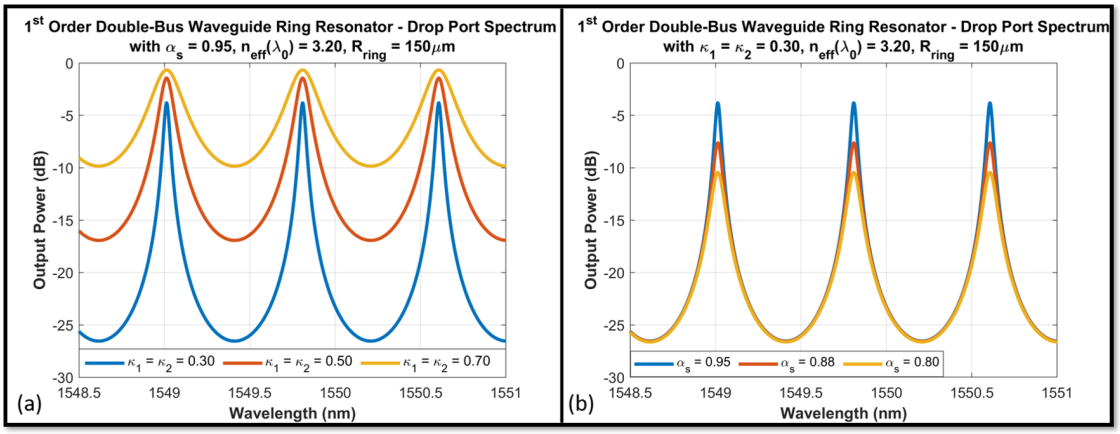

Figure 3.2: Drop power spectra as a function of (a) coupling coefficients and (b) single-pass transmission coefficient

To give an initial insight on the response at the drop port, two example spectra are plotted in Figure 3.2 between 1548.5 nm and 1551 nm with different coupling (κ) and single-pass loss (α_s) coefficients. The waveguide effective index ($n_{eff} = 3.20$) is chosen to be between the refractive indices of the InP cladding [29] and the InGaAsP core [30]. Ring radius is fixed to 150 μm, considering the lower achievable bend limit at our foundry, Fraunhofer HHI [44]. Furthermore, for referencing, the single-pass transmission term value of 0.95 corresponds to 10% power loss in a single round-trip.

Since the characteristics of the transfer function at the drop and pass ports are of particular interest for the filter design, the definitions of the port transfer functions are introduced at this point, which are the ratio of the respective port powers to the input power as functions of wavelength (or frequency):

$$T_d = \frac{|a_4|^2}{|a_1|^2} = \left(\frac{|\kappa_1 \kappa_2|^2 \alpha_s}{1 + |t_1 t_2|^2 \alpha_s^2 - 2|t_1 t_2| \alpha_s \cos(\varphi - \theta)} \right) \tag{3.12}$$

$$T_p = \frac{|b_1|^2}{|a_1|^2} = \left(\frac{|t_1|^2 + |t_2|^2 \alpha_s^2 - 2|t_1 t_2| \alpha_s \cos(\varphi - \theta)}{1 + |t_1 t_2|^2 \alpha_s^2 - 2|t_1 t_2| \alpha_s \cos(\varphi - \theta)} \right) \tag{3.13}$$

where the relation $t_1 t_2^* = |t_1 t_2| e^{i\varphi}$ is defined, with φ denoting the phase of the multiplication of the complex transmission terms. The subscript "p" is used to denote the pass port and "d" represents the drop port. Inspecting the drop port transfer function allows to see the periodic behavior of the spectral response that is observable in Figure 5, where the denominator attains the minimum value at resonances with the cosine term having the value of 1 and the signal power at the drop (output) port is maximized. In this case, the amount of power detected at the pass port is then minimized. Furthermore, the power at the pass port at a resonance can drop to 0, when the so-called "critical coupling condition" is satisfied [46]:

$$|t_1| = |t_2| \alpha_s \qquad (t_2 \; is \; fixed) \tag{3.14}$$

$$|t_2| = |t_1| \alpha_s \qquad (t_1 \; is \; fixed) \tag{3.15}$$

The first condition (Eq. 3.14) is obtained by equating the derivative of Eq. 3.13 with respect to κ_1 or t_1 to zero, whereas the second condition (Eq. 3.15) is found by minimizing the same equation with respect to κ_2 or t_2. Therefore, if one of the transmission coefficients is fixed, setting the value of the other transmission coefficient equal to the fixed one scaled by the single-pass loss coefficient (α_s) would maximize the transferred power to the drop port at resonance.

Because the ring resonator filter is a passive device, the power transmitted to the other ports are always smaller than the input port power. The amount of energy reduction with the introduction of the filter to the system is expressed with the term "Insertion Loss" (IL), which is partially due to scattering, absorption and coupling losses that the optical signal experiences as it passes through the filter. With the filter considered in this study, one can reach the mathematical expression for the IL at the drop port in a logarithmic scale by evaluating the transfer function at a resonance, where the cosine term is equal to 1 and the signal power at the drop (output) port is maximized:

$$IL_d = -10\log_{10}(T_{d,0}) = -10\log_{10}\left(\frac{|\kappa_1\kappa_2|^2\alpha_s}{(1-|t_1t_2|\alpha_s)^2}\right) \tag{3.16}$$

Here, the subscript 0 is used to indicate the transfer function at resonance. Furthermore, the on-off extinction ratio (ER) of the drop port (ER_d), which is the ratio between the maximum power at the respective port to the minimum power, can be written in the dB-scale as:

$$ER_d = 10\log_{10}\left(\frac{\arg\max_{\lambda}(T_d)}{\arg\min_{\lambda}(T_d)}\right) = 10\log_{10}\left(\frac{(1+|t_1t_2|\alpha_s)^2}{(1-|t_1t_2|\alpha_s)^2}\right) \tag{3.17}$$

The effects of changing the coupling and loss coefficients on IL and ER are depicted as an example in Figure 3.3, which are generated as the direct results of Eq. 3.16 and Eq. 3.17. Low coupling strengths increase the value of IL and ER (Figure 3.3b and Figure 3.3d), whereas increasing internal losses enhance the IL but at the same time reduce ER (Figure 3.3a and Figure 3.3c). Moreover, the critical coupling condition can be seen to minimize the IL (Figure 3.3b), the significance of which should be taken into account. Hence, for obtaining a filter with low IL and high ER, finding the right balance regarding the coupling coefficients becomes crucial.

Returning back to the derivations of the other relevant terms of the system, it is previously mentioned that the resonance takes place when the cosine term adopts its maximum value, 1. The physical explanation behind the resonance condition can be done by looking closely to the cosine term. At resonance, the phase accumulation, θ_m, of the m^{th} resonant mode in the ring after a complete round trip satisfies the following equation:

$$(\theta_m - \varphi) = 2\pi m, \qquad m \in \mathbb{N} \tag{3.18}$$

$$\theta_m = \beta_m L = \frac{4\pi^2 n_{eff} R_{ring}}{\lambda_m} = \frac{4\pi^2 n_{eff} R_{ring}}{c_0}\nu_m = (2\pi m + \varphi), \qquad m \in \mathbb{N} \tag{3.19}$$

Meeting the phase matching condition in Eq. 3.19 allows the field inside the ring resonator to constructively interfere with itself at the coupling region after each round-trip. On the contrary, the field is cancelled out if the interference happens destructively, which happens when a π phase shifted

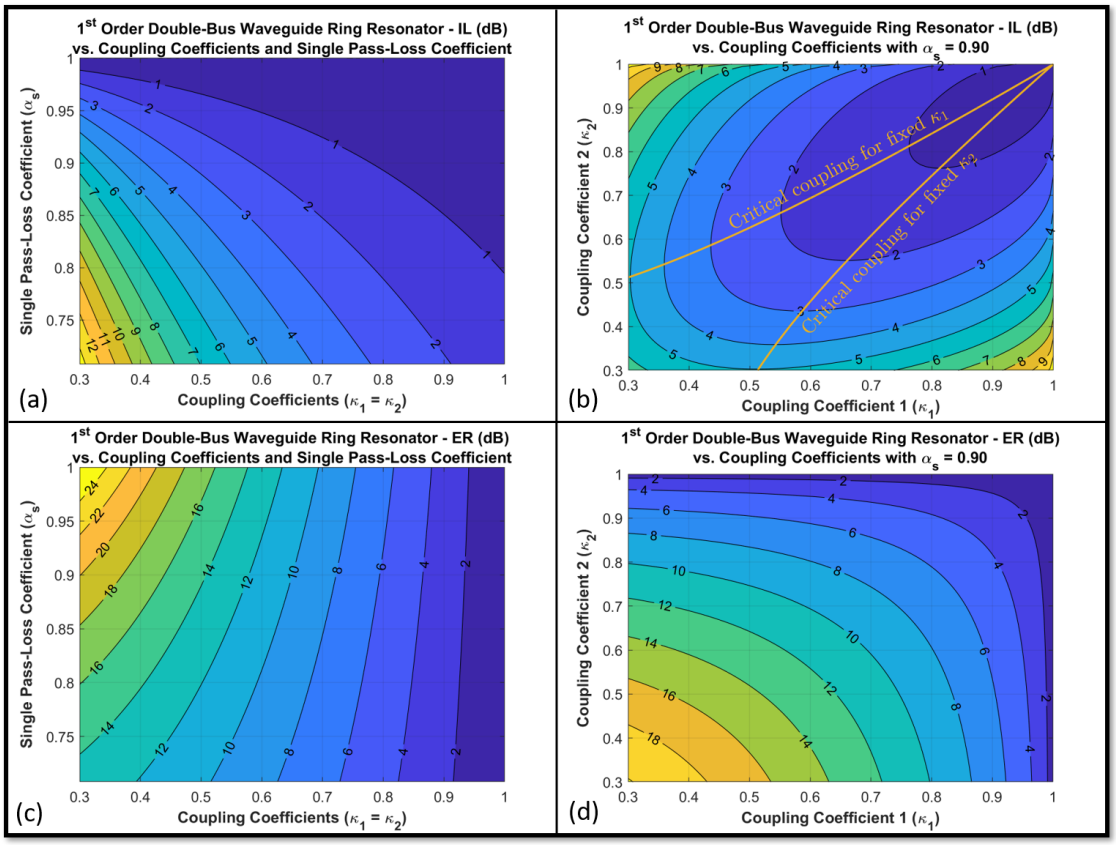

Figure 3.3: Insertion loss (a)-(b) and extinction ratio (c)-(d) of the 1^{st} order ring resonator as a function of coupling coefficients and single pass-loss-coefficient

version of the field coincides with the initial field after travelling around the ring. Since the phase term φ has a constant value between 0 and 2π, it can be negligible if m is not small. In this case, the resonance frequencies and respective wavelengths can be written as:

$$\nu_m = m * \frac{c_0}{2\pi n_{eff} R_{ring}} \tag{3.20}$$

$$m\lambda_m = 2\pi n_{eff} R_{ring} \tag{3.21}$$

An important filter parameter, the so-called free spectral range (FSR) expresses the spectral gap between neighboring resonances, the formula of which in this case can be found by taking the frequency difference between arbitrary consecutive resonances:

$$FSR_\nu = \nu_{m+1} - \nu_m = \frac{c_0}{2\pi n_g R_{ring}} \tag{3.22}$$

$$FSR_\lambda \approx FSR_\nu \frac{\lambda_m^2}{c_0} \approx \frac{\lambda_m^2}{2\pi n_g R_{ring}} \tag{3.23}$$

where n_g is the group index, which takes the dispersion of the waveguide into account with its relation to the effective index, n_{eff}, [47]:

$$n_g = n_{eff} - \lambda_0 \frac{dn_{eff}}{d\lambda} \tag{3.24}$$

The next term that has a major significance in the filter response is the FWHM. It is also known as the 3-dB bandwidth, which expresses the frequency span outside of which the output power reduces by 3 dB, as the name suggests. Requiring several steps of derivation, it expresses the spectrum region where more than half of the resonance output power is present at the output port, which in this case is the drop port. Starting with the transfer function at resonance:

$$T_{d,0} = \left(\frac{|\kappa_1 \kappa_2|^2 \alpha_s}{(1 - |t_1 t_2| \alpha_s)^2} \right) \tag{3.25}$$

This power is halved at the 3-dB bandwidth limits when the value in the denominator is doubled. The phase accumulation term at the lower frequency limit is denoted as θ_l and the higher limit as θ_h. The doubling of the denominator value for these cases can be written as:

$$\frac{1}{2} = \left(\frac{1 + |t_1 t_2|^2 \alpha_s^2 - 2|t_1 t_2| \alpha_s}{1 + |t_1 t_2|^2 \alpha_s^2 - 2|t_1 t_2| \alpha_s \cos(\varphi - \theta_{l,h})} \right) \tag{3.26}$$

$$\cos(\varphi - \theta_{l,h}) = 1 - \frac{(1 - |t_1 t_2| \alpha_s)^2}{2|t_1 t_2| \alpha_s} \tag{3.27}$$

It is important to note that there is no real solution to the equation above with high coupling, small transmission values, where the right-hand side of the equation takes on values outside (-1,1). For very high coupling cases, the 3-dB bandwidth definition cannot be used anymore since the off-resonance signal level increases above 3 dB and the ER decreases below 3 dB. Therefore, care must be taken while continuing with the steps below for deriving the FWHM.

$$\theta_l = \varphi - \arccos \left(1 - \frac{(1 - |t_1 t_2| \alpha_s)^2}{2|t_1 t_2| \alpha_s} \right) \tag{3.28}$$

$$\theta_h = \varphi + \arccos \left(1 - \frac{(1 - |t_1 t_2| \alpha_s)^2}{2|t_1 t_2| \alpha_s} \right) \tag{3.29}$$

$$\Delta\Theta_{hl} = \theta_h - \theta_l = 2 \arccos \left(1 - \frac{(1 - |t_1 t_2| \alpha_s)^2}{2|t_1 t_2| \alpha_s} \right) \tag{3.30}$$

Moreover, writing the initial formula for the phase accumulation terms containing the frequency dependency and taking the difference allows to arrive at the 3-dB frequency bandwidth ($FWHM_\nu = \nu_h - \nu_l$) formula:

$$\Delta\Theta_{hl} = \theta_h - \theta_l = \frac{4\pi^2 n_g R_{ring}}{c_0} (\nu_h - \nu_l) \tag{3.31}$$

$$\nu_h - \nu_l = FWHM_\nu = \frac{c_0}{2\pi n_g R_{ring}} \frac{1}{\pi} \arccos \left(1 - \frac{(1 - |t_1 t_2| \alpha_s)^2}{2|t_1 t_2| \alpha_s} \right) \tag{3.32}$$

This expression is valid for all coupling strengths and contain no approximations. Nevertheless, in the weak coupling situations (small κ, large t), a more compact form of the equation can be reached, where it is possible to use the approximation, $\cos(\Phi) \approx 1 - \frac{\Phi^2}{2} => \Phi \approx \arccos\left(1 - \frac{\Phi^2}{2}\right)$:

$$FWHM_\nu \approx \frac{c_0}{2\pi n_g R_{ring}} \left(\frac{1 - |t_1 t_2| \alpha_s}{\sqrt{|t_1 t_2| \alpha_s}} \right) \tag{3.33}$$

It is also possible to write the FWHM in terms of the wavelength:

$$FWHM_\lambda \approx \frac{\lambda_m^2}{2\pi n_g R_{ring}} \arccos\left(1 - \frac{(1 - |t_1 t_2| \alpha_s)^2}{2|t_1 t_2| \alpha_s}\right) \tag{3.34}$$

$$FWHM_\lambda \approx \frac{\lambda_m^2}{2\pi n_g R_{ring}} \left(\frac{1 - |t_1 t_2| \alpha_s}{\sqrt{|t_1 t_2| \alpha_s}} \right) \tag{3.35}$$

The final expressions of 3-dB bandwidth (FWHM) completes the list of necessary terms to be defined for the analysis of the 1^{st} order add-drop ring resonator filter. In Figure 3.4, example FSR and

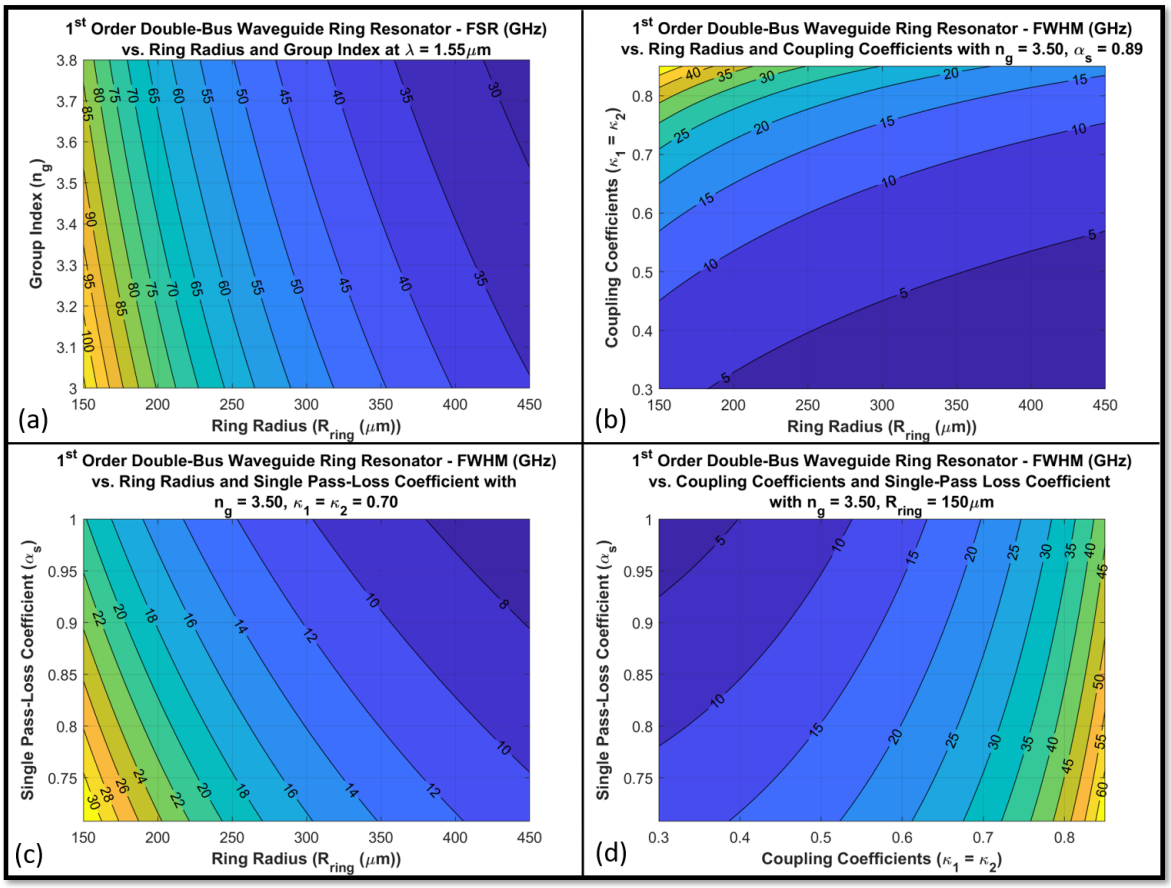

Figure 3.4: Free spectral range (a) and full-width at half-maximum (b)-(c)-(d) of the 1^{st} order ring resonator as a function of group index, ring radius, coupling coefficients and single pass-loss-coefficient

FWHM values for different parameters of the geometry are shown, which are quite useful in finding the required parameter ranges to satisfy the pre-determined KPIs. For convenience in wavelength interpretation of the values given in Figure 3.4, 0.20 nm bandwidth corresponds to 25 GHz. As a side note, the group index is set to a higher value than the assumed effective index in the initial spectrum analysis (see Figure 3.2).

A rough examination of Figure 3.4, as well as Eq. 3.22, Eq. 3.23, Eq. 3.33 and Eq. 3.35 shows that ring radius has an inverse impact on FSR and FWHM, indicating the availability of a low range of radius values to have sufficiently large bandwidth values. Strong couplings and higher losses appear to increase the FWHM, where the former is shown in Figure 6 to decrease IL and ER. Therefore, a care must be given to find a balance between the KPI values with the changes made on the system parameters. Considering the 37.5 GHz (0.30 nm) FWHM criterion, 150 μm ring radius becomes a strict necessity, yet it would only be adequate if high coupling values (e.g. $\kappa > 0.8$) can be reached. This is the main encountered problem with the InP material platform when ring resonator filter is considered, while having a bandwidth requirement that is relatively large. For example, it is significantly easier in SoI to achieve much lower bend radii, owing to the larger index contrast of the platform. This allows higher bandwidth values to be reached with Silicon, regarding the ring resonator geometry. In this sense, InP ring resonator filters are limited below certain bandwidth range, which proves to be a difficulty in this design process.

Nonetheless, with the results above, it is shown that tied to certain conditions, a ring resonator filter can be theoretically designed in InP and with this aim, the study of this geometry is studied further, the details of which are elucidated in Chapter 4. Furthermore, with the objective of increasing the filter performance, a higher-order structure is considered and a similar analysis to the theoretical derivations made for the first-order case is conducted in Appendix C.1. Allowing for a more uniform pass-band, as well as higher ER [47], this alternative is visited in an analytical analysis. Also, in order to enhance the FSR of the filter, the Vernier Effect is investigated as well, the details of which are provided with a short study in Appendix C.1.

3.2 Mach Zehnder Interferometer Filter Theory

Similar to the previous section on the ring resonator, S-matrix analysis will be employed here for the 1^{st} order MZI Filter. Most of the initial equations of this section are the same as the equations from the ring resonator theory and are repeated for the sake of completeness. Moreover, the further details of the 2^{nd} order case is provided in Appendix C.2, which is the extended version of the study that is carried out here.

The model of the 1^{st} order MZI filter is depicted in Figure 3.5, for which the relation between the outgoing fields (b_1&b_2) and the incoming fields (a_1&a_2) at the first coupling section can be written as (ports are defined the other way around in comparison with Eq. 3.3):

$$\begin{pmatrix} b_1 \\ b_2 \end{pmatrix} = \begin{pmatrix} t_1 & -\kappa_1^* \\ \kappa_1 & t_1^* \end{pmatrix} \begin{pmatrix} a_1 \\ a_2 \end{pmatrix} \tag{3.36}$$

where the subscript 1 denotes the coupling and transmission coefficients at the first coupling region.

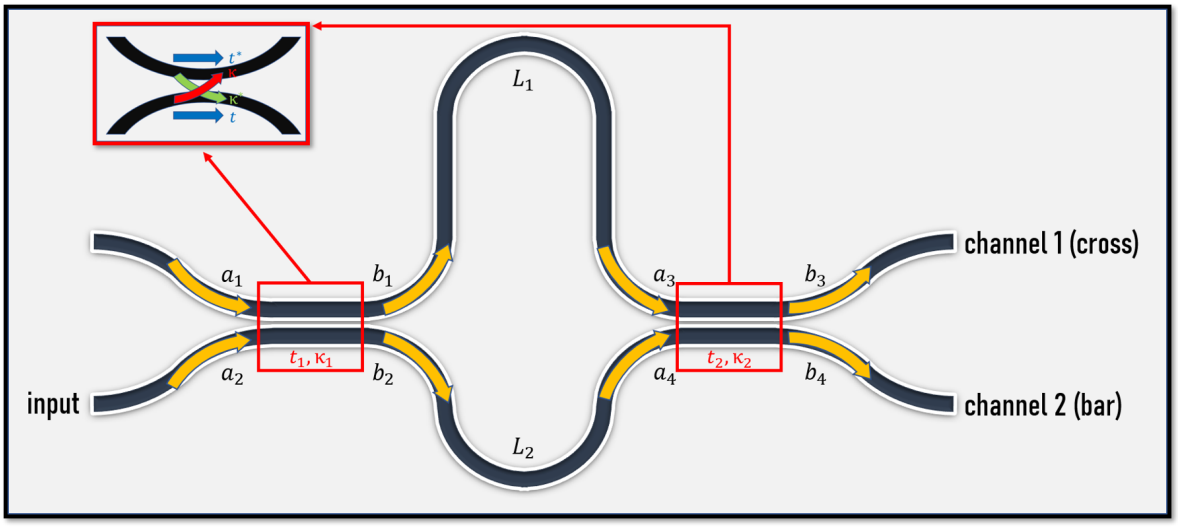

Figure 3.5: 1^{st} order MZI filter model

After travelling along the arms of the MZI, the field amplitudes are multiplied with amplitude transmission and phase factors as:

$$\begin{pmatrix} a_3 \\ a_4 \end{pmatrix} = \begin{pmatrix} e^{-\left(\frac{\alpha L_1}{2} - i\theta_1\right)} & 0 \\ 0 & e^{-\left(\frac{\alpha L_2}{2} - i\theta_2\right)} \end{pmatrix} \begin{pmatrix} b_1 \\ b_2 \end{pmatrix} \tag{3.37}$$

where the power attenuation coefficient, α [1/cm], which is defined in 3.5 is preferred here rather than the single-pass transmission coefficient, α_s, owing to the directional nature of the geometry. Nevertheless, the logarithmic conversion, $\alpha_{dB} = \frac{10}{ln(10)}\alpha$ from Eq. 3.6 is still valid here and can be made use of, if desired. The phase accumulation after a propagation on an interferometer arm, θ_i, is found by multiplying the propagation constant, β, and the respective arm length, Ł$_i$:

$$\theta_i = \beta L_i = \frac{2\pi n_{eff} L_i}{\lambda_0} \tag{3.38}$$

where λ_0 is the wavelength of the field in vacuum and n_{eff} is the effective index of the waveguide. Having the same structure as Eq. 3.36, the matrix at the second coupling region expresses the relation between the field amplitudes a_3, a_4 and b_3, b_4 as:

$$\begin{pmatrix} b_3 \\ b_4 \end{pmatrix} = \begin{pmatrix} t_2^* & \kappa_2 \\ -\kappa_2^* & t_2 \end{pmatrix} \begin{pmatrix} a_3 \\ a_4 \end{pmatrix} \tag{3.39}$$

Assuming an empty first port ($a_1 = 0$), the individual field amplitudes at the output channels are found by solving the system of equations presented above. The equations for the channel spectra are given in Eq. 3.40 and Eq. 3.41 as a function of the system parameters, namely being input field amplitude, coupling coefficients, arm lengths, as well as wavelength and effective index of the waveguides:

$$b_3 = a_4\kappa_2 + a_3 t_2^* = a_2\left(t_1\kappa_2 e^{-\left(\frac{\alpha L_2}{2} - i\theta_2\right)} + \kappa_1 t_2^* e^{-\left(\frac{\alpha L_1}{2} - i\theta_1\right)}\right) \tag{3.40}$$

$$b_4 = a_4 t_2 - a_3\kappa_2^* = a_2\left(t_1 t_2 e^{-\left(\frac{\alpha L_2}{2} - i\theta_2\right)} - \kappa_1\kappa_2^* e^{-\left(\frac{\alpha L_1}{2} - i\theta_1\right)}\right) \tag{3.41}$$

with $\theta_i = \beta L_i = \frac{2\pi n_g L_i}{\lambda_0}$ and $|t_i|^2 + |\kappa_i|^2 = 1$, where $i \in \{1, 2\}$.

The field powers at the cross (channel 1) and the bar (channel 2) ports can be also written by taking the absolute square of the respective field amplitudes, namely b_3 and b_4:

$$P_{cross} = |b_3|^2 = |a_2|^2\left(|t_1\kappa_2|^2 e^{-\alpha L_2} + |\kappa_1 t_2|^2 e^{-\alpha L_1} + 2e^{-\frac{\alpha(L_1+L_2)}{2}} Re\{\kappa_1^*\kappa_2 t_1 t_2 e^{i(\theta_2-\theta_1)}\}\right) \tag{3.42}$$

$$P_{cross} = |b_3|^2 = |a_2|^2\left(|t_1 t_2|^2 e^{-\alpha L_2} + |\kappa_1\kappa_2|^2 e^{-\alpha L_1} - 2e^{-\frac{\alpha(L_1+L_2)}{2}} Re\{\kappa_1^*\kappa_2 t_1 t_2 e^{i(\theta_2-\theta_1)}\}\right) \tag{3.43}$$

Here, the cross port refers to the output channel on the opposite side of the input port with respect to the propagation axis, whereas the bar port is located on the same side as the input port. With the assumed geometry in Figure 3.5, they are also denoted as channel 1 and 2, respectively. Rewriting the output channel powers allow to obtain more compact forms, which are easier to interpret with the cosine terms indicating the periodic nature of the spectra:

$$P_{cross} = |b_3|^2 = |a_2|^2\left(|t_1\kappa_2|^2 e^{-\alpha L_2} + |\kappa_1 t_2|^2 e^{-\alpha L_1} + 2|\kappa_1\kappa_2 t_1 t_2| e^{-\frac{\alpha(L_1+L_2)}{2}} \cos(\varphi - \Delta\theta)\right) \tag{3.44}$$

$$P_{cross} = |b_3|^2 = |a_2|^2\left(|t_1 t_2|^2 e^{-\alpha L_2} + |\kappa_1\kappa_2|^2 e^{-\alpha L_1} - 2|\kappa_1\kappa_2 t_1 t_2| e^{-\frac{\alpha(L_1+L_2)}{2}} \cos(\varphi - \Delta\theta)\right) \tag{3.45}$$

where the coupling and transmission terms are transformed to amplitude-phase form as $\kappa_1^*\kappa_2 t_1 t_2 = |\kappa_1\kappa_2 t_1 t_2| e^{i\varphi}$ and phase accumulation difference term between the arms, $\Delta\theta = (\theta_1 - \theta_2)$, is defined for brevity.

Example cross and bar channel spectra with different coupling coefficients are plotted between 1548 nm and 1552 nm in Figure 3.6, where the effective index is chosen to has the same value as in the ring resonator example, arm lengths are set arbitrarily and may not represent the actual design values. The same is also valid for the loss coefficient, where the value is determined through estimation.

The first evident feature of the two channel responses is that the resonances are shifted by π radians with respect to each other. This can also be observed from Eq. 3.44 and Eq. 3.45, where the cosine terms have different signs in both equations. The equations also point out another distinctive characteristic of two channel outputs in the first two amplitude terms, in which different coupling/transmission coefficient combinations are present for the two ports, leading to a significant difference in the spectral responses seen in Figure 3.6. The ER and pass-band width (FWHM) appear to be indifferent

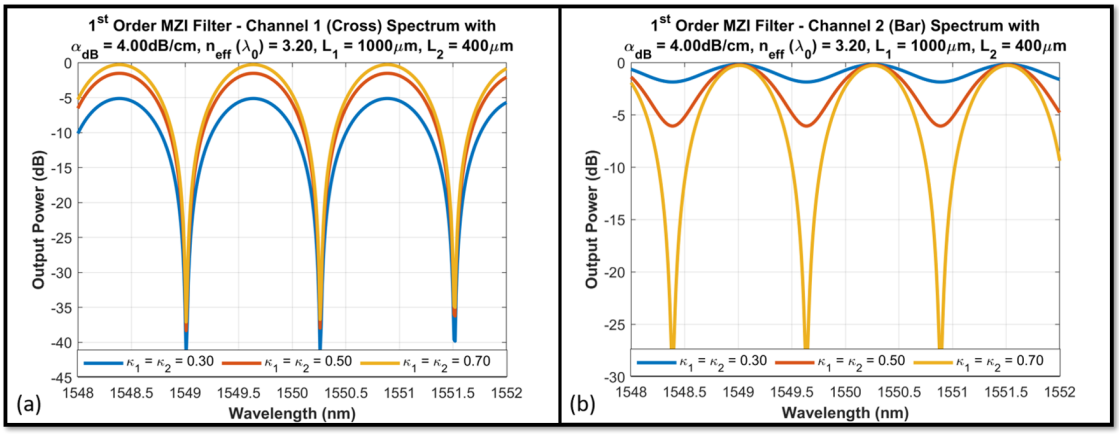

Figure 3.6: Output power spectra of the (a) Cross and (b) Bar channels of the 1^{st} order MZI filter

to changes in the coupling coefficients in the cross channel (Figure 3.6a), where the exact contrary can be said for the bar channel (Figure 3.6b). On the other hand, the IL is sensitive to changes in the cross port, which is not the case in the bar port of the MZI filter. For further investigation of the channel characteristics, the equations for the IL and ER are derived, which requires the transfer function definitions for the channels, that are found from Eq. 3.44 and 3.45:

$$T_1 = \frac{|b_3|^2}{|a_2|^2} = \left(|t_1\kappa_2|^2 e^{-\alpha L_2} + |\kappa_1 t_2|^2 e^{-\alpha L_1} + 2|\kappa_1\kappa_2 t_1 t_2| e^{-\frac{\alpha(L_1+L_2)}{2}} \cos(\varphi - \Delta\theta)\right) \tag{3.46}$$

$$T_2 = \frac{|b_4|^2}{|a_2|^2} = \left(|t_1 t_2|^2 e^{-\alpha L_2} + |\kappa_1\kappa_2|^2 e^{-\alpha L_1} - 2|\kappa_1\kappa_2 t_1 t_2| e^{-\frac{\alpha(L_1+L_2)}{2}} \cos(\varphi - \Delta\theta)\right) \tag{3.47}$$

Starting with the IL, Eq. 3.46 and Eq. 3.47 are calculated at resonance, where the cosine terms take the value of 1 and -1 for channel 1 and 2, respectively.

$$IL_1 = -10\log_{10}(T_{1,0}) = -10\log_{10}\left(|t_1\kappa_2|^2 e^{-\alpha L_2} + |\kappa_1 t_2|^2 e^{-\alpha L_1} + 2|\kappa_1\kappa_2 t_1 t_2| e^{-\frac{\alpha(L_1+L_2)}{2}}\right) \tag{3.48}$$

$$IL_2 = -10\log_{10}(T_{2,0}) = -10\log_{10}\left(|t_1 t_2|^2 e^{-\alpha L_2} + |\kappa_1\kappa_2|^2 e^{-\alpha L_1} + 2|\kappa_1\kappa_2 t_1 t_2| e^{-\frac{\alpha(L_1+L_2)}{2}}\right) \tag{3.49}$$

Figure 3.7 depicts how the different parameters of the system affect the IL of the individual channels. When symmetrical coupling coefficients are used ($\kappa_1 = \kappa_2$), 3-dB power splitting ($\kappa_1 = \kappa_2 = \frac{1}{\sqrt{2}} \approx 0.71$) minimizes the IL of channel 1 (Figure 3.7a), whereas channel 2 IL decreases with smaller coupling coefficients (Figure 3.7c). In both cases, having lower waveguide losses reduces the IL of the filter, as would intuitively be expected. For non-symmetrical coupling coefficients, channel 2 is negatively

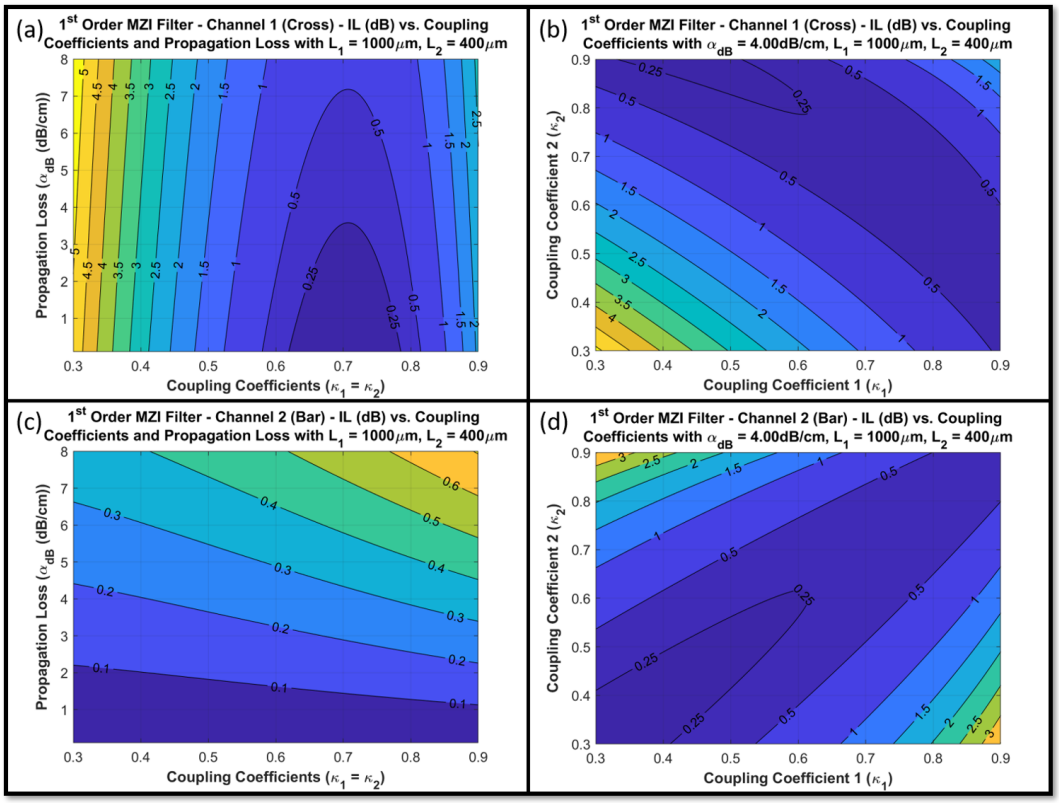

Figure 3.7: Insertion loss (dB) of the 1^{st} order MZI filter for channel 1 (a-b) and channel 2 (c-d) as a function of coupling coefficients and propagation losses

affected with increasing IL as the separation between the coefficients increase (Figure 3.7d). This is, however not necessarily the case for channel 1, where IL appears to attain its minimum values around a band that makes the multiplications of the coefficients to be 0.5 (Figure 3.7b). Moreover, the same minimum IL band for channel 1 contains also the symmetrical 3-dB power splitting case. As the coefficient configurations get further separated from this optimum range, IL values tend to increase as observed from the figure.

The on-off ER is the next term to be studied in the context of 1^{st} order MZI filter, which is found by taking the ratio of the on-resonance power to the off-resonance power. For channel 1 and channel 2, the corresponding expressions are found as:

$$ER_1 = 10\log_{10}\left(\frac{\arg\max_{\lambda}(T_1)}{\arg\min_{\lambda}(T_1)}\right) = 10\log_{10}\left(\frac{|t_1\kappa_2|^2e^{-\alpha L_2} + |\kappa_1 t_2|^2e^{-\alpha L_1} + 2|\kappa_1\kappa_2 t_1 t_2|e^{-\frac{\alpha(L_1+L_2)}{2}}}{|t_1\kappa_2|^2e^{-\alpha L_2} + |\kappa_1 t_2|^2e^{-\alpha L_1} - 2|\kappa_1\kappa_2 t_1 t_2|e^{-\frac{\alpha(L_1+L_2)}{2}}}\right) \quad (3.50)$$

$$ER_2 = 10\log_{10}\left(\frac{\arg\max_{\lambda}(T_2)}{\arg\min_{\lambda}(T_2)}\right) = 10\log_{10}\left(\frac{|t_1 t_2|^2e^{-\alpha L_2} + |\kappa_1\kappa_2|^2e^{-\alpha L_1} + 2|\kappa_1\kappa_2 t_1 t_2|e^{-\frac{\alpha(L_1+L_2)}{2}}}{|t_1 t_2|^2e^{-\alpha L_2} + |\kappa_1\kappa_2|^2e^{-\alpha L_1} - 2|\kappa_1\kappa_2 t_1 t_2|e^{-\frac{\alpha(L_1+L_2)}{2}}}\right) \quad (3.51)$$

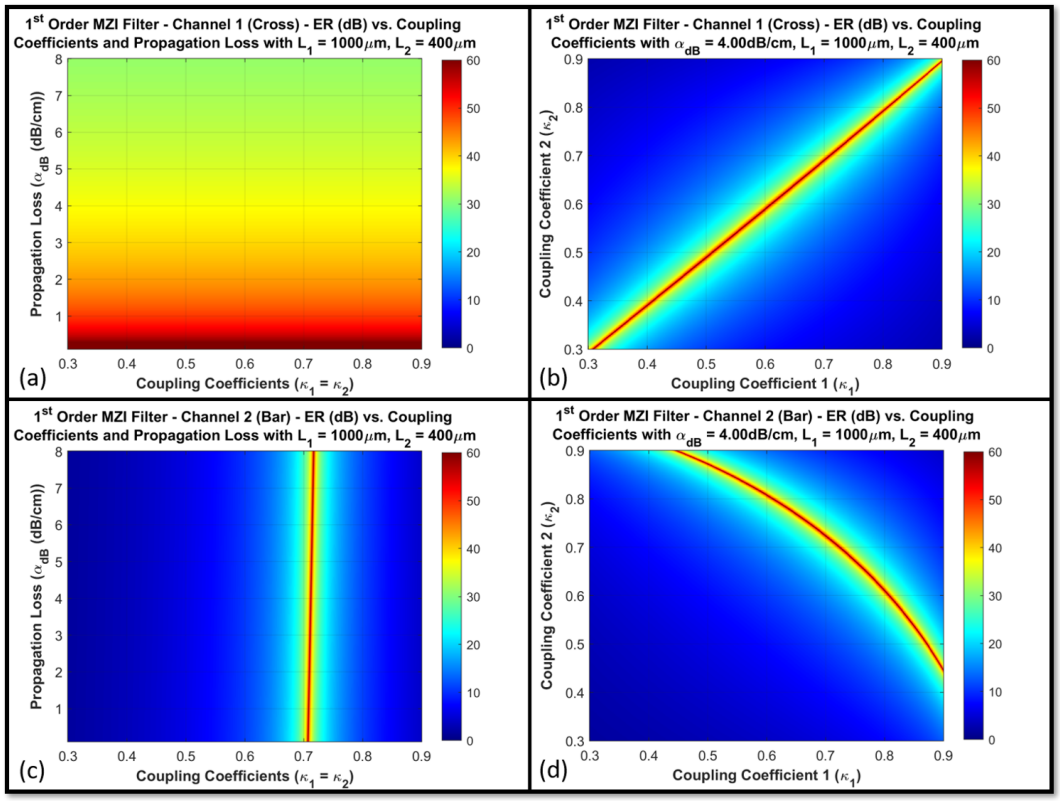

Figure 3.8: Extinction ratio (dB) of the 1^{st} order MZI filter for channel 1 (a-b) and channel 2 (c-d) as a function of coupling coefficients and propagation losses

Although the equations may seem difficult to interpret upon initial observation, the resulting plots in Figure 3.8 allow for easy understanding of the parameters' effects on the ER for the two channels. Different from before, plots are generated in colormap this time, since the values increase significantly around certain values and demonstrating those steep changes proved to be difficult by using a contour map as it was done with the IL plots in Figure 3.7.

The most obvious difference between the cross and bar ports can be seen from Figure 3.8a and Figure 3.8c, where the ER is almost indifferent to the value of the coupling coefficients for channel 1, as long as the coupling is symmetrical. On the contrary, only a small selection of coefficients ensures the maximization of the ER in channel 2, the value of which corresponds to 3-dB coupling for a lossless waveguide. Independent of the coupling values, loss decreases the ER for channel 1 as expected (Figure 3.8a). Yet not so intuitively, it slightly shifts the band of the optimum coupling values for channel 2 (Figure 3.8c). On the other hand, symmetrical coupling can be seen to enhance the ER for channel 1 considerably (Figure 3.8b), whereas the maximized value range for channel 2 seem to follow the trend seen in Figure 3.7b for the IL, with the requirement of being in the vicinity of 0.5 in the multiplication of the two coupling coefficients (Figure 3.8d). Surely here as well, the 3-dB power splitting is included in this band. This condition can be attributed to the joint presences of the coupling coefficients in the second amplitude term of the Eq. 3.51, as well as the transmission coefficients in the first term,

Likewise, the symmetrical coupling condition of channel 1 can be linked to the mixed terms in Eq. 3.50.

Continuing with the resonance condition as it was done in the ring resonator filter, the on-off resonances in the channels take place when the last terms in the transfer functions (Eq. 3.46 and Eq. 3.47) attain the maximum-minimum value with the phase components being equal to an odd or even multiples of π. This happens when the difference between the phase accumulations in the arms of the MZI, θ_1 and θ_2, satisfies:

$$\begin{aligned} &Channel\,1: \quad \Delta\theta_{m,1} = \beta_{m,1}(L_1 - L_2) = \frac{2\pi n_{eff}\Delta L}{\lambda_{m,1}} = \frac{2\pi n_{eff}\Delta L}{c_0}\nu_{m,1} = (2\pi m + \varphi), \qquad m \in \mathbb{N} \\ &Channel\,2: \quad \Delta\theta_{m,2} = \beta_{m,2}(L_1 - L_2) = \frac{2\pi n_{eff}\Delta L}{\lambda_{m,2}} = \frac{2\pi n_{eff}\Delta L}{c_0}\nu_{m,2} = (2\pi m + \varphi + \pi), \quad m \in \mathbb{N} \end{aligned} \tag{3.52}$$

where m denotes the resonance number and $\Delta L = (L_1 - L_2)$ is defined as the length difference between the arms of the interferometer. When the phase matching conditions in Eq. 3.52 are satisfied, it allows the fields in the interferometer arms to constructively interfere at the coupling region. The phase term φ has a constant value between 0 and 2π, thus it can be negligible, if m is not small. Nevertheless, it should not be disregarded when an accurate analysis is required. With this consideration, the resonances for channel 1 can be written as:

$$\nu = m\frac{c_0}{n_{eff}\Delta L} \tag{3.53}$$

$$m\lambda_m = n_{eff}\Delta L \tag{3.54}$$

In the case of channel 2, the π phase term shifts the resonance by half-wavelength, where the m in Eq. 3.54 is replaced by $m + 0.5$. Following the resonance definitions, the FSR of the MZI filter can be found easily from Eq. 3.53 and Eq. 3.54, which becomes the same for both channels, regardless of their different exact resonance values:

$$FSR_\nu = \nu_{m+1} - \nu_{m+1} = \frac{c_0}{n_g\Delta L} \tag{3.55}$$

$$FSR_\lambda \approx \Delta\nu_{FSR}\frac{\lambda_m^2}{c_0} \approx \frac{\lambda_m^2}{n_g\Delta L} \tag{3.56}$$

where n_g is the group index, which was defined in Eq. 3.24.

The final term to be derived in this analysis for the MZI filter is the FWHM. For reasons of brevity, the focus here will be on channel 2 but the expression for the channel 1 will be provided at the end as well. Using Eq. 3.47, 3-dB bandwidth can be found by taking the ratio of the power at the bandwidth limits to the resonance power and then equating to 1/2:

$$\frac{1}{2} = \left(\frac{|t_1t_2|^2e^{-\alpha L_2} + |\kappa_1\kappa_2|^2e^{-\alpha L_1} - 2|\kappa_1\kappa_2t_1t_2|e^{-\frac{\alpha(L_1+L_2)}{2}}\cos(\varphi - \Delta\theta)}{|t_1t_2|^2e^{-\alpha L_2} + |\kappa_1\kappa_2|^2e^{-\alpha L_1} + 2|\kappa_1\kappa_2t_1t_2|e^{-\frac{\alpha(L_1+L_2)}{2}}}\right) \tag{3.57}$$

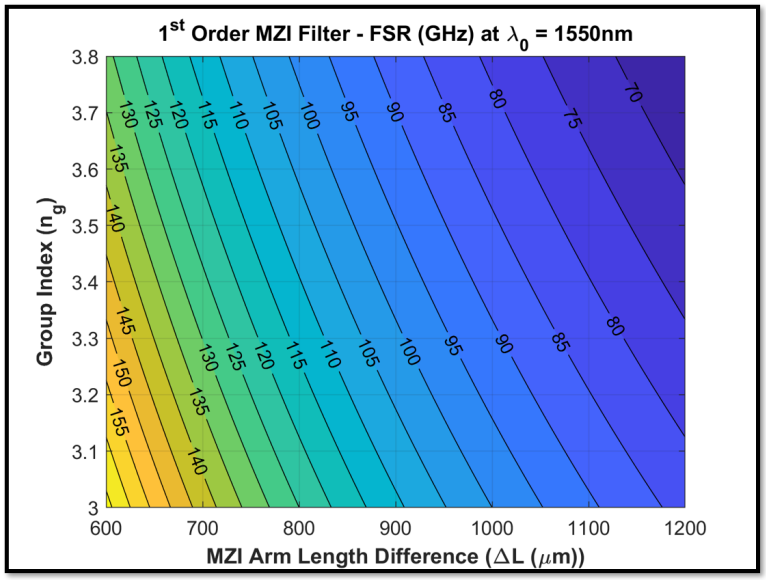

Figure 3.9: FSR (GHz) of the 1^{st} order MZI filter as a function of group index and arm length difference

Finding the two solutions of Eq. 3.57 yields the lower frequency limit, $\Delta\theta_l$, and the higher limit, $\Delta\theta_h$:

$$\Delta\theta_l = \varphi - \pi - \arccos\left(1 - \frac{(|t_1t_2|e^{-\frac{\alpha L_2}{2}} + |\kappa_1\kappa_2|e^{-\frac{\alpha L_1}{2}})^2}{4|\kappa_1\kappa_2t_1t_2|e^{-\frac{\alpha(L_1+L_2)}{2}}}\right) \tag{3.58}$$

$$\Delta\theta_h = \varphi - \pi + \arccos\left(1 - \frac{(|t_1t_2|e^{-\frac{\alpha L_2}{2}} + |\kappa_1\kappa_2|e^{-\frac{\alpha L_1}{2}})^2}{4|\kappa_1\kappa_2t_1t_2|e^{-\frac{\alpha(L_1+L_2)}{2}}}\right) \tag{3.59}$$

the difference of which is interesting for obtaining the FWHM:

$$\Delta\theta_h - \Delta\theta_l = 2\arccos\left(1 - \frac{(|t_1t_2|e^{-\frac{\alpha L_2}{2}} + |\kappa_1\kappa_2|e^{-\frac{\alpha L_1}{2}})^2}{4|\kappa_1\kappa_2t_1t_2|e^{-\frac{\alpha(L_1+L_2)}{2}}}\right) \tag{3.60}$$

With this finding, initial formula (Eq. 3.52) for the phase accumulation term containing the frequency dependency can be written for both limits, the difference of which results in the 3-dB frequency bandwidth ($FWHM_\nu = \nu_h - \nu_l$):

$$\Delta\theta_{hl} = \Delta\theta_h - \Delta\theta_l = \frac{2\pi n_g \Delta L}{c_0}(\nu_h - \nu_l) \tag{3.61}$$

$$(\nu_h - \nu_l) = FWHM_{\nu,2} = \frac{c_0}{\pi n_g \Delta L}\arccos\left(1 - \frac{(|t_1t_2|e^{-\frac{\alpha L_2}{2}} + |\kappa_1\kappa_2|e^{-\frac{\alpha L_1}{2}})^2}{4|\kappa_1\kappa_2t_1t_2|e^{-\frac{\alpha(L_1+L_2)}{2}}}\right) \tag{3.62}$$

In terms of the wavelength, FWHM becomes:

$$FWHM_{\lambda,2} \approx \frac{\lambda_m^2}{\pi n_g \Delta L}\arccos\left(1 - \frac{(|t_1t_2|e^{-\frac{\alpha L_2}{2}} + |\kappa_1\kappa_2|e^{-\frac{\alpha L_1}{2}})^2}{4|\kappa_1\kappa_2t_1t_2|e^{-\frac{\alpha(L_1+L_2)}{2}}}\right) \tag{3.63}$$

Similar steps can be followed for channel 1 and the corresponding FWHM are found as:

$$FWHM_{\nu,1} = \frac{c_0}{\pi n_g \Delta L} \arccos\left(1 - \frac{(|t_1\kappa_2|e^{-\frac{\alpha L_2}{2}} + |\kappa_1 t_2|e^{-\frac{\alpha L_1}{2}})^2}{4|\kappa_1\kappa_2 t_1 t_2|e^{-\frac{\alpha(L_1+L_2)}{2}}}\right) \tag{3.64}$$

$$FWHM_{\lambda,1} \approx \frac{\lambda_m^2}{\pi n_g \Delta L} \arccos\left(1 - \frac{(|t_1\kappa_2|e^{-\frac{\alpha L_2}{2}} + |\kappa_1 t_2|e^{-\frac{\alpha L_1}{2}})^2}{4|\kappa_1\kappa_2 t_1 t_2|e^{-\frac{\alpha(L_1+L_2)}{2}}}\right) \tag{3.65}$$

Example graphs for the relations between the system parameters (group index, MZI arm length difference, coupling and loss coefficients) and FSR, as well as FWHM are generated for the cross and bar ports of the 1^{st} order MZI filter from the Eq. 3.55, Eq. 3.62 and Eq. 3.64 and summarized in Figure 3.9 and Figure 3.10. Considering a relatively small range of possible values for the group index, which is not necessarily a free parameter, the fundamental decisive factor on both FWHM and FSR becomes the arm-length difference for the outputs that has an inverse effect due to being in the denominator of the above-mentioned equations. Inspection of Figure 3.9 implies the 800-1000 nm arm length difference range to be not convenient for the KPI criterion on the FSR, which actually

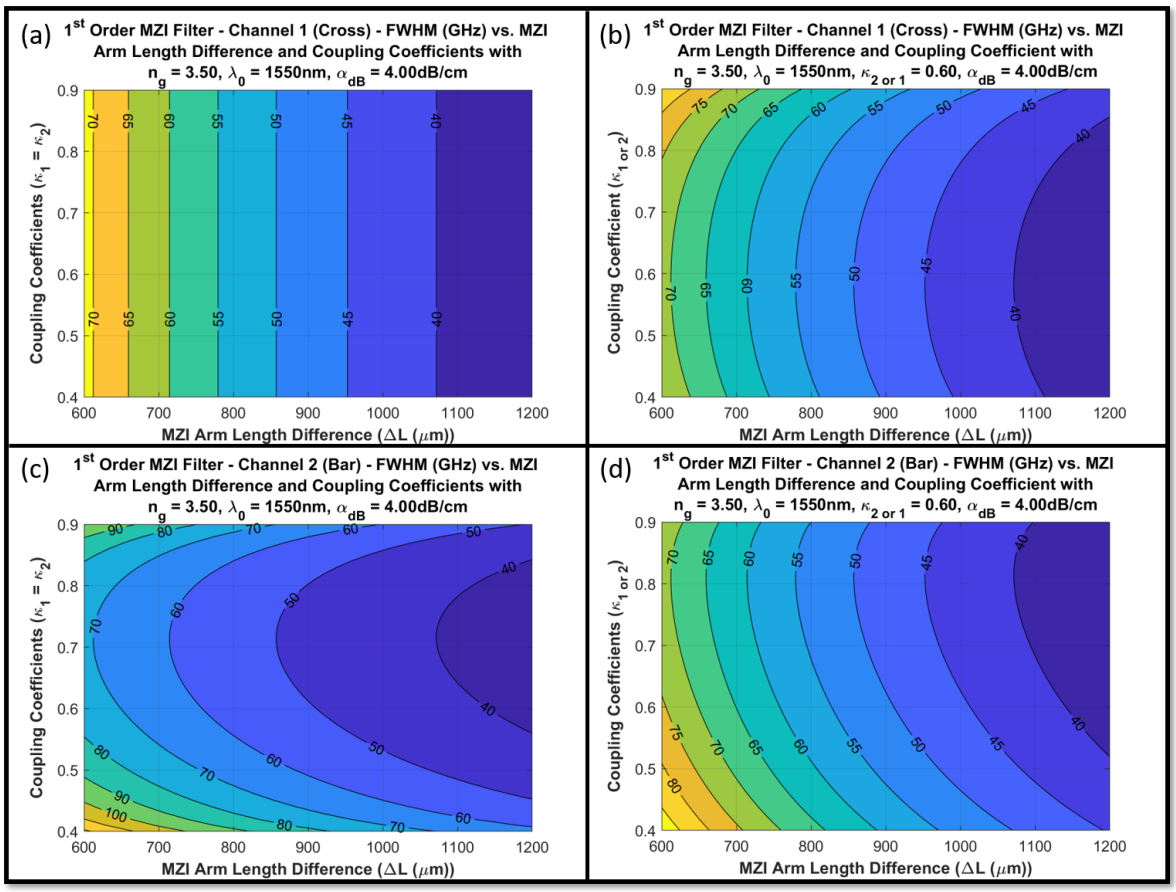

Figure 3.10: FWHM (GHz) of the 1^{st} order MZI filter for channel 1 (a-b) and channel 2 (c-d) as a function of coupling coefficients and arm length differences

should be different from 100 GHz (0.80 nm), so that neighboring channels do not coincide with the side-resonances. In terms of the FWHM, the inflexibility of the MZI filter to the coupling coefficients can be observed from Figure 3.10 in general, when a comparison is made to the ring resonator results in Figure 3.4, where 10-fold FWHM increases could be seen in the same range of coupling values there. This is especially obvious in Figure 3.10a, in which symmetrical coupling results in almost invariable FWHM values for the cross channel. Nevertheless, bar channel shows a variation to the values of κ in Figure 3.10c, where the condition of the coefficient multiplications to be equal to 0.5 seems to minimize the bandwidth, as can be also inferred from Eq. 3.62. This was not predicted from the initial literature research, though the range of bandwidth adjustment is still relatively small. On the other hand, Figure 3.10b (channel 1) and Figure 3.10d (channel 2) shows another distinction between the two channel responses, where one of the coupling coefficients (here denoted as $\kappa_{2\,or\,1} = 0.6$) are fixed to a certain value and the other is changed, as well as the MZI arm length difference. For channel 1, the minimum bandwidth value is achieved for symmetrical coupling (when $\kappa_{1\,or\,2} = 0.6$), yet channel 2 attains its lowest bandwidth value when the previously mentioned coupling multiplication condition is satisfied (when $\kappa_{1\,or\,2} = \frac{0.5}{0.6}$). Moreover, the effect of loss on bandwidth values are found to be negligible on the bandwidths for each port, which is the reason why loss studies are not included in Figure 3.10. To meet the 37.5 GHz (0.30 nm) FWHM criterion, at least mm-length arm length differences seem to be necessary, which however would decrease FSR significantly. With the 1st order geometry, it is difficult to flexibly adjust the ratio between FSR and FWHM, with nm-FSR and sub nm-FWHM filter could be realized. For this purpose, Vernier Effect can be employed, which suggests the usage of a higher-order filter with different arm length differences. In the next chapter on the methodology used with the MZI filter, 2^{nd} order structure would be considered for that reason, the theory of which can be found in Appendix C.2. For the goal of introducing the theoretical foundations of the MZI filter, the detailed 1^{st} order analysis of this section is considered sufficient at this point.

Chapter 4

Methodology

4.1 Ring Resonator Filter Design Process

Having completed the theoretical investigation of the ring resonator filter with the S-matrix analysis, KPI testing is initially carried out for checking the viability of the geometry. With the 1^{st} order ring resonator, the minimum requirement for at least one of the three indicators (FWHM, IL or ER) could not be satisfied for any combination of the coupling coefficients. Incrementing the filter order by one (2^{nd} order filtering) resulted in promising spectra, yet only for relatively high coupling coefficients (e.g. $\kappa > 0.8$). Example comparison plots are generated and can be inspected in Figure 4.1. For both the 1^{st} and 2^{nd} order filters, 45% power transfer at each ring-bus coupling region ($\kappa_1 = \kappa_2 = 0.67$) are represented by the blue lines for both 1st and 2nd order filters. The intermediate coupling strengths between the two rings of the 2^{nd} order filter are chosen to yield flat-top responses ($\kappa_{int,1} = 0.36$ & $\kappa_{int,2} = 0.68$). For more information on the model used for the 2^{nd} order case, Appendix C.1 provides a detailed investigation. The radius for both rings is set to 150 μm, in order to obtain the highest possible FWHM. Moreover, green, yellow, orange and red colored backgrounds on the table below the figures represent perfect, good, satisfactory and unsatisfactory values for each criterion (see Table 2.1).

With the initial parameters explained above and given in the figure, the 1^{st} order filter can be seen to satisfy IL and ER requirements, whereas the FWHM remains unsatisfactory for the blue curve. Increasing the coupling to result in 64% power transfer for both coefficients ($\kappa_1 = \kappa_2 = 0.80$) allows perfectly meeting the FWHM and IL, whereas this time ER falls below the minimum requirement of 10 dB. In the 2^{nd} order filter, a similar trade-off can be observed. Attempting to satisfy the FWHM by increasing the coupling coefficients reduces the ER significantly. Nevertheless, it is possible to find parameter combinations that satisfy all criteria (FWHM, IL and ER) at least on the satisfactory level, one of which can be seen in the orange curve of Figure 4.1b.

With this motivation, the analytical study carried out until this point is followed by developing a physical model and simulating the ring resonator geometry by referring to computational means of calculation. For this purpose, a commercially available software called "Synopsys Photonic Solutions – RSoft" (shortly will be called RSoft) is used. The tools package of the software incorporates dif-

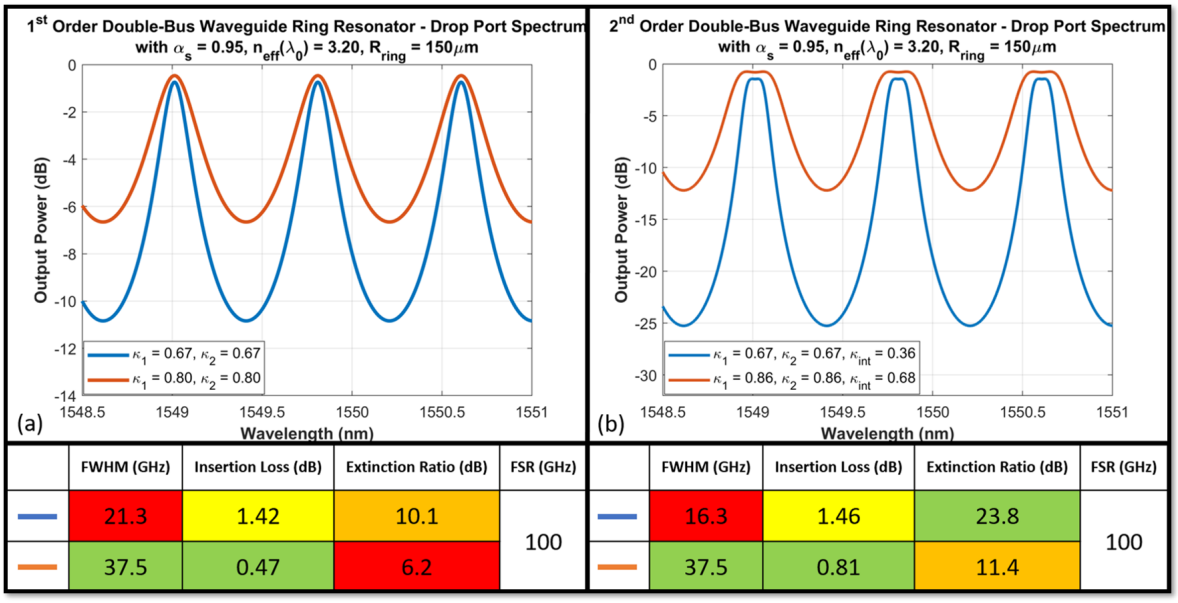

	FWHM (GHz)	Insertion Loss (dB)	Extinction Ratio (dB)	FSR (GHz)
—	21.3	1.42	10.1	100
—	37.5	0.47	6.2	

	FWHM (GHz)	Insertion Loss (dB)	Extinction Ratio (dB)	FSR (GHz)
—	16.3	1.46	23.8	100
—	37.5	0.81	11.4	

Figure 4.1: Drop port spectra for (a) 1^{st} and (b) 2^{nd} order ring resonators with example parameters

ferent simulation methods for solving electromagnetic equations, such as Beam Propagation Method (BPM), Eigen-Mode Expansion (EME) and Finite-Difference Time-Domain (FDTD). In this sense, each available option is considered for simulating the physics of the system. Since the BPM and the EME methods are direction dependent, they are regarded as being unsuitable for the investigation of the curved geometry of ring resonators. The alternative simulation method, namely FDTD, is a versatile and robust method of calculating the electromagnetic equations in time-domain, which would also be useful in following the transient response of the filter. However, it is a computationally heavy method and the 3D simulations for a ring resonator with the minimum radius of 150 μm would require significantly long computation times for sufficiently high spatial resolutions. This is primarily due to the large central region in the ring resonator structure, which is included in the simulation domain but not relevant for the simulation itself, which renders the computational burden unnecessarily large. Applying non-uniform meshing to the inner area of the ring also proved to be a nonviable solution against this problem. Due to having the unused inner region sharing its two axes (except the height axis) with the propagation axes of the ring waveguide, it is not possible to use separate spatial resolution grids inside and along the ring waveguides for two dimensions.

Therefore, the main issue with utilizing FDTD in the context of ring resonator filter design on InP initially emerged as the large dimensions of the structure due to the chosen material platform. As a workaround, an alternative methodology is proposed and tested by combining S-matrix simulations in MATLAB and 2D-FDTD simulations in RSoft. Having the potential of offering guidance to similar studies, the idea behind this framework emerged by dividing the geometry in separate regions where different physical phenomena take place. Outside the coupling regions, ring resonator only introduces phase shifts which could be easily simulated and predicted by the S-matrix formalism. In this sense, simulating the structure only at the coupling regions would allow for the extraction of the coupling

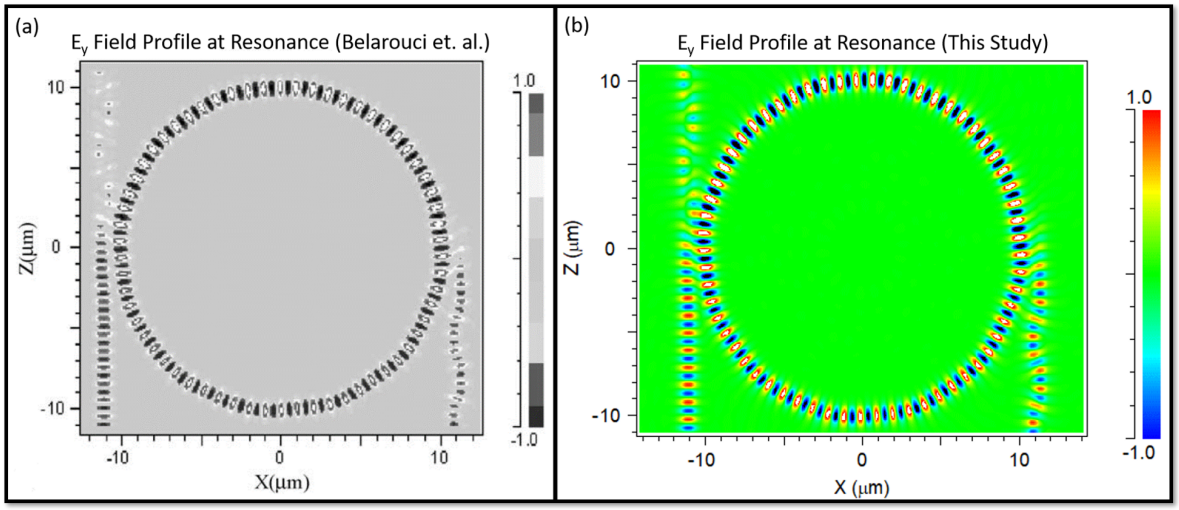

Figure 4.2: Field profile comparison at a resonance between (a) Belarouci et. al. and (b) this study

coefficients. Likewise, calculating the effective index and losses of a waveguide for different wavelengths and integrating these findings into the already developed S-matrix model should be sufficient for simulating the physics of the ring resonator structure. With this method, the necessity of the FDTD simulations for quite long times would be revoked and a computationally-efficient alternative can yield the same result.

To this end, a reference study is first taken into consideration and used for comparison purposes, which is focused on the 2D-FDTD simulations of a 10 μm radius ring resonator [50]. The width and coupling gap of the waveguides are set to 1 μm and 100 nm, respectively; while the core and the cladding material indices are set as 1.6 and 1 for any wavelength. Figure 4.2 shows the y component of the steady state electric field profile obtained at resonance in both studies, where input fields are excited from the waveguide at the bottom left corner. A strong resemblance between the two results can be seen, where the field profile in Figure 4.2b is generated by using 35 points per wavelength (ppw) grids in x and z axes, although the spatial resolution in the reference study was not specified. Additionally, the pass port power spectra comparison is carried out by using 60 nm of spatial resolution in both axes, which also shows a well correspondence to the study of Belarouci et. al. [50] (see Figure 4.3a). An inspection of the spectra comparison reveals different values of transmission power at resonances between two studies, which can be explained by the simulation duration. As the fields are simulated for higher number of round-trips, a better convergence in the ring resonator can be ensured, which is assumed to be the reason behind the different power values calculated at resonances. Moreover, it is necessary to mind the relation between the spatial resolution and the accuracy of the simulations. That being said, different spatial resolution grids are simulated to see their effects on the resonance wavelengths of the signal spectra. As shown in Figure 4.3b, the convergence of the results take place after approximately 25 ppw resolution, below which the outputs show a wide range of variety in terms of both the power values and the resonance wavelengths.

Confirming the validity of the initial FDTD simulations, the waveguide width is reduced to 600

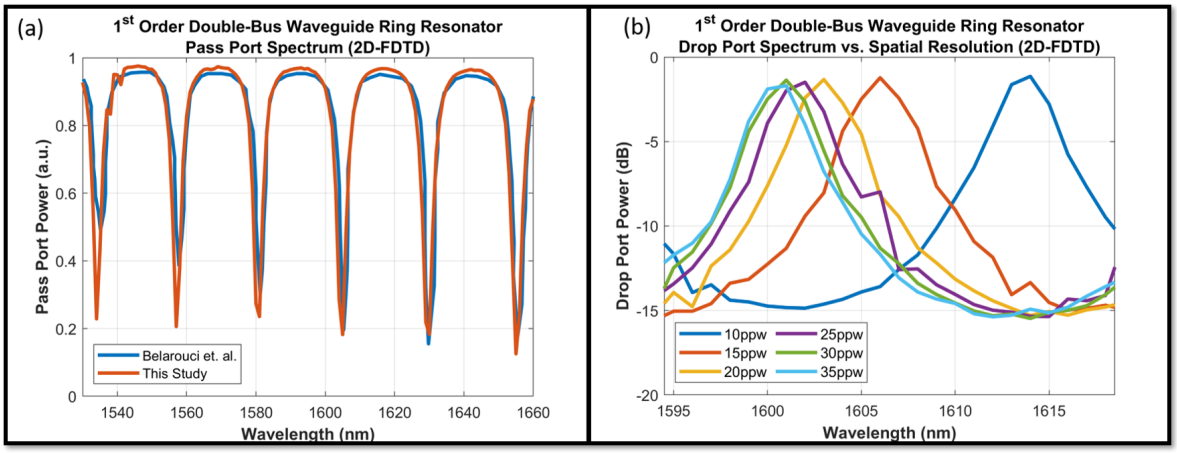

Figure 4.3: (a) Pass port power comparison between the study of Belarouci et.al. and this study - (b) Drop port resonance wavelength comparison between different spatial resolutions in x and z axes using 2D-FDTD simulations

nm to have a single-mode supporting geometry. Because the waveguides with 1 μm width allowed for the excitation of two modes, this resulted in different coupling coefficient strengths (from the input to the ring waveguide and vice versa) at individual coupling regions, conflicting with one of the core assumptions of the S-matrix model being used ($\kappa_{in=>ring} = \kappa_{ring=>in}$). The multi-mode nature of the default waveguide can be seen from the oscillatory field behavior at the pass and drop ports in Figure 4.2. The generation of a centrally aligned slab mode at the input waveguide only excites a single mode, due to the symmetrical interaction with the waveguide. However, when this mode couples to the ring waveguide at the first interface, the lateral excitation allows for the energy transfer to first two modes that the waveguide supports, which propagate through the ring and first couple to the drop port, then back to the pass port after a full-round trip. Only a single waveguide mode couples to two modes in the initial coupling from input to ring waveguide, whereas two modes of the ring waveguide excite two modes of the pass waveguide. As a result of this difference between the input-ring and ring-pass coupling, the assumption of the equal amplitude coupling coefficients (can be seen in Eq. 3.2 or Figure 3.1b) for both coupling directions in the S-matrix becomes insufficient in the physical representation of this geometry. Hence, in order to have a single-mode supporting geometry that would be convenient to work with and is also compatible with the developed S-matrix model, the waveguide width is set to 600 nm and further simulations are carried out with a narrower waveguide version of the geometry used in the work of Belarouci et. al. [50].

In order to model the existing ring resonator geometry successfully, it is necessary to include the wavelength dependency of the effective index of the waveguide modes and the coupling coefficients at the bus-ring coupling sections. Especially these two parameters play important role in the response of the system and their dispersion need to be considered. A well representation of the coupling coefficients and the phase accumulation of the fields would be mostly sufficient for these purposes, the proof of which will be provided with the comparison results carried out below. Moreover, due to the strong field confinement of the structure, losses in the idealized 2D simulation are found to be quite low.

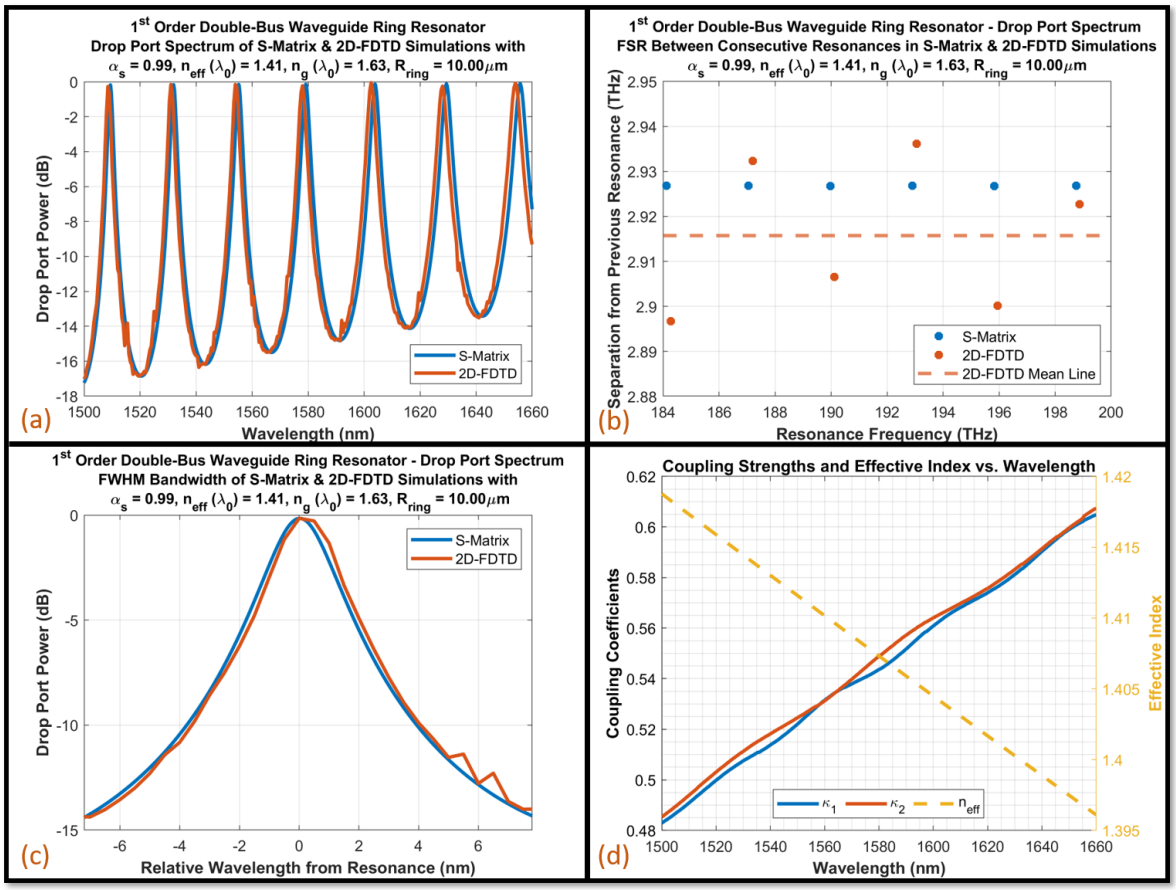

Figure 4.4: (a) Spectrum, (b) FSR and (c) FWHM comparison of the 1^{st} order double bus waveguide ring resonator drop port power between S-matrix and FDTD simulations, with (d) the wavelength dependent parameters

Therefore, the wavelength dependencies of the losses were not considered here, although introducing certain inaccuracy to the model. Nevertheless, it might act crucial for similar studies with lossy waveguides and care must be taken in such cases.

The extraction of the coupling coefficients and the effective index of the fundamental mode are done by 2D-FDTD simulations in RSoft (see Figure 4.4d) and the wavelength dependent values between 1500 nm and 1660 nm are integrated into the S-matrix model. The introduction of dispersion into the S-matrix resulted in a significant correspondence of drop port spectrum with FDTD simulations as shown in Figure 4.4a. The wavelength resolution of the FDTD simulations were 0.50 nm (≈60 GHz) and the spatial resolution of 30 ppw are chosen, which are found to provide an appropriate balance between accuracy and simulation complexity. In both simulations, the frequency separation value from the previous peak for each resonance are plotted in Figure 4.4b, where constant separation is found between the analytical S-matrix resonances. The mean value of the 2D-FDTD resonance separations is calculated and plotted as a constant line together with the individual separations calculated at each peak. The deviation from the mean line is found to be within the 60 GHz wavelength resolution of the

FDTD simulation, confirming the compliance of the results of the two models with each other, despite the FSR difference of around 10 GHz between the 2D-FDTD line and the S-matrix resonances (see Figure 4.4b). The reason behind calculating the resonance frequency separations in frequency domain, rather than as a function of wavelength as in the case of the spectrum from Figure 4.4a, is to have the constant separations of the S-matrix resonances as reference for interpreting the FDTD resonance separations. Moreover, the FWHMs are also found to be consistent in both cases, where an example comparison is plotted in Figure 4.4c, which is focused at the resonance peak near 1555 nm.

The slight mismatches between the two models can be explained by the FDTD resolution limitations and the main assumptions of S-matrix analysis. The spatial resolution limit affects the exact positions of the resonance frequencies, which might introduce certain shifts in comparison to the actual spectrum. Furthermore, the calculated FSR of different resonances is possibly affected by this limitation, another cause of which can be linked to the wavelength resolution limit. The simulated spectral span is also relatively wide, which might result in dispersion related imprecisions, stemming from the slight effective index inaccuracies. The fundamental assumptions of the S-matrix model, such as having wavelength independency of the losses ($\alpha(\lambda) = \alpha$), as well as assuming no coupling losses ($|\kappa|^2 + |t|^2 = 1$) can be put forward to explain the remaining mismatches of the two simulations.

Increasing the resolution of the simulations would therefore allow for more precise spectral representations of the physical geometry, as well as diminishing the differences of the S-matrix with the FDTD simulations. Nevertheless, the relatively simple S-matrix model already proves to be performing quite well, which can be used for larger geometries that cannot be easily simulated with FDTD. That being said, a promising framework for overcoming the issue of InP ring resonator simulations is proposed with this analysis on a relatively simple ring geometry. This allowed for continuing the physical simulations of the actual geometry. As it was done for the previous ring example, the first step is the effective index and coupling coefficient simulations in FDTD. For that, the investigation of the waveguides in InP was required.

The main waveguide structure in InP material platform is the rib/ridge type of configuration [7], where a slab layer of cladding material (InGaAsP) is laid between the substrate (InP) and the core material (InP). Afterwards, the structure is etched from the sides to leave a rectangular area for waveguiding at the top. Depending on the depth of the etching applied, the core can be fully confined to the rectangular region (deep etch) or be partially etched, where it consists of an underneath slab and a rectangular upper section (medium/shallow etch). There are mainly two waveguide geometries considered for this work that are available for fabrication, one of which is deep etched and the other is medium etched waveguides. The illustration given in Figure 4.5 depicts these geometries, where non-zero sidewall angle is assumed due to possible fabrication limitations. Thanks to the better field confinement offered by the deep etching, lower losses are present in this option, where down to 150 μm bending radii are fabricable. On the other hand, fields are guided in the medium etched waveguide with certain leakage from the sides of the slab region underneath. An example mode profile of the medium etched waveguide in Figure 4.5c shows this reduced mode confinement in comparison with the deep etched waveguide in Figure 4.5b. As a result of the increased losses with this structure, the minimum achievable bending radius value is 450 μm. This directly indicates at least three-fold decrease in the bandwidth of the ring resonator compared to the first option, when medium etched waveguides would

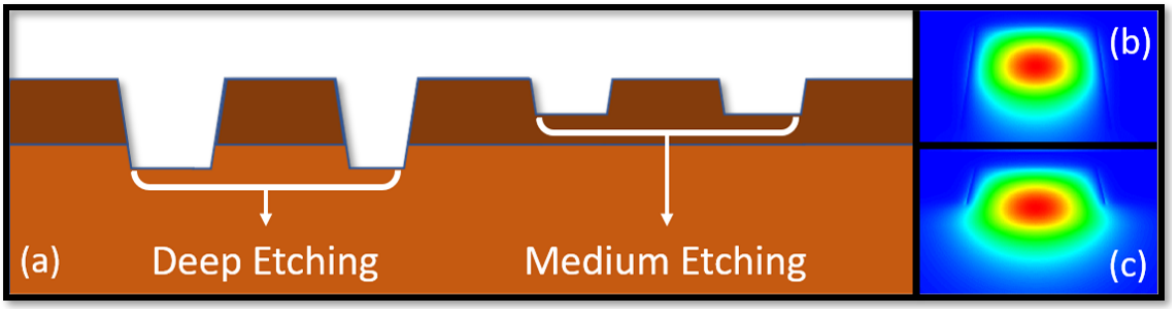

Figure 4.5: (a) Two waveguide structures considered in this work, as well as the corresponding fundamental mode comparison between (b) deep etched and (c) medium etched waveguides

be utilized for the filter design. Despite the higher losses and higher minimum bending radii of the medium etched waveguides, it is expected that higher coupling values could be achieved compared to deep etched waveguides, due to lower field confinement. With this consideration, the effective index and coupling strength simulations for both waveguide geometries are conducted using Beam Propagation Method (BPM) in RSoft. The waveguide width and height are determined to be 2 μm and 1 μm, respectively, which supports single mode for deep and medium etching.

Initially, the fundamental modes of the waveguides are calculated, together with the wavelength dependency of their effective indices and plotted in Figure 19a. For higher wavelengths, the ratio of the waveguide width to the wavelength decreases, which can be seen to reduce the effective index value and brings the waveguide away from being multimodal. Additionally, the normal dispersion (lower indices at longer wavelengths) and the fact of having the values between the core and the cladding indices are compatible results with the physical expectations.

Continuing with the directional coupling simulations, two straight waveguides are placed parallel in the simulation domains for both etching of the waveguides. The chosen gap between the waveguides, $d_{coupling} = 1.5\,\mu m$, is the minimum possible gap value determined by the fabrication limitation. The deep etched waveguide is found to half couple ($\kappa \approx 0.71$) to the parallel waveguide after approximately 171.5 mm at 1550 nm wavelength (see Figure 4.5b). With a ring geometry having a few hundred pm bandwidth requirement, the circumference of the ring cannot exceed a few hundred mm's, as can be inferred from the analysis made in the previous chapter. Because of this necessity, several-hundred-mm-long coupling sections with deep etched waveguides are not possible to realize with the ring resonators studied in this work. That is despite the fact that the deep etching offers the advantage of attaining relatively low bending radii ($R_{min} = 150\,\mu m$), as well as being superior to the medium etched waveguide with regard to the theoretically achievable lower bandwidth values. The simulations with the medium etched waveguide, on the other hand, has shown to reduce the required half-coupling length to approximately 1.534 mm, which is a significant improvement (see Figure 4.5b). Yet, this value is still not sufficiently low for ring resonators. Furthermore, the coupling simulations given here are carried out using straight directional waveguides. Without transforming the filter geometry to racetrack resonator, it is not possible to have straight coupling sections and the resulting coupling strengths would have even lower values with ring resonator due to the curved nature of the ring

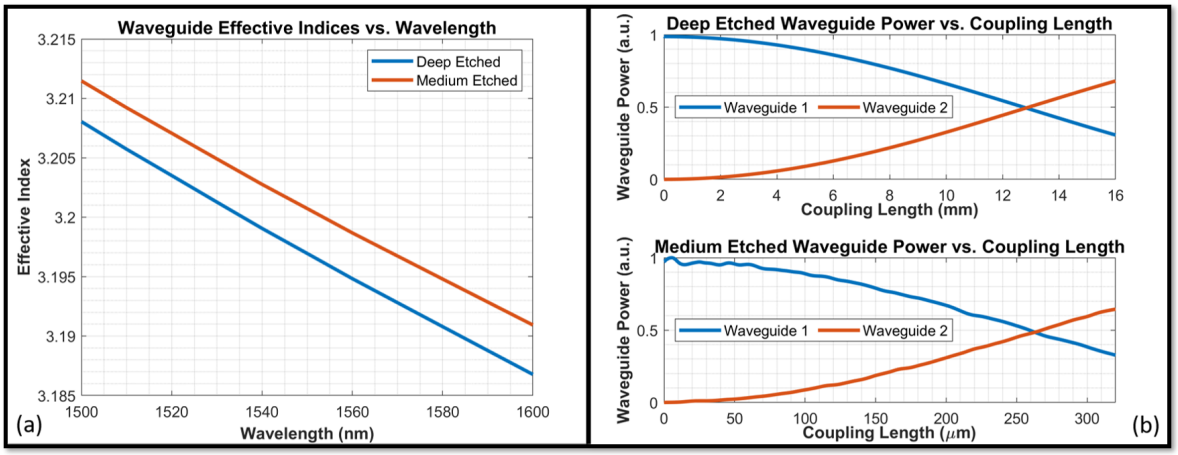

Figure 4.6: (a) Effective index and (b) coupling simulations for deep etched and medium etched InP waveguides. Coupling simulations are carried out at 1550 nm wavelength with 1.5 μm coupling gap

waveguide in the coupling region.

Recalling the theoretical indications of the last chapter, the minimum achievable radius of 150 μm is a necessity in terms of meeting the bandwidth criteria of this work with InP ring resonators. Likewise, high coupling coefficients ($\kappa > 0.8$) need to be achieved to this end. Using directional coupling, the simulations have shown that satisfying both at the same time is not possible with the available waveguide geometries, where the deep etching can only enable the radius condition and the medium etching offers the chance of attaining increased coupling strengths, although proving to be still insufficient.

In addition, an interesting approach is also considered to enhance coupling strengths by integrating MMI couplers instead of directional couplers, which however would transform the geometry into a racetrack resonator with straight sections at the coupling regions. The result of this would be increased circumference of the resonator, which again further reduces FSR and FWHM. Furthermore, compared to the default waveguide sections, different effective indices and phase accumulations inside the MMI sections would add more complexity in the integration of MMI couplers into the existing S-matrix model with a fixed index and a wavevector along the entire geometry. Either the whole theoretical model needed to be revised and improved, which would increase the complexity of the analysis, or another framework for simplifying the MMI sections would be necessary. In any case, due to the projected lower bandwidth result of this geometry, the idea of using MMI's for coupling in ring resonators is not investigated in this study. Nevertheless, it remains to be said that the integration of MMI couplers in ring resonator filters is still a quite reasonable alternative option in general, when it is desired to have sufficiently large coupling values in relatively short propagation lengths.

Moreover, buried heterostructure waveguide designs are also demonstrated to increase coupling strengths, where the core sections of the waveguides are enclosed in the claddings from every direction in the transverse plane [51]. Replacing air between the waveguides by the cladding material (for example InP or a polymer), reduces field confinement in the waveguides and the slope of the evanescent field amplitude in the cladding with lower index contrast. As a result, significantly higher coupling strengths

with this waveguide configuration are achieved. This is another promising attempt in having small ring circumferences, together with sufficient coupling values. Nevertheless, lower field confinement would also indicate higher losses, which is one of the trade-offs that should be considered. This waveguide structure is also disregarded here mainly due to the unavailability of the respective fabrication options in the selected foundry. Still, the objective of mentioning this alternative in this work is to provide another perspective to the general picture, which might prove helpful for similar design projects.

The final consideration regarding the design on ring resonators is regarding the tunability of the filter. Although possible, it is found to be not quite convenient to apply thermo-optic tuning to the filter with the curved nature of the ring resonator. Here, the reason is also fabrication related, where the heaters available for use in this study consisted of straight sections, which does not fully comply with the bent waveguides of the geometry. Compared to MZI filter, the design process of which will be explained in the next section, ring resonator filter appears to be slightly disadvantageous in terms of the tunability, due to this reason.

4.2 Mach Zehnder Interferometer Filter Design Process

Similar to the procedure followed with the ring resonator filter design, a preliminary viability check on the MZI filter is done by an S-matrix analysis. Due to the limitations regarding the finesse of the 1^{st} order MZI filter, preventing a flexible arrangement of FSR and FWHM, 2^{nd} order filtering is also considered here. For more information on the 2^{nd} order geometry preference, the reader is referred to Appendix C.2.

At first, two example parameter set are determined and the resulting spectra of the analytical investigation with S-matrix are generated in Figure 4.7. All of the four coupling coefficients are set to yield 3-dB coupling ($\kappa_1 = \kappa_2 = \kappa_3 = \kappa_4 = \frac{1}{\sqrt{2}}$) which are chosen to result in the highest ER and lowest IL, as shown in the previous chapter. Moreover, the losses, as well as the effective index are assumed to have the same value as in the analysis made for Figure 3.6. The 1^{st} order filter spectra are also plotted with blue curves to provide reference to the outputs of the 2^{nd} order filter. For the sake of readability of the figures, only the cross channel at the 2^{nd} order filter and the bar channel of the 1^{st} order outputs are selected, which allow for a fair comparison between the spectra obtained at each stage. Moreover, particular resonances near 1550 nm are marked with green vertical dashed lines. According to the ITU dense WDM (DWDM) grid standard, the positions of the four nearest side channels are also depicted in black with 100 GHz (0.80 nm) separation in between [1]. The 1^{st} and the 2^{nd} stage arm length differences are chosen to have 1-to-2 ratio for both examples, which increases the finesse of the filter while retaining the relatively periodic spectral shape. The main difference between Figure 4.7a and Figure 4.7b can be seen in the arm length differences, which result in different FSR and FWHM for both filter orders.

With the cost of slightly increasing the IL, the FWHM of the 1^{st} order MZI filter with $L_1 - L_2 = 560\,\mu m$ can be matched to the desired value of 37.5 GHz with the introduction of the 2^{nd} stage with $L_4 - L_3 = 1120\,\mu m$ (see Figure 4.7a). Better suppression of the neighboring four channels at two sides is also achieved with the increase in the filter order. A similar scenario can be observed with the 1^{st} order MZI filter, having the arm length difference, $L_1 - L_2 = 700\,\mu m$ (see Figure 4.7b). However,

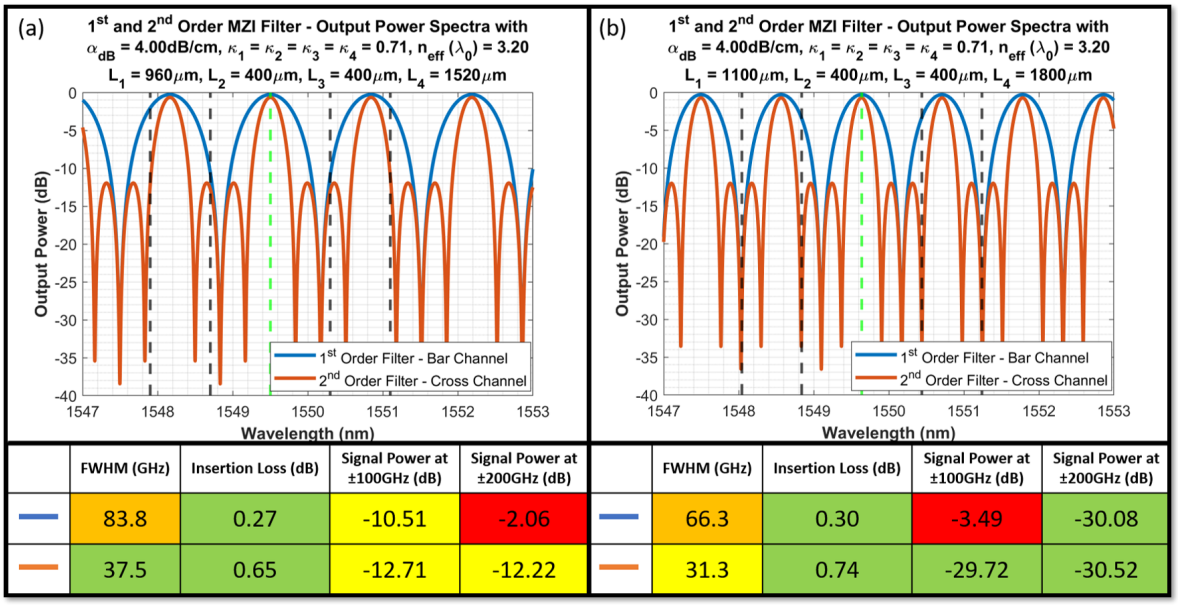

	FWHM (GHz)	Insertion Loss (dB)	Signal Power at ±100GHz (dB)	Signal Power at ±200GHz (dB)
—	83.8	0.27	-10.51	-2.06
—	37.5	0.65	-12.71	-12.22

	FWHM (GHz)	Insertion Loss (dB)	Signal Power at ±100GHz (dB)	Signal Power at ±200GHz (dB)
—	66.3	0.30	-3.49	-30.08
—	31.3	0.74	-29.72	-30.52

Figure 4.7: 1^{st} and 2^{nd} order MZI filter spectra comparison with (a) $560-1120\,\mu m$ (b) $700-1400\,\mu m$ arm length differences in the two stages of the filter, together with the resulting FWHM and IL of the resonances, as well as signal powers at the neighboring channels ($\pm 100\ GHz\ or\ \pm 0.80\,nm$)

in this case, the 2^{nd} order stage decreases the FWHM below the optimum value, while showing an immense improvement in the signal suppression for the side channels. Hence, through abstaining from having a perfect agreement with the bandwidth criteria, it is possible to align the positions of the side channels to correspond to the minima of the filter spectrum by the adjustment of the FSR. This is a quite promising finding in terms of the project goal, the idea of which is mentioned in Chapter 2.

The first step towards realizing the results of this preliminary investigation is taken by focusing on the coupling sections of the design. As demonstrated with the directional coupler simulations, the required length for half power coupling is practically not convenient for both waveguide etching schemes. Another option is to refer to MMI couplers, which become more favorable in achieving reduced coupling section lengths. Here, the attention of this study is not centered on the actual design of MMI couplers, since the existence of previously designed couplers for 50-50 power splitting ratio removed such a necessity. The indication of this was a significant gain on time and effort in the filter design process, which could be directed towards other important design activities. With the present MMI coupler model, 3-dB coupling could be achieved with sections shorter than 200 μm with the deep etched waveguide. The preference at this point is made towards the deep etching of the waveguide, in order to have smaller device dimensions with the lower bend radius it offers.

An interesting remark to be made at this point is that utilizing MMI couplers in MZI filters has a distinct physical implication in contrary to their use with ring resonator filters. The straight sections introduced with MMI couplers do not affect bandwidth and FSR of MZI filters, which are essentially defined by the phase accumulation differences in the interferometer arms. Since the phase change in the coupling sections of ring resonators are still included in the full-round trip of the field, effective

Table 4.1: Low and high frequency band channels considered for the design, that are compatible with the definitions of the ITU [1]

	Low Frequency Band	**High Frequency Band**
Channel 1	192.6 THz (1556.555 nm)	194.9 THz (1538.186 nm)
Channel 2	192.5 THz (1557.363 nm)	194.8 THz (1538.976 nm)
Channel 3	192.4 THz (1558.173 nm)	194.7 THz (1539.766 nm)
Channel 4	192.3 THz (1558.983 nm)	194.6 THz (1540.557 nm)

index and length of the coupling regions become important in ring resonator filter analysis. Other than determining coupling ratio and introducing 90° phase difference between output channels, MMI sections in MZI filter have no impact on output spectra. Hence, together with the relatively short coupling length requirements, 2x2 MMI couplers are preferred in this work for achieving half power splitting to attain the spectral response foreseen in Figure 4.7.

Having decided on the coupling section model, the other crucial parameter for the filter response, namely the wavelength dependent effective index is obtained with BPM waveguide simulations. Implementing the same methodology, the effective index model is created for two different frequency bands below and above the central design wavelength, 1550 nm. Due to the bi-directional communication planned to take place between satellites and ground stations that require two separate set of frequency channels (see Table 4.1), different wavelength intervals are considered. 4 communication channels are assumed for a single direction of data transfer, where the 2^{nd} channels are chosen to be the central reference channels. At first, the filter design is mainly planned for the channel 2 of each frequency band.

By introducing an example modulated signal spectrum, the maxima of which are aligned with the above defined channel frequencies, an overlap study is carried out between the filter response and the side channel signal powers. While adhering to the 1-to-2 ratio between the two stages, overlap integral is calculated for different MZI arm length differences of the 1^{st} stage. By doing so, the overlap is sought to be minimized, in order to achieve the maximized suppression of the side channels. The respective results of this analysis are illustrated in Figure 4.8a for both frequency bands. An important remark to be made here is that a prerequisite is put forward on the arm length differences for plotting the side channel power suppression. In this regard, the 1^{st} stage difference values yielding non-optimal alignment between the central channel and a filter resonance are disregarded. In other words, the selected set of values for the horizontal axis perfectly aligns an on-resonance of the filter with the 2^{nd} channel of the respective frequency band, although the discontinuities of the curves are not observable with the sub-μm separations between consecutive axis values. Moreover, for a reasonable range of filter bandwidth values aligned with the criteria of this study, the lower and upper limits of the 1^{st} stage arm length differences to be swept in this investigation are determined as 400 μm and 800 μm.

The minimum overlap value for the low frequency band is achieved with 628 μm length difference between the two interferometer arms of the 1^{st} stage and 1256 μm of the 2^{nd}. The resulting filter response is shown in Figure 4.8b, together with the example signal spectrum. On the figure, the

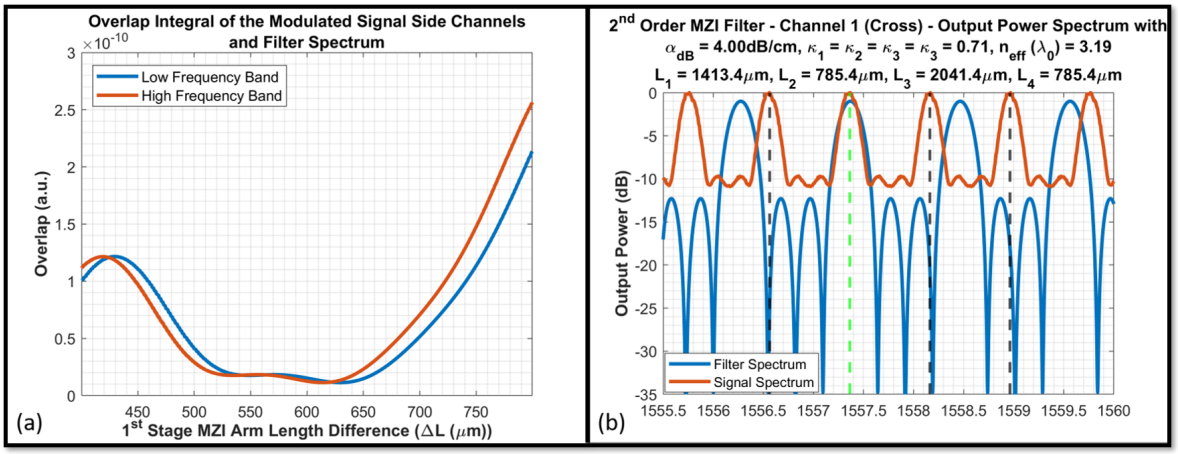

Figure 4.8: Side channel overlap study between filter and modulated signal spectrum with different 1^{st} stage MZI arm length differences and (b) the resulting filter spectrum at the overlap minimum for the low frequency band

wavelength of the central channel is marked with green dashed line, whereas the other 3 channel wavelengths are depicted with black dashed lines. Upon an initial observation, the spectral positionings of the side channels are found to be similar to the initial investigation made in the beginning of this section. The slightly broadened filter spectrum aligns the centers of the side channels not exactly to the dips in the filter response but applies a certain shift towards the central channel, the reason of which can be linked to the overall power overlap minimization. Noting that the obtained findings of Figure 4.8 are still the outcomes of the analytical study, the analysis of the filter spectrum results is left to the next chapter. A more detailed discussion is provided there with a verification study. As the study on ring resonators demonstrated, the robustness of the analytical approach has already been partially proven (see Figure 4.4). Though, supporting the investigation with physical simulations is deemed to be preferable. In this sense, the validity of the final design is verified by referring to numerical calculation methods using the commercial simulation software, RSoft.

The initial consideration is given to simulate the analytically designed structure by using FDTD method. Different from ring resonator filter, where steady state is reached after numerous cycles, converged MZI filter response can be obtained with a single pass of the field through the device. The reason behind this fundamental difference is related to the feedback and the feed-forward mechanisms of ring resonator and MZI geometries, where the details of this contrasting physics are elucidated in Appendix B.2. As a result, FDTD simulations for MZI filter can in principle be completed in relatively shorter computational times in comparison with ring resonator simulations. On the other hand, MZI filters are not as compact as ring resonators mentioned in Chapter 2. This, in turn, would increase the requirements on the simulation area and thus the computational burden. With this consideration, complete 3D-device simulations with FDTD method are still estimated to be fairly complicated. Another alternative, namely BPM, is also at first deemed to be a non-optimal choice for the MZI geometry that comprises bends in the interferometer arms, since BPM is inherently a directional field solving technique. In spite of this limitation, by applying certain transformations on

straight waveguides, it is, in fact, possible to simulate bends with BPM. The "simulated bend" feature of the software used in this work, RSoft, has been utilized for this purpose and the individual bends in the system could be simulated. Another restraint at this point is found to be regarding the difficulty of simultaneous simulation of interferometer arm pairs, due to the necessity of spatially matching the start and end vertices of the different length arms. To overcome this, the simulations with BPM are carried out by splitting the geometry and conducting consecutive simulations on separate parts of the filter. The electric field phase and the respective power values at the end of each defined simulation region is collected and are afterwards combined to yield the spectra at the output channels. In the next chapter, the obtained simulation findings regarding the filter response with this proposed methodology are gathered for the final analysis, where a comparison is made with respect to the estimations of the analytical model given in this chapter.

Chapter 5

Results and Discussion

The MZI filter to be simulated is initially designed as a whole, before carrying out individual segment simulations. Since the structure configurations, such as arm positionings, necessary bend placements of the arms and other related considerations would define the final model of the device, alternative options are investigated. Regarding the bend radius that would be preferred in the design, the decision is made towards 250 μm. The lower bending radius limit of 150 μm was not a necessity in the case of MZI filter, since the bandwidth related performance metrics are not directly linked to the bending radius as in ring resonator filter. Therefore, while aiming for a relatively small device size, the motivation is given to have reduced waveguide losses around the bends of the design. That is why, 250 μm bend radius is found to provide the right balance in this regard. Furthermore, the two stages of the filter are positioned "back-to-back" with respect to each other, rather than the common directional cascading modeled in Appendix C.2 (see Figure 5.1). The motivation behind this choice was to save as much space in the device area as possible and the resulting footprint is estimated to be approximately 1.76 mm^2 with 0.77x2.29 mm dimensions. The final device schematic is depicted in Figure 5.1, where the shorter arms of each stage consists of only two 90° bends.

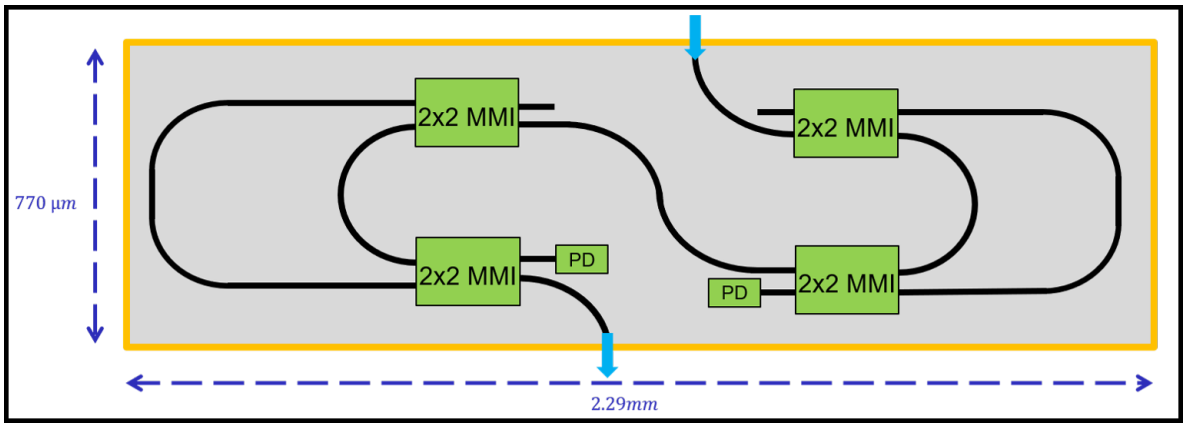

Figure 5.1: MZI filter final design schematic (not to scale)

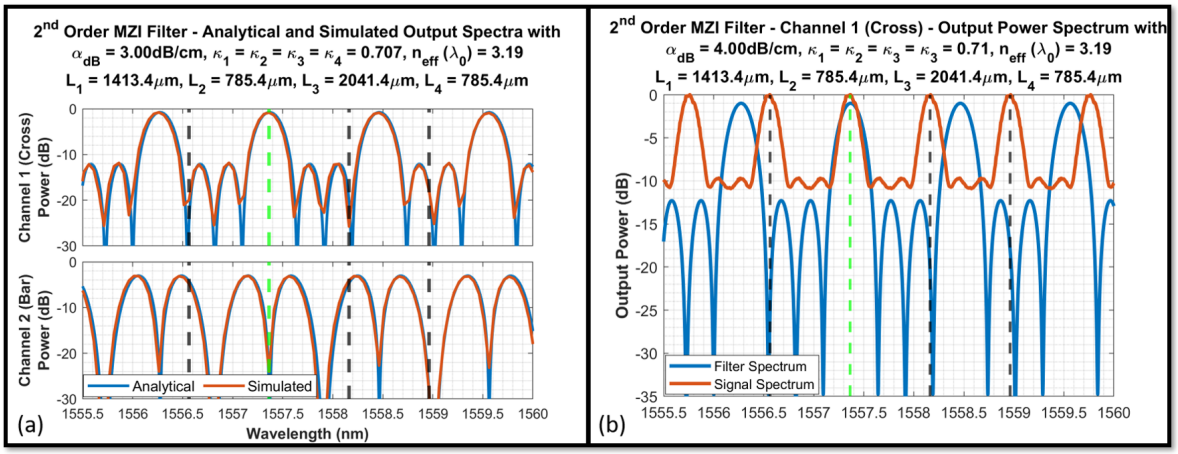

Figure 5.2: (a) Analytical and simulated spectra of the 2^{nd} order MZI filter and (b) the analytical filter response with modulated signal spectrum, showing the relative positioning of filter resonances and signal channels

Having decided on the dimensions of the device, the design process is followed with the BPM simulations of individual segments using 20 nm transversal and 100 nm longitudinal grids. In Figure 5.2a, the comparison between the cross and bar ports of the analytical filter response and the simulated spectra is demonstrated. The resemblance of the theoretical expectation and simulation plots verifies the viability of the ultimate design of the filter. It is worth noting that the propagation loss value of 3 dB/cm for the theory curve is not a systematically calculated value, rather it is determined to yield the maximum similarity with the simulation results. That being said, it is an estimation that comprises the propagation losses, bending losses and the losses at the MMI couplers. All the contributions from different loss sources are, therefore, expressed as a single term, due to the single loss parameter model of the analytical formalism. Moreover, since the wavelength dependency of the coupling coefficients of MMI couplers is found to be negligible in the wavelength span of the simulations, they are taken to be constant with $\kappa_1 = \kappa_2 = \kappa_3 = \kappa_4 = \frac{1}{\sqrt{2}}$ in the analytical results. These assumptions would provide an explanation to the slight discrepancies between the two plots.

As Figure 5.2a indicates, all of the KPI's determined in Chapter 2 have been met, some of which even succeed in satisfying the most ideal case. IL of 0.81 dB, 18-25 dB power suppression at the centers of the side channels and down to 25 dB maximum ER in the spectrum are the clearest verifications of this statement. Increasing the spectral resolution of the simulations should allow for the demonstration of even higher signal suppression values. With 31.25 GHz (0.25 nm) FWHM, the bandwidth requirement also appears to be matched to a certain extent, although the most optimum value of 37.5GHz (0.30 nm) is abandoned for the sake of achieving higher side channel power suppression. The main disadvantage of the current design can be associated with the non-flat signal suppression that show frequent and abrupt changes over the course of an FSR in the spectrum. For this reason, the edges of the nearest two side channels in the modulated signal spectrum experience relatively low-suppression due to their partial overlap with a filter resonance (see Figure 5.2b). This is not necessarily a significant problem, since the majority of the side channel power under the central region is suppressed, which was the

intended goal of the overlap study in the previous chapter. On the other hand, flat-top spectral response on the resonances in Figure 5.2 cannot be observed, which is ideally favorable in band-pass filter designs. One of the reasons for this can be attributed to the MZI geometry with single waveguide connection between the two stages. The direct transfer function multiplication of each stages with this design configuration prevents the flattening of the resonances, which is seen in the commonly used lattice MZI filter [41] geometry. At this point, refraining from using the prevalent geometry allows for increased signal suppression outside the resonances, being the main reason behind this design choice.

The FSR of the 2^{nd} order MZI filter is measured to be approximately 1.10 nm (137.5 GHz), which is slightly above the channel spacing value of 0.80 nm (37.5 GHz). From the tuning perspective, having FSR to be slightly larger than the channel spacing can actually be perceived as a benefit. To understand this clearly, Figure 5.3a can be inspected, which is the linear scale counterpart of the filter response from Figure 5.2b. Focusing here on thermal tuning and assuming temperature increase to reduce the effective index, heating the longer arms of the MZI filter causes the filter spectrum to shift to the shorter wavelengths, i.e. to the left in Figure 5.2b. This means that channel 3 can be tuned to the next filter resonance by applying a spectral shift that is equal to the difference between the FSR and a channel spacing value, which in this case is around 0.30 nm (37.5 GHz). Further increasing the temperature on the longer arms would tune channel 4 with 0.60 nm (75 GHz) and channel 1 with 0.80 nm (100 GHz) shift. The required tuning for every side channel is, therefore, actually below the FSR of the filter spectrum and at most equal to a single channel spacing value. For an FSR-free filter response, tuning to each side channel would require the amount of shift that is equal to the difference between the respective channel wavelength and the central channel wavelength. Assuming also that the heating is applied only to the longer MZI arms (for the device size considerations), the design needs to be made for channel 4, which becomes the new central channel. The reason for this is simply the left spectral shift happening with longer arm heating. In such a case, tuning to channel 1 would therefore necessitate a 2.40 nm shift, which indicates approximately 4.36π extra phase addition on the longer 1^{st} stage arm due to heating (and 8.72π for the longer 2^{nd} stage arm, to retain the 1-to-2 stage ratio). As opposed to that, the current design with limited and close-to-channel-spacing-FSR can be tuned for every side channel with at most 1.455π phase shift on the longer arm of the 1^{st} stage. Increasing the number of channels, however, might prove problematic in this case, since 1.10 nm FSR places every 4^{th} channel approximately to the same spectral positions with respect to the filter resonances. This can be visually verified from the 1^{st} and the 4^{th} filter resonances in Figure 5.3a, which are separated from their left neighboring channels by similar spectral shifts.

The device dimensions mentioned up to this point were determined for the low frequency band (1556-1559 nm) channels. Keeping the same design, a filter resonance for the higher frequency band (1538-1541 nm) also aligns with the respective central channel at 1538.976 nm (194.8 THz) almost in perfect agreement. In that case, at most 0.03 nm tuning is necessary for a perfect alignment, which is comparatively low with respect to the 1.10 nm of FSR. This is a significant advantage of the designed filter, indicating the availability of its use for both frequency bands. Therefore, with relatively small required tuning, a single design can function for both communication directions between ground stations and satellites. For other MZI filter design projects, certain arm length differences can be found that results in similar spectral resemblances between different wavelength ranges, allowing

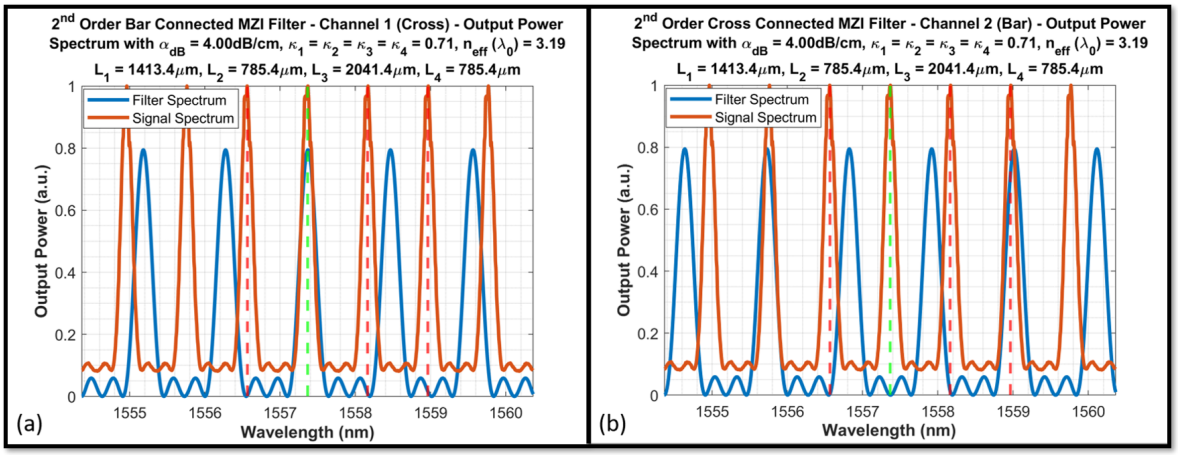

Figure 5.3: (a) Bar connected 2^{nd} order MZI filter channel 1 (cross) output and (b) cross-connected 2^{nd} order MZI filter channel 2 (bar) output response with modulated signal spectra

the production of universal filters for various communication bands. The values determined for this project are one among the many, that also happens to maximize the power suppression for the side communication channels.

An alternative tuning option to only heating the longer MZI arms can be proposed with also heating the shorter arms of the MZI stages. The filter spectrum in that case would be shifted to the higher wavelengths, i.e. to the right in Figure 5.3a. This can be beneficial for tuning of channel 1, which is the channel requiring the maximum shift when heating is applied to the longer arms. Changing the direction of the spectral shift would reduce the necessary phase change from 1.455π to 0.546π, resulting in 62.5% power reduction for channel 1. This would, however, be possible if the length of the interferometer arms could be increased, including the addition of straight sections to the shorter arms. Leading to size expansion of the device, this solution might not always be favorable, depending on the design choices.

In order to decrease the tuning power for certain channels, it is also worth considering the use of another filter geometry. The spectrum in Figure 5.3a is obtained from the cross-channel output of the "bar-connected" 2^{nd} order MZI filter (see Figure C.3). Here, the term "bar-connected" refer to connecting the 1^{st} and the 2^{nd} stages via the bar ports and leaving the cross-port connection open. Using the same device dimensions (e.g. arm lengths, bending radii), the bar-channel of the "cross-connected" 2^{nd} order MZI filter would, in turn, result in the spectrum seen in Figure 5.3b. Maintaining the exact spectral response, a π-shift can be achieved only by reverting the position of the connection waveguide for a specific channel design and measuring the power from the opposite output port. Hence, by exploiting an inherent nature of the MZI geometry, the tuning of channel 1 and 4 can be done by significant reduction in the additional phase shift requirements (see Figure 5.3b). The disadvantage of this approach would be, however, losing the universality of the design that should be suitable for every channel circuit in the system and can be inconvenient from the system design perspective.

Chapter 6

Conclusions and Further Recommendations

This thesis focused on the design process of integrated optical filter for a transceiver system in InP. The literature study demonstrated the advantages and disadvantages of various material platforms and filter types available for the realization of the target device. With the developed theoretical background on the filtering with add-drop ring resonators and MZI's, in depth analysis is provided that sheds light in the different physics and characteristics of both geometries. Especially for the simulation of large optical filters, which could be relevant for similar studies, a useful framework with S-matrix and FDTD simulations have been established. The computational burden is shown to be reduced significantly, through preliminary dispersive modelling of effective index and coupling coefficients in ring resonator filters. Moreover, the same procedure can be easily applicable for MZI filters.

During the course of the project, ring resonator filters in InP material platform are found to be unsuitable for the implementation of the initial sub-nm bandwidth criteria. The difficulty of achieving both relatively high coupling coefficients and keeping the ring circumference short at the same time impeded the continuation of the filter design with ring resonators and the focus is directed towards the other alternative geometry, namely MZI filter. Although it is left unexamined in this study, racetrack resonator filter with MMI couplers is shown to be another potential filtering device in InP for studies with more relaxed bandwidth requirements. In that case, the theory laid out in this thesis needs to be expanded, in order to include the different effective indices of MMI couplers and resonator waveguides in the modelling. Since both coupling and waveguiding sections would contribute to the exact phase accumulation after every round trip of the resonator, the current model with single effective index representation would be insufficient in that case.

Regarding the MZI filter order and geometry, certain considerations have been made in view of the existing trade-offs. First of all, to improve the spectral performance, filter order is increased to 2 with single port connection between the two stages. With the single-port connected 2^{nd} order geometry, flat-top response is sacrificed in order to increase the side channel signal suppression and decrease the bandwidth of the filter. Further increasing the filter order is disregarded for the sake of keeping the device dimensions as small as possible, since the 2^{nd} order filter area is already assessed to be relatively large. If the area limitations are more flexible, increasing the filter order might be a reasonable choice

that should further increase noise suppression. Nevertheless, the device complexity would also increase, making the design process lengthier and more complicated than with a lower-order filter.

Concerning the coupling sections of the current design, 2x2 MMI couplers are preferred to achieve the 3-dB power splitting between the waveguiding sections. As opposed to the wavelength-dependent nature of directional couplers, MMI couplers allowed for relatively stable splitting ratios over the entire investigated wavelength spectrum. Furthermore, MMI couplers also proved to be quite useful in minimizing the size of the device by reducing the required coupling lengths. Another option, which is not considered in this work, can offer further shortening of the device length, when device size considerations are crucially important. This can be done by replacing the 2x2 MMI couplers at the inputs of each filter stage with 1x2 MMI couplers. Since 3-dB coupling in 2x2 MMI couplers requires longer lengths than 1x2 MMI couplers, this can be a slightly advantageous choice in terms of device size. However, in this case, using the identical device dimensions would not yield the same spectrum at the output, which is affected by the different geometry of the 1x2 MMI couplers. The coupling equations given in this work are determined with respect to the physics of directional couplers and are compatible with 2x2 MMI couplers. However, these equations are slightly changed for 1x2 MMI couplers, due to the different positions of the input waveguides. For 50-50 power splitting geometry, the phases of the electric fields at the output ports of a 1x2 MMI coupler adopt the same values, owing to the symmetry of the device. On the contrary, directional couplers and 2x2 MMI couplers result in 90° phase difference between the two output channels. This fundamental dissimilarity needs to be considered when designing the MZI filter with different coupler geometries. The theoretical derivations of this study can be applied to cover such a hybrid design with 1x2 and 2x2 MMI's. In this case, the arm length differences of the design determined for the model with only 2x2 MMI couplers should be slightly changed, if the goal is to attain the same spectral response at the output.

The final remark to be made about the designed filter is that the exact phase accumulation in the MZI arms are fairly dependent on the true effective index of the waveguides. Consequently, it can be predicted that the material model used in the simulations would not exactly match the fabricated material properties. In the light of possible fabrication inaccuracies, the simulation estimations for the exact resonance wavelengths and signal suppression values for the side channels are likely to be different from the hardware results. The resulting IL, FSR and FWHM are not expected to deviate significantly, yet the filter resonances and relative channel positionings might become crucial in the fabricated device. Although it is difficult to prevent such simulation-fabrication mismatches, tuning can be used to minimize the resulting spectral discrepancies. For that reason, and the fact that the same design can be used for multiple wavelength channels, tuning is highly recommended for similar MZI filter design projects.

References

[1] *Spectral Grids for WDM applications: DWDM frequency grid*, The International Telecommunication Union", 2020.

[2] W. S. Zaoui, A. Kunze, W. Vogel, M. Berroth, J. Butschke, F. Letzkus, and J. Burghartz, "Bridging the Gap Between Optical Fibers and Silicon Photonic Integrated Circuits," *Optics Express*, vol. 22, no. 2, p. 1277, 2014.

[3] S. J. Yoo, B. Guan, and R. P. Scott, "Heterogeneous 2D/3D Photonic Integrated Microsystems," *Microsystems & Nanoengineering*, vol. 2, no. 1, 2016.

[4] T. Sharma, J. Wang, B. K. Kaushik, Z. Cheng, R. Kumar, Z. Wei, and X. Li, "Review of Recent Progress on Silicon Nitride-Based Photonic Integrated Circuits," *IEEE Access*, vol. 8, pp. 195 436–195 446, 2020.

[5] M. Smit, K. Williams, and J. van der Tol, "Past, Present, and Future of InP-Based Photonic Integration," *APL Photonics*, vol. 4, no. 5, p. 050901, 2019.

[6] M. W. Ziarko, G. Terrasanta, and R. M. Calvo, "Optical Communications for Very High Throughput Satellites," in *Advanced Photonics Congress*, 2021.

[7] J. Klamkin, H. Zhao, B. Song, Y. Liu, B. Isaac, S. Pinna, F. Sang, and L. Coldren, "Indium Phosphide Photonic Integrated Circuits: Technology and Applications," in *IEEE BiCMOS and Compound Semiconductor Integrated Circuits and Technology Symposium (BCICTS)*, San Diego, California, USA, 2018.

[8] T. Mizuno and Y. Miyamoto, "High-Capacity Dense Space Division Multiplexing Transmission," *Optical Fiber Technology*, vol. 35, pp. 108–117, 2017.

[9] R. M. Calvo, J. Poliak, J. Surof, A. Reeves, M. Richerzhagen, H. F. Kelemu, R. Barrios, C. Carrizo, R. Wolf, F. Rein, A. Dochhan, K. Saucke, and W. Luetke, "Optical Technologies for Very High Throughput Satellite Communications," in *Proc. of SPIE, Free-Space Laser Communications XXXI*, vol. 10910, 2019.

[10] P. R. Binetti, M. Lu, E. J. Norberg, R. S. Guzzon, J. S. Parker, A. Sivananthan, A. Bhardwaj, L. A. Johansson, M. J. Rodwell, and L. A. Coldren, "Indium Phosphide Photonic Integrated Circuits for Coherent Optical Links," *IEEE Journal of Quantum Electronics*, vol. 48, no. 2, pp. 279–291, 2012.

[11] A. A. Jørgensen, D. Kong, M. R. Henriksen, F. Klejs, Z. Ye, O. B. Helgason, H. E. Hansen, H. Hu, M. Yankov, S. Forchhammer, P. Andrekson, A. Larsson, M. Karlsson, J. Schröder, Y. Sasaki, K. Aikawa, J. W. Thomsen, T. Morioka, M. Galili, V. Torres-Company, and L. K. Oxenløwe, "Petabit-per-Second Data Transmission Using a Chip-Scale Microcomb Ring Resonator Source," *Nature Photonics*, vol. 16, no. 11, pp. 798–802, 2022.

[12] J. Tang, M. Li, and J. Yao, "A Center Frequency and Bandwidth Tunable Microwave Photonic Band-Stop Filter Based on an InP/InGaAsP Micro-Ring Resonator," in *International Topical Meeting on Microwave Photonics (MWP)*, Ottawa, Canada, 2019.

[13] D. Thomson, A. Zilkie, J. E. Bowers, T. Komljenovic, G. T. Reed, L. Vivien, D. Marris-Morini, E. Cassan, L. Virot, and J.-M. Fédéli, "Roadmap on Silicon Photonics," *Journal of Optics*, vol. 18, no. 7, p. 073003, 2016.

[14] D. J. Blumenthal, R. Heideman, D. Geuzobroek, A. Leinse, and C. Roeloffzen, "Silicon Nitride in Silicon Photonics," in *Proceedings of the IEEE*, vol. 106, no. 12, 2018, pp. 2209–2231.

[15] H. H. Li, "Refractive Index of Silicon and Germanium and its Wavelength and Temperature Derivatives," *Journal of Physical and Chemical Reference Data*, vol. 9, no. 3, pp. 561–658, 1980.

[16] I. H. Malitson, "Interspecimen Comparison of the Refractive Index of Fused Silica*,†," *Journal of the Optical Society of America*, vol. 55, no. 10, p. 1205, 1965.

[17] R. Baets, A. Z. Subramanian, S. Clemmen, B. Kuyken, P. Bientsman, N. L. Thomas, G. Roelkens, D. V. Thourhout, P. Helin, and S. Severi, "Silicon Photonics: Silicon Nitride versus Silicon-on-Insulator," in *Optical Fiber Communication Conference*, Anaheim, California, USA, 2016.

[18] S. Bogdanov, M. Y. Shalaginov, A. Boltasseva, and V. M. Shalaev, "Material Platforms for Integrated Quantum Photonics," *Optical Materials Express*, vol. 7, no. 1, p. 111, 2016.

[19] S. Cui, K. Cao, Y. Yu, and X. Zhang, "Ultra-High-Q Racetrack Microring Based on Silicon-Nitride," October 2022.

[20] C. G. Roeloffzen, M. Hoekman, E. J. Klein, L. S. Wevers, R. B. Timens, D. Marchenko, D. Geskus, R. Dekker, A. Alippi, R. Grootians, A. van Rees, R. M. Oldenbeuving, J. P. Epping, R. G. Heideman, K. Worhoff, A. Leinse, D. Geuzebroek, E. Schreuder, P. W. van Dijk, I. Visscher, C. Taddei, Y. Fan, C. Taballione, Y. Liu, D. Marpaung, L. Zhuang, M. Benelajla, and K. J. Boller, "Low-Loss Si_3N_4 Triplex Optical Waveguides: Technology and Applications Overview," *IEEE Journal of Selected Topics in Quantum Electronics*, vol. 24, no. 4, pp. 1–21, 2018.

[21] Y. Marin, T. Nannipieri, C. J. Oton, and F. D. Pasquale, "Fiber Bragg Grating Sensor Interrogators on Chip: Challenges and Opportunities," in *25th Optical Fiber Sensors Conference (OFS)*, Jeju, South Korea, 2017.

[22] A. Kaźmierczak, L. Vivien, K. B. Gylfason, B. Sanchez, A. Griol, D. Marris-Morini, E. Cassan, F. Dortu, H. Sohlström, D. Giannone, and D. Hill, "High Quality Optical Microring Resonators in Si_3N_4/SiO_2," in *14th European Conference on Integrated Optics (ECIO)*, Eindhoven, Netherlands, 2008.

[23] D. J. Moss, R. Morandotti, A. L. Gaeta, and M. Lipson, "New CMOS-Compatible Platforms Based on Silicon Nitride and Hydex for Nonlinear Optics," *Nature Photonics*, vol. 7, no. 8, pp. 597–607, 2013.

[24] A. P. Ovvyan, N. Gruhler, S. Ferrari, and W. H. Pernice, "Cascaded Mach–Zehnder Interferometer Tunable Filters," *Journal of Optics*, vol. 18, no. 6, p. 064011, 2016.

[25] Z. Zhang, A. M. Novo, D. Liu, N. Keil, and N. Grote, "Compact and Tunable Silicon Nitride Bragg Grating Filters in Polymer," *Optics Communications*, vol. 321, pp. 23–27, 2014.

[26] I. Giuntoni, A. Gaida, M. Krause, R. Steingrüber, J. Bruns, and K. Petermann, "Tunable Bragg Reflectors on Silicon-on-Insulator Rib Waveguides," *Optics Express*, vol. 17, no. 21, p. 18518, 2009.

[27] F. G. D. Corte, G. Cocorullo, M. Jodice, and I. Rendina, "Temperature Dependence of the Thermo-Optic Coefficient of InP, GaAs, and SiC from Room Temperature to 600 K at the Wavelength of 1.5 μm," *Applied Physics Letters*, vol. 77, no. 11, pp. 1614–1616, 2000.

[28] S. Arafin and L. A. Coldren, "Advanced InP Photonic Integrated Circuits for Communication and Sensing," *IEEE Journal of Selected Topics in Quantum Electronics*, vol. 24, no. 1, pp. 1–12, 2018.

[29] G. D. Pettit and W. J. Turner, "Refractive Index of InP," *Journal of Applied Physics*, vol. 36, no. 6, p. 2081, 1965.

[30] B. Broberg and S. Lindgren, "Refractive Index of $In_{1-x}Ga_xAs_yP_{1-y}$ Layers and InP in the Transparent Wavelength Region," *Journal of Applied Physics*, vol. 55, no. 9, pp. 3376–3381, 1984.

[31] M. G. Saber, Z. Xing, D. Patel, E. El-Fiky, N. Abadia, Y. Wang, M. Jacques, M. Morsy-Osman, and D. V. Plant, "A CMOS Compatible Ultracompact Silicon Photonic Optical Add-Drop Multiplexer with Misaligned Sidewall Bragg Gratings," *IEEE Photonics Journal*, vol. 9, no. 3, pp. 1–10, 2014.

[32] S. Xie, J. Zhan, Y. Hu, Y. Zhang, S. Veilleux, J. Bland-Hawthorn, and M. Dagenais, "Add–Drop Filter with Complex Waveguide Bragg Grating and Multimode Interferometer Operating on Arbitrarily Spaced Channels," *Optics Letters*, vol. 43, no. 24, p. 6045, 2018.

[33] I. Teraoka, "A Hybrid Filter of Bragg Grating and Ring Resonator," *Optics Communications*, vol. 339, pp. 108–114, 2015.

[34] R. Cheng and L. Chrostowski, "Spectral Design of Silicon Integrated Bragg Gratings: A Tutorial," *Journal of Lightwave Technology*, vol. 39, no. 3, pp. 712–729, 2021.

[35] C. Sun, Y. Yin, Z. Chen, Y. Ye, Y. Luo, H. Ma, L. Wang, M. Wei, J. Jian, R. Tang, H. Dai, J. Wu, J. Li, D. Zhang, H. Lin, and L. Li, "Tunable Narrow-Band Single-Channel Add-Drop Integrated Optical Filter with Ultrawide FSR," *PhotoniX*, vol. 3, no. 12, 2022.

[36] H. Saghaei, P. Elyasi, and B. J. Shastri, "Sinusoidal and rectangular bragg grating filters: Design, fabrication, and comparative analysis," *Journal of Applied Physics*, vol. 132, no. 6, p. 064501, 2022.

[37] X. Wang, W. Shi, R. Vafaei, N. A. Jaeger, and L. Chrostowski, "Uniform and sampled bragg gratings in soi strip waveguides with sidewall corrugations," *IEEE Photonics Technology Letters*, vol. 23, no. 5, pp. 290–292, 2011.

[38] X. Wang, W. Shi, H. Yun, S. Grist, N. A. Jaeger, and L. Chrostowski, "Narrow-Band Waveguide Bragg Gratings on SOI Wafers with CMOS-Compatible Fabrication Process," *Optics Express*, vol. 20, no. 14, p. 15547, 2012.

[39] N. Kohli, B. Sang, F. Nabki, and M. Menard, "Tunable Bandpass Filter with Serially Coupled Ring Resonators Assisted MZI," *IEEE Photonics Journal*, vol. 13, no. 4, pp. 1–8, 2021.

[40] J. Wang, I. Glesk, and L. R. Chen, "Subwavelength Grating Bragg Grating Filters in Silicon-on-Insulator," *Electronics Letters*, vol. 51, no. 9, pp. 712–714, 2015.

[41] F. Horst, W. Green, S. Assefa, S. Shank, Y. Vlasov, and B. J. Offrein, "Cascaded Mach-Zehnder Wavelength Filters in Silicon Photonics for Low Loss and Flat Pass-Band WDM (de-)Multiplexing," *Optics Express*, vol. 21, no. 10, pp. 11 652–11 658, 2013.

[42] R. S. Guzzon, E. J. Norberg, J. S. Parker, L. A. Johansson, and L. A. Coldren, "Integrated InP-InGaAsP Tunable Coupled Ring Optical Bandpass Filters with Zero Insertion Loss," *Optics Express*, vol. 19, no. 8, p. 7816, 2011.

[43] M. Cherchi, M. Harjanne, S. Ylinen, M. Kapulainen, T. Vehmas, and T. Aalto, "Flat-Top MZI Filters: A Novel Robust Design Based on MMI Splitters," in *Proc. SPIE 9752, Silicon Photonics XI, San Francisco, California, USA*, 2016.

[44] "Performance Summary-Table," [Online]. Available: https://www.hhi.fraunhofer.de/en/departments/pc/research-groups/photonic-inp-foundry/our-offer/performance-summary-table.html, Fraunhofer Heinrich Hertz Institute, [Accessed 10 January 2023].

[45] A. Tauke-Pedretti, G. A. Vawter, E. J. Skogen, G. Peake, M. Overberg, C. Alford, D. Torres, and F. Cajas, "InP Tunable Ring Resonator Filters," in *Proc. SPIE 8628, Optoelectronic Integrated Circuits XV, San Francisco, California, USA*, 2013.

[46] D. H. Geuzobroek and A. Driessen, *Wavelength Filters in Fibre Optics*. Heidelberg, Germany: Springer Berlin, 2006, ch. 8 - Ring-resonator-based wavelength filters, pp. 341–379.

[47] W. Bogaerts, P. D. Heyn, T. V. Vaerenbergh, K. D. Vos, S. K. Selvaraja, T. Claes, P. Dumon, P. Bienstman, D. V. Thourhout, and R. Baets, "Silicon Microring Resonators," *Laser & Photonics Reviews*, vol. 6, no. 1, pp. 47–73, 2012.

[48] S. Feng, T. Lei, H. Chen, H. Cai, X. Luo, and A. W. Poon, "Silicon Photonics: From a Microresonator Perspective," *Laser & Photonics Reviews*, vol. 6, no. 2, pp. 145–177, 2012.

[49] A. Yariv, "Universal Relations for Coupling of Optical Power Between Microresonators and Dielectric Waveguides," *Electronics Letters*, vol. 36, no. 4, pp. 321–322, 2000.

[50] A. Belarouci, K. B. Hill, Y. Liu, Y. Xiong, T. Chang, and A. E. Craig, "Design and Modelling of Waveguide-Coupled Microring Resonator," *Journal of Luminescence*, vol. 94–95, pp. 35–38, 2001.

[51] S. J. Choi, K. Djordjev, Z. Peng, Q. Yang, S. J. Choi, and P. D. Dapkus, "Laterally Coupled Buried Heterostructure High-Q Ring Resonators," *IEEE Photonics Technology Letters*, vol. 16, no. 10, pp. 2266–2268, 2004.

[52] R. Grover, "Indium Phosphide Based Optical Micro-Ring Resonators," Ph.D. dissertation, University of Maryland, 2003.

[53] A. Yariv, "Coupled-Mode Theory for Guided-Wave Optics," *IEEE Journal of Quantum Electronics*, vol. 9, no. 9, pp. 919–933, 1973.

[54] E. J. Norberg, R. S. Guzzon, J. S. Parker, L. A. Johansson, and L. A. Coldren, "Programmable Photonic Microwave Filters Monolithically Integrated in InP–InGaAsP," *Journal of Lightwave Technology*, vol. 29, no. 11, pp. 1611–1619, 2011.

[55] R. Boeck, N. A. F. Jaeger, N. Rouger, and L. Chrostowski, "Series-Coupled Silicon Racetrack Resonators and the Vernier Effect: Theory and Measurement," *Optics Express*, vol. 18, no. 24, pp. 25 151–25 157, 2010.

[56] Q. Deng, L. Liu, R. Zhang, X. Li, J. Michel, and Z. Zhou, "Athermal and Flat-Topped Silicon Mach-Zehnder Filters," *Optics Express*, vol. 24, no. 26, pp. 29 577–29 582, 2016.

Appendix A

Determination of the S-Matrix Parameter Relations Through Coupled Mode Theory Analysis

As previously mentioned, several assumptions are made to find the relations between the individual elements of the S-matrix. These are namely the following: taking the losses during the coupling process to be zero, the excitation of only a single unidirectional mode of the resonator and assuming that no reflection takes place in the system. By referring to the coupled mode theory for the starting point, the relations between the off-diagonal elements of the matrix will be found. It is also worth mentioning that certain parts of the following derivations are adopted from the investigation in the PhD thesis of Dr. Rohit Grover [52].

Here, the coupling region between the input-pass waveguide and the ring resonator will be taken for the derivation, where the field through the input-pass waveguide is denoted with f and the field in the ring resonator is given by g (see Figure 3.1c):

$$f(z,x,t) = F(z)e^{i(\omega_a t - \beta_a z)}f(x) \tag{A.1}$$

$$g(z,x,t) = G(z)e^{i(\omega_b t - \beta_b z)}g(x) \tag{A.2}$$

In the definitions above, F and G are the complex amplitudes of the fields, which are functions of the longitudinal position along the coupling region. The following relations are provided for the sake of completeness, where the time and transversal field dependencies are omitted for reasons of brevity:

$$f(z,0) = a_1 \qquad f(z=L) = b_1 \tag{A.3}$$

$$g(z,0) = a_2 \qquad g(z=L) = b_2 \tag{A.4}$$

The coupled mode equations, relating the complex amplitudes of the fields are then written as [53]:

$$\frac{dF}{dz} = \kappa_{fg} G e^{-i\Delta z} \tag{A.5}$$

$$\frac{dG}{dz} = \kappa_{gf} F e^{i\Delta z} \tag{A.6}$$

where κ_{fg} and κ_{gf} are the coupling coefficients from the ring waveguide to the input waveguide and vice versa, respectively. Δz is the phase-mismatching constant, which is not of significant interest for the purpose of this derivation. In the co-directional coupling case, the conservation of total power along the longitudinal axis of the waveguides necessitates the following [53]:

$$\frac{d}{dz}(|F|^2 + |G|^2) = 0 \tag{A.7}$$

As the next step, this expression is rearranged and the coupled wave equations are plugged in:

$$\frac{d}{dz}(FF^* + GG^*) = F^* \frac{dF}{dz} + G\frac{dG^*}{dz} + cc. = 0 \tag{A.8}$$

$$F^* G e^{-i\Delta z}(\kappa_{fg} + \kappa_{gf}^*) + cc. = 0 \tag{A.9}$$

A non-trivial solution ($F \neq 0$, $G \neq 0$) for this equation is found when:

$$\kappa_{fg} = -\kappa_{gf}^* \tag{A.10}$$

Since the coupling coefficients κ_{fg} and κ_{gf} represent the field transfer to an opposite waveguide, their relation allows to relate the off-diagonal axis elements in the S-matrix that is defined previously:

$$s_{12} = -s_{21}^* \tag{A.11}$$

Having acquired the first condition on the matrix elements, another derivation can be done by assuming that no energy is lost during the coupling process due to the field interactions [52]:

$$|b_1|^2 + |b_2|^2 = |a_1|^2 + |a_2|^2 \tag{A.12}$$

This can be written in the compact matrix form and solved via matrix operations, where the initial expression $b = Sa$ is made use of:

$$b^\dagger b = a^\dagger a$$

$$b^\dagger b = (Sa)^\dagger Sa = a^\dagger S^\dagger Sa = a^\dagger a \tag{A.13}$$

From the upper line, a useful relation is acquired:

$$S^\dagger S = 1 \tag{A.14}$$

which is then unwrapped to obtain further relations between the matrix terms:

$$S^\dagger S = \begin{pmatrix} s_{11}^* & s_{21}^* \\ s_{12}^* & s_{22}^* \end{pmatrix} \begin{pmatrix} s_{11} & s_{12} \\ s_{21} & s_{22} \end{pmatrix} = \begin{pmatrix} |s_{11}|^2 + |s_{21}|^2 & s_{12}s_{11}^* + s_{22}s_{21}^* \\ s_{11}s_{12}^* + s_{21}s_{22}^* & |s_{12}|^2 + |s_{22}|^2 \end{pmatrix} = \begin{pmatrix} 1 & 0 \\ 0 & 1 \end{pmatrix} \tag{A.15}$$

$$|s_{11}|^2 + |s_{21}|^2 = 1 \tag{A.16}$$

$$|s_{12}|^2 + |s_{22}|^2 = 1 \tag{A.17}$$

$$s_{12}s_{11}^* = -s_{22}s_{21}^* \tag{A.18}$$

At this point, a switch from the S-parameters to the coupling parameters is done, with the introduction of κ and t terms, representing the coupling strength from the input to the opposite waveguide and transmission along the input-pass waveguide, respectively.

$$S = \begin{pmatrix} s_{11} & s_{12} \\ s_{21} & s_{22} \end{pmatrix} = \begin{pmatrix} t & s_{12} \\ \kappa & s_{22} \end{pmatrix} \tag{A.19}$$

Using the off-diagonal element relation (Eq. A.11) and the condition arising from the lossless coupling (Eq. A.18), s_{12} and s_{22} are plugged in, which completes the matrix [49]:

$$s_{22} = -\frac{s_{12}t^*}{\kappa^*} = t^* \tag{A.20}$$

$$S = \begin{pmatrix} t & -\kappa^* \\ \kappa & t^* \end{pmatrix} \tag{A.21}$$

As a final check, Eq. A.16 and Eq. A.17 are inspected, which serve to support the validity of the obtained result by stating the matrix to be unitarity:

$$|t|^2 + |\kappa|^2 = 1 \tag{A.22}$$

APPENDIX A. DETERMINATION OF THE S-MATRIX PARAMETER RELATIONS THROUGH COUPLED MODE THEORY ANALYSIS

Appendix B

Further 1st Order Filter Considerations

B.1 Calculated 1st Order Ring Resonator Port Field Amplitudes

The port field amplitude solutions to the geometry in Figure 4 are analytically calculated, the results of which are provided below:

Table B.1: 1^{st} order add-drop ring resonator port field amplitudes

$a_2 = a_1\left(\frac{\kappa_1 t_2 \alpha_s e^{i\theta}}{1-t_1^* t_2 \alpha_s e^{i\theta}}\right)$	$b_1 = a_1\left(\frac{t_1 - t_2 \alpha_s e^{i\theta}}{1-t_1^* t_2 \alpha_s e^{i\theta}}\right)$	$b_2 = a_1\left(\frac{\kappa_1}{1-t_1^* t_2 \alpha_s e^{i\theta}}\right)$
$b_3 = a_1\left(\frac{\kappa_1\sqrt{\alpha_s e^{i\theta}}}{1-t_1^* t_2 \alpha_s e^{i\theta}}\right)$	$a_3 = a_1\left(\frac{\kappa_1 t_2\sqrt{\alpha_s e^{i\theta}}}{1-t_1^* t_2 \alpha_s e^{i\theta}}\right)$	$a_4 = a_1\left(\frac{\kappa_1\kappa_2\sqrt{\alpha_s e^{i\theta}}}{1-t_1^* t_2 \alpha_s e^{i\theta}}\right)$

B.2 Spectral Comparison of the 1st Order Ring Resonator Filter and the 1st Order MZI Filter

It was introduced in Chapter 2.2.3 that ring resonator and MZI filters are inherently different with respect to their spectral characteristics. Eq. 3.12 and Eq. 3.46/3.47 can be compared to identify this fundamental distinction of the two geometries. The feedback loop in the ring resonator filter results in such a response at the drop port that mainly rejects the signal transmission but allowing only for particular wavelengths (poles in the denominator expression of Eq. 3.12) to pass. On the contrary, with the feed-forward geometry of the MZI filter, the fundamental trend is to allow signal transmission for most part of the spectrum but hindering only selected wavelengths (zeros of the expression in Eq. 3.12) to propagate through the channels. This is depicted in Figure B.1 as example parameters of the systems are chosen and a comparison plot is generated between 1549 nm and 1551 nm. In

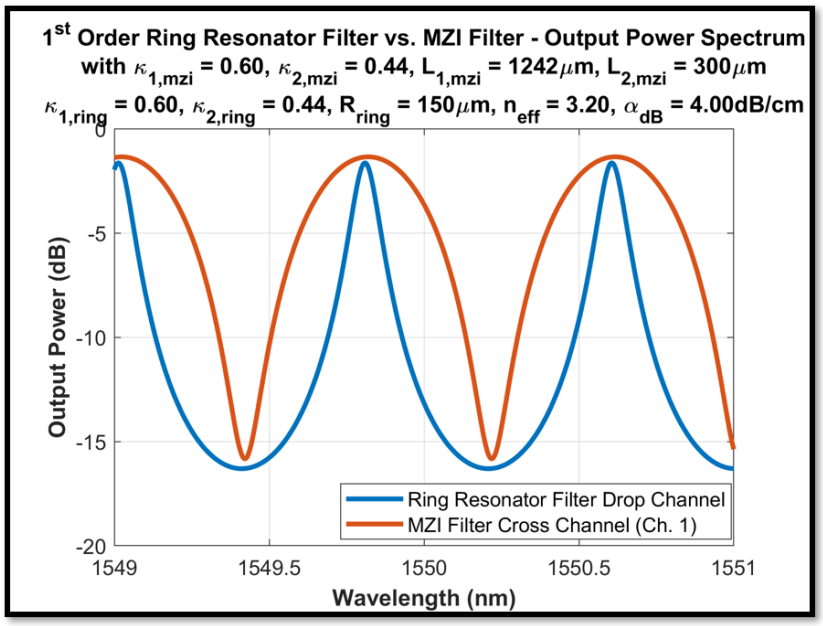

Figure B.1: 1^{st} order ring resonator and MZI filters - output spectra comparison

both geometries, the two coupling coefficients are determined to be the same, which actually doesn't correspond to the same physical conditions. Nevertheless, it should suffice for the goal of the practice here, as the idea is to have a mere comparison of the spectral behaviors of the two filters. Moreover, the ring circumference and the arm length differences, as well as the effective indices for both cases are chosen to be the same, in order to attain the same FSR and aligned resonance wavelengths on the spectrum.

As previously pointed out, the two spectra can be seen to have an inverse characteristic with respect to the other. This is because the drop channel of the ring resonator has Lorentzian type of resonance curves with sharp peaks, outside of which reduced signal powers are present in the spectrum and the cross channel of the MZI filter shows a direct sinusoidal output coming from Eq. 3.46/3.47, which mostly allows for comparatively high signal powers outside of a selected small spectral span. This was an interesting finding of the study on the two filters that affected the decisions made during the work and proved to be a useful exercise, which is why it is decided to be documented in this thesis.

Appendix C

S-Matrix Analysis of the 2^{nd} Order Filters

C.1 Serially Cascaded 2^{nd} Order Add-Drop Ring Resonator Filter

The serial cascaded 2^{nd} order double bus add-drop ring resonator filter model is sketched in Figure C.1, which is the generalized version of the geometry, where ring radii can be equal to each other or different. In the initial consideration, the focus is on the symmetrical structure with $R_1 = R_2 = R_{ring}$ and the definitions for the port and the coupling parameters are in agreement with Figure 3.1, except for having another ring between the first ring and the add-drop bus waveguide.

Having a coupled higher order arrangement significantly enhances the ER of the filter [54], with the slight cost of increased IL. Due to the coupled nature of the system, the poles split when the resonance frequencies of the two rings are the same, where the strength of the splitting can be controlled by the adjustment of the inter-ring coupling coefficient [10], [54]. This way, achieving higher ER values with still adjustable bandwidth and flat-topped bandpass shape [10] can be ensured with the 2^{nd} order geometry, which is an important advantage for the purposes of this work.

Here, the already introduced equations for the 1^{st} order filter will be repeated without going to the details of the derivations. The main addition is the inter-ring coupling and transmission coefficients, which are denoted with the subscript "int". The set of coupling equations for the first ring in S-matrix formalism read as:

$$\begin{pmatrix} b_1 \\ b_2 \end{pmatrix} = \begin{pmatrix} t_1 & -\kappa_1^* \\ \kappa_1 & t_1^* \end{pmatrix} \begin{pmatrix} a_1 \\ a_2 \end{pmatrix} \tag{C.1}$$

$$\begin{pmatrix} b_3 \\ a_2 \end{pmatrix} = \sqrt{\alpha_s e^{i\theta}} \begin{pmatrix} 1 & 0 \\ 0 & 1 \end{pmatrix} \begin{pmatrix} b_2 \\ a_3 \end{pmatrix} \tag{C.2}$$

$$\begin{pmatrix} a_3 \\ a_4 \end{pmatrix} = \begin{pmatrix} t_{int} & -\kappa_{int}^* \\ \kappa_{int} & t_{int}^* \end{pmatrix} \begin{pmatrix} b_3 \\ b_4 \end{pmatrix} \tag{C.3}$$

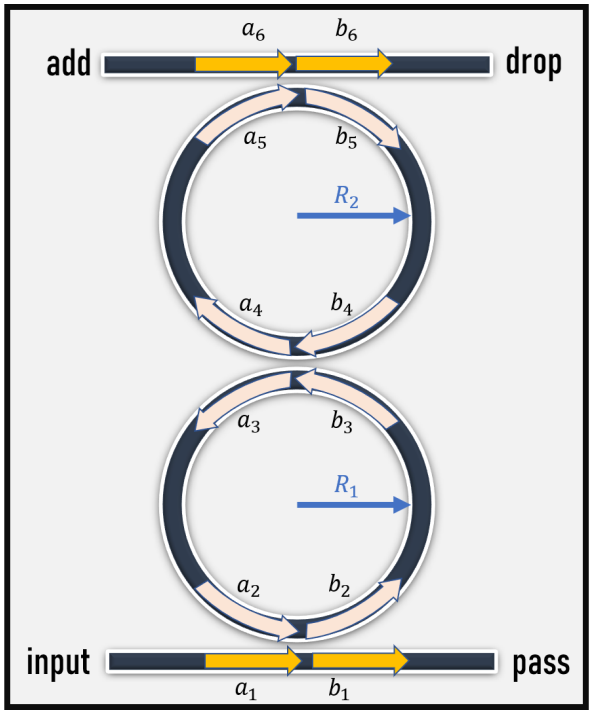

Figure C.1: 2^{nd} order double bus add-drop ring resonator filter model

Similar relations can be written for the case of the second ring:

$$\begin{pmatrix} a_5 \\ b_4 \end{pmatrix} = \sqrt{\alpha_s e^{i\theta}} \begin{pmatrix} 1 & 0 \\ 0 & 1 \end{pmatrix} \begin{pmatrix} a_4 \\ b_5 \end{pmatrix} \tag{C.4}$$

$$\begin{pmatrix} b_5 \\ b_6 \end{pmatrix} = \begin{pmatrix} t_2 & -\kappa_2^* \\ \kappa_2 & t_2^* \end{pmatrix} \begin{pmatrix} a_5 \\ a_6 \end{pmatrix} \tag{C.5}$$

with $a_6 = 0$ and:

$$\theta = \frac{4\pi^2 n_{eff} R_{ring}}{\lambda} = \frac{4\pi^2 n_{eff} R_{ring}}{c_0} \nu \tag{C.6}$$

Solving the set of equations with a procedure similar to the 1st order ring resonator yields the port field amplitudes in Table C.1. The power at the drop (output) port, $|b_6|^2$, is of importance for examining the filter response, which is plotted on top of a 1^{st} order filter output with the same κ_1 and κ_2 values and provided in Figure C.2a.

The most obvious difference between the two responses is the ER, which considerably improves with the 2^{nd} order filtering. Another increase can be seen in the IL, which is the drawback of having a larger and more complex geometry. Compared to the 1^{st} order filter, the 3-dB bandwidth of the 2^{nd} order filter is slightly narrower in this example with $\kappa_{int} = 0.42$. It can surely be increased by having larger values of the intermediate coupling coefficient, which however would enhance the resonance splitting and result in a non-flat-topped resonance behavior.

Table C.1: Port field amplitudes of the 2^{nd} order ring resonator filter

Port	Field Amplitude
b_1	$a_1\left(\frac{t_1-t_1t_2t_{int}^*\alpha_s e^{i\theta}-t_{int}\alpha_s e^{i\theta}+t_2\alpha_s^2 e^{2i\theta}}{1-t_2t_{int}^*\alpha_s e^{i\theta}-t_1^*t_{int}\alpha_s e^{i\theta}+t_1^*t_2\alpha_s^2 e^{2i\theta}}\right)$
b_2	$a_1\left(\frac{\kappa_1(1-t_2t_{int}^*\alpha_s e^{i\theta})}{1-t_2t_{int}^*\alpha_s e^{i\theta}-t_1^*t_{int}\alpha_s e^{i\theta}+t_1^*t_2\alpha_s^2 e^{2i\theta}}\right)$
b_3	$a_1\left(\frac{\kappa_1\sqrt{\alpha_s e^{i\theta}}(1-t_2t_{int}^*\alpha_s e^{i\theta})}{1-t_2t_{int}^*\alpha_s e^{i\theta}-t_1^*t_{int}\alpha_s e^{i\theta}+t_1^*t_2\alpha_s^2 e^{2i\theta}}\right)$
b_4	$a_1\left(\frac{\kappa_1\kappa_{int}t_2(\alpha_s e^{i\theta})^{\frac{3}{2}}}{1-t_2t_{int}^*\alpha_s e^{i\theta}-t_1^*t_{int}\alpha_s e^{i\theta}+t_1^*t_2\alpha_s^2 e^{2i\theta}}\right)$
b_5	$a_1\left(\frac{\kappa_1\kappa_{int}t_2\alpha_s e^{i\theta}}{1-t_2t_{int}^*\alpha_s e^{i\theta}-t_1^*t_{int}\alpha_s e^{i\theta}+t_1^*t_2\alpha_s^2 e^{2i\theta}}\right)$
b_6	$a_1\left(\frac{\kappa_1\kappa_{int}\kappa_2\alpha_s e^{i\theta}}{1-t_2t_{int}^*\alpha_s e^{i\theta}-t_1^*t_{int}\alpha_s e^{i\theta}+t_1^*t_2\alpha_s^2 e^{2i\theta}}\right)$
a_2	$a_1\left(\frac{\kappa_1\alpha_s e^{i\theta}(t_{int}-t_2\alpha_s e^{i\theta})}{1-t_2t_{int}^*\alpha_s e^{i\theta}-t_1^*t_{int}\alpha_s e^{i\theta}+t_1^*t_2\alpha_s^2 e^{2i\theta}}\right)$
a_3	$a_1\left(\frac{\kappa_1\sqrt{\alpha_s e^{i\theta}}(t_{int}-t_2\alpha_s e^{i\theta})}{1-t_2t_{int}^*\alpha_s e^{i\theta}-t_1^*t_{int}\alpha_s e^{i\theta}+t_1^*t_2\alpha_s^2 e^{2i\theta}}\right)$
a_4	$a_1\left(\frac{\kappa_1\kappa_{int}\sqrt{\alpha_s e^{i\theta}}}{1-t_2t_{int}^*\alpha_s e^{i\theta}-t_1^*t_{int}\alpha_s e^{i\theta}+t_1^*t_2\alpha_s^2 e^{2i\theta}}\right)$
a_5	$a_1\left(\frac{\kappa_1\kappa_{int}\alpha_s e^{i\theta}}{1-t_2t_{int}^*\alpha_s e^{i\theta}-t_1^*t_{int}\alpha_s e^{i\theta}+t_1^*t_2\alpha_s^2 e^{2i\theta}}\right)$

Returning to a more generalized case of the 2^{nd} order ring resonator filter with different ring radii, namely when $R_1 \neq R_2$, an interesting effect can be observed. By inspecting Eq. 3.22/3.23, it can be understood that the FSR of a ring resonator is inversely proportional to its circumference and having two rings with differing radii results in the modification of the general response of the filter by the so-called Vernier Effect [55]. The repetition of the resonance patterns in the spectrum extends due to this effect and the FSR attains a value that satisfies the following relation [55]:

$$FSR_{new} = m_1 FSR_1 = m_2 FSR_2 \tag{C.7}$$

where m_1 and m_2 are co-prime integers with the relation:

$$\frac{m_1}{m_2} = \frac{R_1}{R_2} \tag{C.8}$$

Similar to the previous exercises, the generalized equations for the theoretical model of the 2^{nd} order ring resonator filter for different radii are given below (again assuming $a_6 = 0$). Here, since it would not be realistic to define the same single-pass loss-coefficient for different ring circumferences, the power attenuation coefficient in Eq. 3.5 is used, which describes the loss per unit distance and modifies the equations slightly:

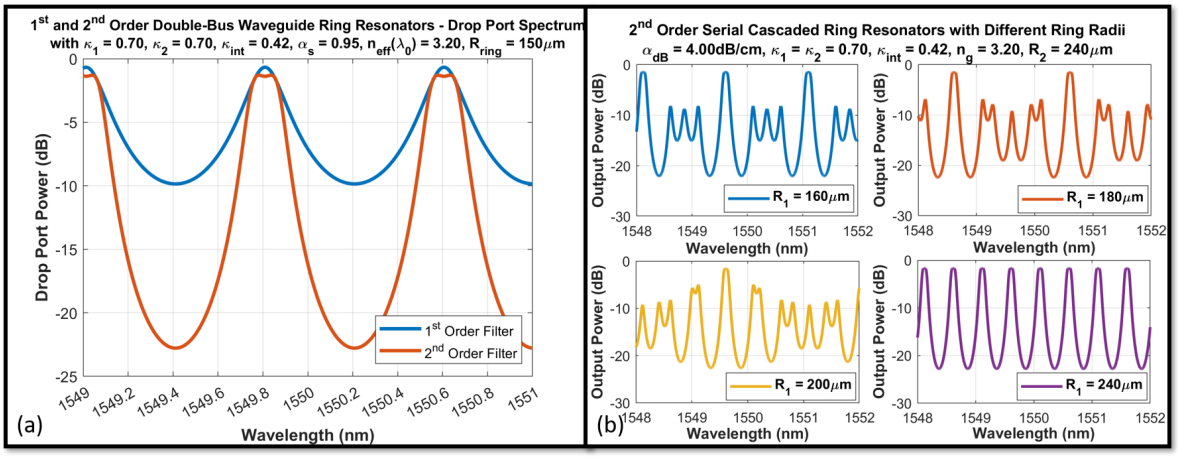

Figure C.2: (a) Drop port spectra of the 1^{st} and 2^{nd} order double-bus add-drop ring resonator filters and (b) the demonstration of the Vernier Effect with different radii ring resonators

$$\begin{pmatrix} b_1 \\ b_2 \end{pmatrix} = \begin{pmatrix} t_1 & -\kappa_1^* \\ \kappa_1 & t_1^* \end{pmatrix} \begin{pmatrix} a_1 \\ a_2 \end{pmatrix} \tag{C.9}$$

$$\begin{pmatrix} b_3 \\ a_2 \end{pmatrix} = e^{-\frac{(\alpha-2i\beta)L1}{4}} \begin{pmatrix} 1 & 0 \\ 0 & 1 \end{pmatrix} \begin{pmatrix} b_2 \\ a_3 \end{pmatrix} \tag{C.10}$$

$$\begin{pmatrix} a_3 \\ a_4 \end{pmatrix} = \begin{pmatrix} t_{int} & -\kappa_{int}^* \\ \kappa_{int} & t_{int}^* \end{pmatrix} \begin{pmatrix} b_3 \\ b_4 \end{pmatrix} \tag{C.11}$$

$$\begin{pmatrix} a_5 \\ b_4 \end{pmatrix} = e^{-\frac{(\alpha-2i\beta)L2}{4}} \begin{pmatrix} 1 & 0 \\ 0 & 1 \end{pmatrix} \begin{pmatrix} a_4 \\ b_5 \end{pmatrix} \tag{C.12}$$

$$\begin{pmatrix} b_5 \\ b_6 \end{pmatrix} = \begin{pmatrix} t_2 & -\kappa_2^* \\ \kappa_2 & t_2^* \end{pmatrix} \begin{pmatrix} a_5 \\ a_6 \end{pmatrix} \tag{C.13}$$

with

$$\beta L_i = \frac{2\pi n_{eff}}{\lambda} * 2\pi R_i = \frac{4\pi^2 n_{eff} R_i}{\lambda} = \frac{4\pi^2 n_{eff} R_i}{c_0}\nu, \qquad i \in \{1,2\} \tag{C.14}$$

The pass (b_1) and the drop (b_6) port field amplitude solutions to the above equations can be then found as:

$$b_1 = a_1 \left(\frac{t_1 - t_{int} e^{-\frac{(\alpha-2i\beta)L_1}{2}} - t_1 t_2 t_{int}^* e^{-\frac{(\alpha-2i\beta)L_2}{2}} + t_2 e^{-\frac{(\alpha-2i\beta)(L_1+L_2)}{2}}}{1 - t_1^* t_{int} e^{-\frac{(\alpha-2i\beta)L_1}{2}} - t_2 t_{int}^* e^{-\frac{(\alpha-2i\beta)L_2}{2}} + t_1^* t_2 e^{-\frac{(\alpha-2i\beta)(L_1+L_2)}{2}}} \right) \tag{C.15}$$

$$b_6 = a_1 \left(\frac{\kappa_1 \kappa_2 \kappa_{int} e^{-\frac{(\alpha-2i\beta)(L_1+L_2)}{4}}}{1 - t_1^* t_{int} e^{-\frac{(\alpha-2i\beta)L_1}{2}} - t_2 t_{int}^* e^{-\frac{(\alpha-2i\beta)L_2}{2}} + t_1^* t_2 e^{-\frac{(\alpha-2i\beta)(L_1+L_2)}{2}}} \right) \tag{C.16}$$

As a result of the obtained theoretical expressions, the radius of the second ring is fixed to 240 μm and different example values for the radius of the first ring (160 μm, 180 μm, 200 μm, 240 μm) are determined, which are then plotted for their corresponding drop port output powers in Figure C.2b. When the two radii are the same ($R_1 = R_2 = 240\,\mu m$), the spectrum appears to be quite periodic with the expected FSR between the resonances. For different common divisor ratios, the spectral repetition periods become different, some of which even stretch out of the simulated range of frequencies (1548-1552 nm). An important remark to be made here is that for small differences between the ring radii, higher FSR values (a direct consequence of Eq. C.7) are obtained, yet the suppression of the neighboring peaks is reduced at the same time. This can be easily observed by comparing the plots for $R_1 = 160\,\mu m$ and $R_1 = 180/200\,\mu m$, which needs to be considered when the objective is to increase FSR but at the same time have good cancellation of side resonances.

C.2 Serially Cascaded 2^{nd} Order Mach Zehnder Interferometer Filter

In this section, the derivations of the channel field amplitude formulas for the 2^{nd} order MZI filter are conducted, which relies on the findings of the 1^{st} order MZI filter analysis made in Chapter 3.2. The structure of the extended filter and the port definitions can be found in Figure C.3. Slightly different from the lattice filter configuration prevalently used in the literature [41], [56], the waveguide connection between the cross port of the first MZI and the upper port of the second MZI is removed in the considered model here (see Figure C.3). With the original model of the 2^{nd} order MZI filter, the ER and the pass band shape are affected by the exact optical phase accumulations through the interferometer arms in the system and the exact values of the coupling coefficients. This renders the filter response quite sensitive to changes in these parameters [41]. By detaching one of the channels between the two stages, the resulting effect becomes the simplification of the spectral response, where the overall transfer function is expressed as the multiplication of the individual filter stages. Here, the choice of connecting the bar or cross port of the first stage to the opposite port is arbitrary for 3-dB

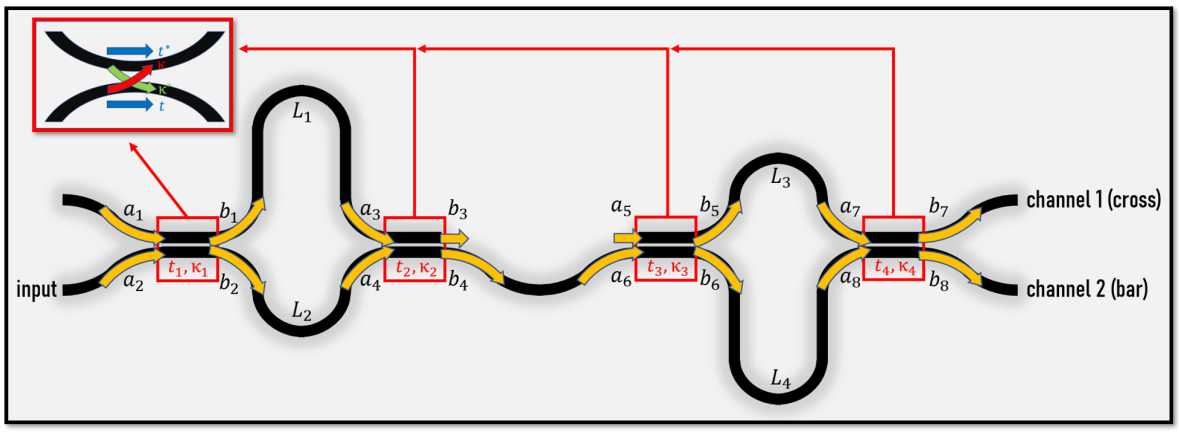

Figure C.3: 2^{nd} order MZI filter model

coupling, which is the interesting case with the highest ER. The only difference would be the phase shifted responses with respect to the other alternative, as well as the switching of the port outputs. The meaning of this is that the bar port power spectrum in of the configurations would be obtained in the cross port of the other geometry with a π phase shift and vice versa. Preferring here the bar-connected configuration seen in Figure C.3, the already calculated expressions for the output ports of the 1^{st} order model, b_3 and b_4 are repeated here for convenience:

$$b_3 = a_4\kappa_2 + a_3 t_2^* = a_2\left(t_1\kappa_2 e^{-\left(\frac{\alpha L_2}{2} - i\theta_2\right)} + \kappa_1 t_2^* e^{-\left(\frac{\alpha L_1}{2} - i\theta_1\right)}\right) \tag{C.17}$$

$$b_4 = a_4 t_2 - a_3\kappa_2^* = a_2\left(t_1 t_2 e^{-\left(\frac{\alpha L_2}{2} - i\theta_2\right)} - \kappa_1\kappa_2^* e^{-\left(\frac{\alpha L_1}{2} - i\theta_1\right)}\right) \tag{C.18}$$

The additional equations for the newly introduced final section are written as:

$$\begin{pmatrix} a_5 \\ a_6 \end{pmatrix} = \begin{pmatrix} 0 & 0 \\ 0 & 1 \end{pmatrix} \begin{pmatrix} b_3 \\ b_4 \end{pmatrix} \tag{C.19}$$

$$\begin{pmatrix} b_5 \\ b_6 \end{pmatrix} = \begin{pmatrix} 0 & \kappa_3 \\ 0 & t_3 \end{pmatrix} \begin{pmatrix} a_5 \\ a_6 \end{pmatrix} \tag{C.20}$$

$$\begin{pmatrix} a_7 \\ a_8 \end{pmatrix} = \begin{pmatrix} e^{-\frac{\alpha L_3}{2} - i\theta_3} & 0 \\ 0 & e^{-\frac{\alpha L_4}{2} - i\theta_4} \end{pmatrix} \begin{pmatrix} b_5 \\ b_6 \end{pmatrix} \tag{C.21}$$

$$\begin{pmatrix} b_7 \\ b_8 \end{pmatrix} = \begin{pmatrix} t_4^* & \kappa_4 \\ -\kappa_4^* & t_4 \end{pmatrix} \begin{pmatrix} a_7 \\ a_8 \end{pmatrix} \tag{C.22}$$

with $a_5 = 0$ and the phase accumulation terms for the interferometer arms defined as:

$$\theta_i = \beta L_i = \frac{2\pi n_{eff} L_i}{\lambda_0}, \qquad i \in \{1, 2, 3, 4\} \tag{C.23}$$

The field amplitudes of the cross (b_7) and bar (b_8) channels can then be found as:

$$\begin{aligned} b_7 = a_2\Big(&t_1 t_2 t_3\kappa_4 e^{-\left(\frac{\alpha(L_2+L_4)}{2} - i(\theta_2+\theta_4)\right)} + t_1 t_2\kappa_3 t_4^* e^{-\left(\frac{\alpha(L_2+L_3)}{2} - i(\theta_2+\theta_3)\right)} - \\ &\kappa_1\kappa_2^* t_3\kappa_4 e^{-\left(\frac{\alpha(L_1+L_4)}{2} - i(\theta_1+\theta_4)\right)} - \kappa_1\kappa_2^*\kappa_3 t_4^* e^{-\left(\frac{\alpha(L_1+L_3)}{2} - i(\theta_1+\theta_3)\right)}\Big) \end{aligned} \tag{C.24}$$

$$\begin{aligned} b_8 = a_2\Big(&t_1 t_2 t_3 t_4 e^{-\left(\frac{\alpha(L_2+L_4)}{2} - i(\theta_2+\theta_4)\right)} - t_1 t_2\kappa_3\kappa_4^* e^{-\left(\frac{\alpha(L_2+L_3)}{2} - i(\theta_2+\theta_3)\right)} - \\ &\kappa_1\kappa_2^* t_3 t_4 e^{-\left(\frac{\alpha(L_1+L_4)}{2} - i(\theta_1+\theta_4)\right)} + \kappa_1\kappa_2^*\kappa_3\kappa_4^* e^{-\left(\frac{\alpha(L_1+L_3)}{2} - i(\theta_1+\theta_3)\right)}\Big) \end{aligned} \tag{C.25}$$

Taking the absolute squares of the Eq. C.24 and Eq. C.25 allows to compare the output power spectra of the 2^{nd} order filter with the 1^{st} order bar channel spectrum. In the first example, the arm length differences of the two stages are set equally (see Figure C.4a) and in the second, the ratio

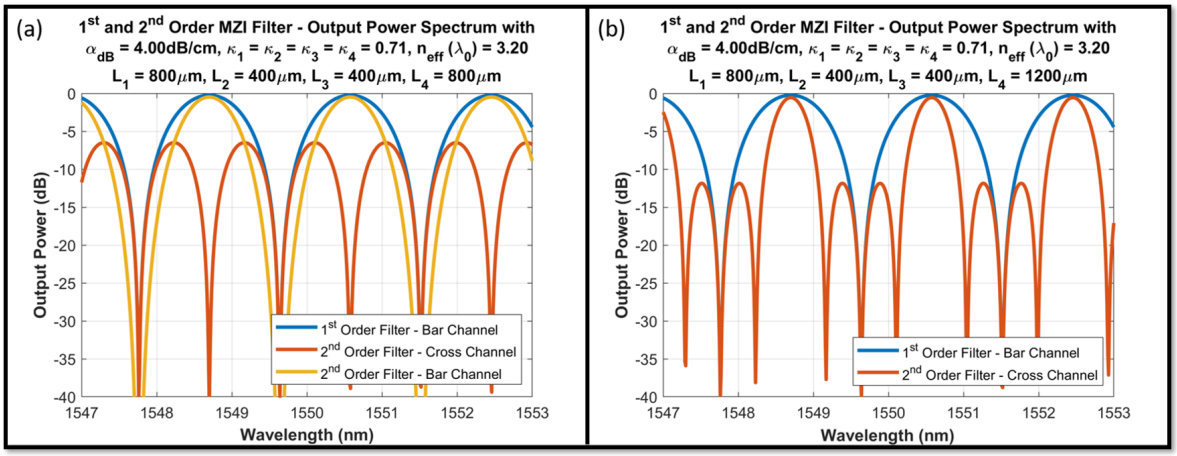

Figure C.4: Output power spectra comparison between the 1^{st} and the 2^{nd} order MZI filter spectra - (a) 1-to-1 and (b) 1-to-2 arm length difference ratio

between them are determined as 2, where the longer difference is used in the second MZI section (see Figure C.4b). Half-power transfer is considered for each coupling region ($\kappa_1 = \kappa_2 = \kappa_3 = \kappa_4 = \frac{1}{\sqrt{2}}$) and the losses, as well as effective indices, are set in accordance with the value preferred in the analysis of the 1^{st} order MZI filter from Figure 3.6. Figure C.4a shows the bandwidth reduction for both bar and cross channels of the 2^{nd} order filter in comparison with the 1^{st} order filter output. This is even more improved when the 2^{nd} stage arm difference is arranged to be the twice of the 1^{st} stage, as shown in Figure C.4b. Although the finesse of MZI filters cannot be as flexibly and straightforwardly arranged as in the case of ring resonator filters by the adjustment of coupling coefficients, the possibility still exists, one example of which is shown here.